https://lib.uliege.be

https://matheo.uliege.be

Travail de fin d'études et stage[BR]- [BR]-

Auteur : Lambrette, Ethan
Promoteur(s) : Mertens, Anne
Faculté : Faculté des Sciences appliquées
Diplôme : Master en ingénieur civil mécanicien, à finalité spécialisée en technologies durables en automobile
Année académique : 2025-2026
URI/URL : http://hdl.handle.net/2268.2/25189

Avertissement à l'attention des usagers :

Tous les documents placés en accès ouvert sur le site le site MatheO sont protégés par le droit d'auteur. Conformément aux principes énoncés par la "Budapest Open Access Initiative"(BOAI, 2002), l'utilisateur du site peut lire, télécharger, copier, transmettre, imprimer, chercher ou faire un lien vers le texte intégral de ces documents, les disséquer pour les indexer, s'en servir de données pour un logiciel, ou s'en servir à toute autre fin légale (ou prévue par la réglementation relative au droit d'auteur). Toute utilisation du document à des fins commerciales est strictement interdite.

Par ailleurs, l'utilisateur s'engage à respecter les droits moraux de l'auteur, principalement le droit à l'intégrité de l'oeuvre et le droit de paternité et ce dans toute utilisation que l'utilisateur entreprend. Ainsi, à titre d'exemple, lorsqu'il reproduira un document par extrait ou dans son intégralité, l'utilisateur citera de manière complète les sources telles que mentionnées ci-dessus. Toute utilisation non explicitement autorisée ci-avant (telle que par exemple, la modification du document ou son résumé) nécessite l'autorisation préalable et expresse des auteurs ou de leurs ayants droit.

UNIVERSITE DE LIEGE
FACULTE DES SCIENCES APPLIQUEES

Development and Characterization of Corrosion Resistant High Entropy Alloys through Laser Powder Bed Fusion

---

LAMBRETTE Ethan

Thesis presented to obtain the degree of:

Master of Science in Mechanical Engineering

Thesis supervisor:

MERTENS Anne

Ph.D. student supervisor:

SEIDOU Herrim

Academic year: **2025 – 2026**

Abstract

This study investigates the design and initial assessment of corrosion-resistant High Entropy Alloys (HEAs) processed by Laser Powder Bed Fusion (LPBF) using mixtures of commercially available metallic powders. Candidate compositions were first screened through CALculation of PHAse Diagrams (CALPHAD) based on thermodynamic calculations using Thermo-Calc and thermodynamic prediction tools such as Valence electron concentration (VEC), atomic size mismatch, or configurational mixing entropy. These candidate compositions were then tested using Differential Thermal Analysis (DTA) to predict equilibrium phases, to identify solidification events, and to evaluate microstructural trends as a function of composition. DTA-based microstructural characterization highlighted a progressive increase in phase complexity with aluminum additions, guiding the selection of two compositions, one Al-free and another with low aluminum content, for LPBF printing. Single track experiments were used to establish a viable processing window, followed by fabrication of cubic samples produced under a range of laser power from 100 to 200W, and a scan speed ranging from 200 to 1,000mm/s. Part quality was quantified using helium pycnometry and 3D optical profilometry, while Optical Microscopy (OM), Scanning Electron Microscopy (SEM), Electron BackScatter Diffraction (EBSD), and Energy-Dispersive X-ray spectroscopy (EDX) were carried out to analyze phase constitution, grain morphology, porosity, cracking, and chemical heterogeneities. The results demonstrate that densification and porosity are strongly dependent on processing parameters, whereas surface quality is additionally influenced by spatter and shielding gas flow-related depositions. Regardless of composition and parameter set, intergranular hot cracking was systematically observed, and oxide inclusions were detected at both micro- and nano-scale. Non-metallic inclusions were predominantly aluminum oxides in Al-containing samples, and silicon oxides in Al-free samples, in both cases the inclusions often exhibited chemically stratified interfacial layers. Overall, aluminum addition improved bulk quality within the tested process window but did not suppress cracking, emphasizing the need for composition specific LPBF optimization and improved control of powder chemistry and oxidation during processing.

Acknowledgements

I would like to express my sincere gratitude to my thesis promoter, Prof. Anne Mertens, for giving me the opportunity to carry out my master's thesis within her research group. I am thankful for her supervision, guidance throughout the research, and for the time she dedicated to reviewing my thesis.

I am also grateful to Dr. Jérôme Tchoufang Tchuindjang for his supervision and continuous guidance during the research process, as well as for the time he dedicated to reviewing my thesis.

My deepest thanks go to PhD. Student Abdul Herrim Seidou, whose support was essential to the successful completion of this work. As my internship supervisor, he guided me through every stage of the thesis, from literature research to experimental work and writing. Since this thesis is based on assisting his PhD research, his constant availability, patience, and expertise were invaluable, and I am sincerely thankful for his help in every aspect of this master's thesis.

I also express my sincere gratitude to the Metallic Materials Science (MMS) team for warmly welcoming me and for their support during my thesis work. Special thanks go to Sylvie Salieri, Olivier Dedry, Alessandra Segatto, and Gauthier Snoeck.

Finally, I would like to express my heartfelt gratitude to my family for their unconditional love, unwavering support, and constant encouragement throughout my studies. Their presence during both the highs and lows of this journey has been essential, and I am deeply thankful for everything they have done for me.

Table of Contents

Abstract ... i
Acknowledgements ... ii
List of Figures ... vi
List of Tables ... viii
Introduction ... ix
1. State of the Art ... 10
  1.1. Additive Manufacturing ... 10
    1.1.1. Advantages of Additive Manufacturing ... 11
    1.1.2. Limitations of Additive Manufacturing ... 12
    1.1.3. Additive Manufacturing Processes for Metals ... 13
    1.1.4. Laser Powder Bed Fusion (LPBF) ... 15
      1.1.4.1. Working Principle ... 17
      1.1.4.2. Rheological properties of powders ... 18
      1.1.4.3. Printing Parameters ... 20
      1.1.4.4. Typical Defects ... 24
  1.2. High Entropy Alloys (HEAs) ... 30
    1.2.1. Definitions and interpretations ... 32
    1.2.2. Four core effects of HEAs ... 35
    1.2.3. Phase formation in HEAs and corrosion behavior ... 39
2. Materials and Methods ... 40
  2.1. Base Powders ... 40
  2.2. Powder Preparation ... 42
    2.2.1. Preparation for Differential Thermal Analysis (DTA) ... 42
    2.2.2. Preparation for Laser Powder Bed Fusion (LPBF) ... 42
  2.3. Sample Production ... 44
    2.3.1. Differential Thermal Analysis (DTA) ... 44
    2.3.2. Laser Powder Bed Fusion (LPBF) ... 45
      2.3.2.1. Single Track ... 46
      2.3.2.2. Cubic Samples ... 47
  2.4. Pycnometer Analysis ... 49
  2.5. Profilometer Analysis ... 50
  2.6. Microstructure characterization ... 51
    2.6.1. Sample preparation ... 51

2.6.2. Optical Microscope (OM) and stream analysis software 52
2.6.3. Scanning Electron Microscope (SEM) 53
3. Results 54
3.1. Powders selection and mixture optimization 54
3.1.1. Mixture oriented powders selection and final compositions selection 54
3.1.2. Multiple powder hand mixing induced deviation 56
3.1.3. Thermo-Calc Predictions 57
3.2. Differential Thermal Analysis measurements 59
3.2.1. DTA curves 59
3.2.2. DTA samples microstructures 61
3.3. Process Maps 65
3.3.1. Single Tracks 65
3.3.2. Cubic Samples 67
3.3.2.1. $CrFe_{2.1}MnNi_2$ 67
3.3.2.2. $Al_{0.25}Cr_{1.25}Fe_{2.5}MnNi_{2.6}$ 68
3.4. As-built density measurements 69
$CrFe_{2.1}MnNi_2$ 70
$Al_{0.25}Cr_{1.25}Fe_{2.5}MnNi_{2.6}$ 70
3.4.1. $CrFe_{2.1}MnNi_2$ 70
3.4.2. $Al_{0.25}Cr_{1.25}Fe_{2.5}$MnNi2.6 71
3.5. As-built top layer profilometry 72
3.5.1. Surface morphology 72
3.5.2. Average and maximum heights 75
3.6. Microstructural characterization 76
3.6.1. Optical micrographs 76
3.6.1.1. Porosity analysis 76
3.6.2. Crystallographic structure (EBSD) 78
3.6.2.1. Phase distribution 78
3.6.2.2. Grain morphology 79
3.6.3. SEM micrographs 80
3.6.3.1. Cracks 80
3.6.3.2. Unmelted powders 81
3.6.3.3. Pores 82
3.6.4. EDX and elemental mappings 84
4. Discussions 90

4.1. Hot cracks formation 90
4.2. Oxidation and inclusions 94
4.3. Impact of processing parameters and composition on final part 96
4.4. Limitations of multiple powders mixtures 101
5. Conclusions 104
6. Perspectives 105
References 106
Appendices 113

List of Figures

Figure 1: Illustration of (a) subtractive manufacturing and (b) additive manufacturing [66] 11
Figure 2: Visualization of "complexity for free" and small lot size advantage of AM compared to conventional manufacturing methods [6] 12
Figure 3: Typical internal schematic of an LPBF machine [67] 16
Figure 4: Schematic of thermal phenomena occurring during LPBF [68] 17
Figure 5: Methods of powder production [24] 19
Figure 6: Illustration of the main LPBF parameters [69] 21
Figure 7: Illustration of different types of scan strategies [25] 23
Figure 8: (a) Lack-of-fusion, (b) keyhole, (c) gas pores micrographs [33] 25
Figure 9: Keyhole formation and pore formation due to collapse [70] 26
Figure 10: Illustration of balling effect caused by high laser power [71] 27
Figure 11: (a) Schematic diagram of the solidification of molten pool and (b) directional solidification of columnar crystals [34] 29
Figure 12: History chart of engineering materials marked with the birth of HEAs [62] 31
Figure 13: Ternary alloy systems illustrating the evolution of alloy design with the introduction of HEAs and CCAs [72] 32
Figure 14: Schematic representation of lattice distortion in BCC pure metals, conventional dilute alloys and HEAs, with different elements from A to E [73] 37
Figure 15: SEM micrographs of powders: (a) 316L, (b) Ni-Cr, (c) Al, and (d) Mn 41
Figure 16: Netzsch-Gerätebau GmbH - STA 449 C Jupiter Thermo-microbalance [45] 44
Figure 17: Aconity MINI LPBF printer [46] 45
Figure 18: (a) Overview of the upper section of the single-track array, and (b) close-up of a melt track (100W|200mm/s) of $CrFe_{2.11}MnNi_2$ alloy 47
Figure 19: Overview of the 20 Al0.25Cr1.25Fe2.5MnNi2.62 cubic samples 47
Figure 20: AccuPyc II Series 1345 gas Pycnometer [47] 50
Figure 21: Alicona InfiniteFocus G5 profilometer [48] 51
Figure 22: (left) STRUERS Citopress-1 and (right) STRUERS Tegramin-30 [50] 51
Figure 23: Sample prepared for SEM, in Bakelite and with silver paint 52
Figure 24: Tescan Clara Ultra-High-Resolution Scanning Electron Microscope [74] 53
Figure 25: DTA cooling curves at 5°C/min for $CrFe_{2.1}MnNi_2$, $Al_{0.25}Cr_{1.25}Fe_{2.5}MnNi_{2.6}$, $Al_{0.4}Cr_{1.1}Fe_{2.2}MnNi_{2.3}$, and $Al_{0.9}Cr_{1.4}Fe_{2.9}MnNi_3$ 59
Figure 26: SEM-micrograph of $CrFe_{2.1}MnNi_2$ DTA sample 61
Figure 27: SEM-micrographs of $Al_{0.25}Cr_{1.25}Fe_{2.5}MnNi_{2.6}$ DTA sample 61
Figure 28: SEM-micrograph of $Al_{0.4}Cr_{1.1}Fe_{2.2}MnNi_{2.3}$ DTA sample 62
Figure 29: SEM micrograph and EDX elemental mapping of $Al_{0.4}Cr_{1.1}Fe_{2.2}MnNi_{2.3}$ DTA sample 63
Figure 30: SEM-micrograph of $Al_{0.4}Cr_{1.1}Fe_{2.2}MnNi_{2.3}$ DTA sample 63
Figure 31: SEM micrograph and EDX elemental mapping of $Al_{0.9}Cr_{1.4}Fe_{2.9}MnNi_3$ DTA sample 64
Figure 32: Single track experiment process map of $CrFe_{2.1}MnNi_2$ with selected parameters for cubic sample printing and regions associated with typical defects 65
Figure 33: OM-micrographs of $CrFe_{2.1}MnNi_2$ single tracks with (a) surface damage, (b) irregular, (c) spatter, and (d) discontinuity defects. 66
Figure 34: 1cm^3 cubic sample printing process map of $CrFe_{2.1}MnNi_2$ with interrupted samples and regions associated with typical defects 67

Figure 35: Top view of the 20 cubic $CrFe_{2.1}MnNi_2$ samples printed on the substrate with the direction of the argon gas flow during printing displayed 68
Figure 36: $1cm^3$ cubic sample printing process map of $Al_{0.25}Cr_{1.25}Fe_{2.5}MnNi_{2.6}$ 68
Figure 37: Top view of the 20 cubic $Al_{0.25}Cr_{1.25}Fe_{2.5}MnNi_{2.6}$ samples printed on the substrate with the direction of the argon gas flow during printing displayed 69
Figure 38: Relative density heat map of $CrFe_{2.1}MnNi_2$ cubic samples wrt. Laser power (W) and Scan speed (mm/s) 70
Figure 39: Relative density heat map of $Al_{0.25}Cr_{1.25}Fe_{2.5}MnNi_{2.6}$ cubic samples wrt. Laser power (W) and Scan speed (mm/s) 71
Figure 40: Top layer surface roughness with inclined views and top view height maps 73
Figure 41: Top layer height distribution histograms 74
Figure 42: Top layer average height heat map of (a) $CrFe_{2.1}MnNi_2$ and (b) $Al_{0.25}Cr_{1.25}Fe_{2.5}MnNi_{2.6}$ cubic samples wrt. Laser power and scan speed 75
Figure 43: Top layer maximum height heat map of (a) $CrFe_{2.1}MnNi_2$ and (b) $Al_{0.25}Cr_{1.25}Fe_{2.5}MnNi_{2.6}$ cubic samples wrt. Laser power and scan speed 75
Figure 44: As-built porosity heat map of (a) $CrFe_{2.1}MnNi_2$ and (b) $Al_{0.25}Cr_{1.25}Fe_{2.5}MnNi_{2.6}$ cubic samples wrt. Laser power and scan speed 76
Figure 45: OM-micrographs of $CrFe_{2.1}MnNi_2$ cubic samples cross sections 77
Figure 46: EBSD phase map and corresponding pattern quality 78
Figure 47: EBSD phase map and corresponding pattern quality 78
Figure 48: EBSD grain boundary map and corresponding pattern quality 79
Figure 49: EBSD grain boundary map and corresponding pattern quality 79
Figure 50: SEM-micrograph of $Al_{0.25}Cr_{1.25}Fe_{2.5}MnNi_{2.6}$ cubic sample 80
Figure 51: SEM-micrograph of $CrFe_{2.1}MnNi_2$ cubic sample 81
Figure 52: SEM-micrograph of $Al_{0.25}Cr_{1.25}Fe_{2.5}MnNi_{2.6}$ cubic sample 81
Figure 53: SEM-micrograph of $CrFe_{2.1}MnNi_2$ cubic sample at the top layer 82
Figure 54: SEM-micrographs of $CrFe_{2.1}MnNi_2$ cubic samples 83
Figure 55: SEM-micrographs of (a) $Al_{0.25}Cr_{1.25}Fe_{2.5}MnNi_{2.6}$ cubic sample, and (b) $CrFe_{2.1}MnNi_2$ cubic sample 84
Figure 56: SEM-micrograph of $CrFe_{2.1}MnNi_2$ cubic sample with elemental mapping for Cr, Ni, Fe, Mn, and Si elements 85
Figure 57: Elemental mapping of $CrFe_{2.1}MnNi_2$ cubic sample for Si, and Mn elements 85
Figure 58: SEM-micrograph of $Al_{0.25}Cr_{1.25}Fe_{2.5}MnNi_{2.6}$ cubic sample with elemental mapping of Al, Cr, O, Fe, Mn, Ni, and Si elements 86
Figure 59: SEM-micrograph of $Al_{0.25}Cr_{1.25}Fe_{2.5}MnNi_{2.6}$ cubic sample ($P = 150W \mid V_s = 800mm/s$) with EDX point analysis for Al, Si, and O elements 87
Figure 60: SEM-micrograph of $Al_{0.25}Cr_{1.25}Fe_{2.5}MnNi_{2.6}$ cubic sample 88
Figure 61: SEM-micrograph of $CrFe_{2.1}MnNi_2$ cubic sample 89
Figure 62:Illustration of solidification cracking due to segregation of Si-rich liquid along grain boundary and the development of cracks driven by residual tensile stresses between adjacent grains [53] 91
Figure 63: Relation between particle packing density and particle size distribution [75] 102

List of Tables

Table 1: AM processes suited for Metals [4,9–11] 14
Table 2: Chemical Composition in wt.% of 316L & Ni-Cr powders 40
Table 3: Powder size ranges of selected powders 42
Table 4: DTA compositions tested 42
Table 5: Powder quantity used in 1kg powders mix for single track CrFe$_{2.11}$MnNi$_2$ 43
Table 6: Powder quantity used in 2.7kg powders mixtures for cubic samples printing of CrFe$_{2.11}$MnNi$_2$ and Al$_{0.25}$Cr$_{1.25}$Fe$_{2.5}$MnNi$_{2.62}$ 43
Table 7: Aconity MINI specifications [46] 46
Table 8: Printing Parameters for CrFe2.11MnNi2 Cubic Samples 48
Table 9: Printing Parameters for the Al$_{0.25}$Cr$_{1.25}$Fe$_{2.5}$MnNi$_{2.62}$ Cubic Samples 49
Table 10: Theoretical atomic percentages of Al, Cr, Fe, Mn, Ni, and Si elements in each tested composition using different powder-mixing strategies 55
Table 11: Theoretical atomic percentages of Al, Cr, Fe, Mn, Ni, and Si elements obtained for each tested composition after hand mixing of powders 56
Table 12: Differences in atomic composition between the actual compositions obtained after hand mixing and the corresponding target compositions 56
Table 13: Thermo-Calc equilibrium phase fractions predictions (vol. %) at 100,000 Pa and 1,000°C .. 57
Table 14: Principal cooling peaks for CrFe$_{2.1}$MnNi$_2$, Al$_{0.25}$Cr$_{1.25}$Fe$_{2.5}$MnNi$_{2.6}$, Al$_{0.4}$Cr$_{1.1}$Fe$_{2.2}$MnNi$_{2.3}$, and Al$_{0.9}$Cr$_{1.4}$Fe$_{2.9}$MnNi$_3$ DTA samples 60
Table 15: Mean density of powder’s mixture CrFe$_{2.1}$MnNi$_2$ and Al$_{0.25}$Cr$_{1.25}$Fe$_{2.5}$MnNi$_{2.6}$ 69
Table 16: Chemical composition of EDX point analysis (Figure 57) for CrFe$_{2.1}$MnNi$_2$ $_1$MnNi$_2$ cubic sample (P = 150W | V$_s$ = 800mm/s) 86
Table 17: Chemical composition (wt. %) of EDX point analysis (Figure 59) of Al$_{0.25}$Cr$_{1.25}$Fe$_{2.5}$MnNi$_{2.6}$ cubic sample (P = 150W | V$_s$ = 800mm/s) 87
Table 18: Chemical composition median in at. %, wt. %, and normalized wt.%, of Al, O, and Si elements of the nano scale inclusions in Al$_{0.25}$Cr$_{1.25}$Fe$_{2.5}$MnNi$_{2.6}$ cubic sample (P = 150W | V$_s$ = 800mm/s) 88

Introduction

Additive Manufacturing (AM) has attracted significant interest due to its ability to produce parts with complex geometries and high design flexibility. Among metal additive manufacturing technologies, Laser Powder Bed Fusion (LPBF) stands out for its capability to produce components with high dimensional accuracy and fine microstructural control through localized melting and rapid solidification of metallic powders.

High Entropy Alloys (HEAs) represent a relatively recent class of materials composed of multiple principal elements in comparable proportions. These alloys are known to exhibit attractive properties such as high corrosion resistance, good mechanical strength, and favorable thermal stability. Traditionally, HEAs are produced by arc melting or induction melting followed by casting, or by mechanical alloying combined with spark plasma sintering. However, increasing attention has been devoted to the processing of HEAs by LPBF due to the extremely high cooling rates involved, which can significantly influence phase formation and microstructure. As a result, preliminary alloy selection and phase stability assessment are crucial steps in HEA development for LPBF applications.

This thesis is part of a broader PhD. Project aiming to develop new HEAs with high corrosion resistance properties using LPBF technology. The present work focuses on the selection of suitable alloy compositions and experimental assessment of their behavior under LPBF processing.

Differential Thermal Analysis (DTA) was employed to investigate the solidification behavior of several candidate compositions under near-equilibrium conditions. A series of samples with varying aluminum contents were prepared and analyzed in order to identify phase formation tendencies and microstructural evolution as a function of composition. The resulting microstructures were characterized using optical microscopy (OM) and scanning electron microscopy (SEM), complemented by energy-dispersive X-ray spectroscopy (EDX).

In addition, LPBF experiments were conducted using both single-track and cubic sample strategies to evaluate printability and scan speed. The printed samples were characterized in terms of density, surface morphology, porosity, and microstructure using gas pycnometry, 3D optical profilometry, OM, SEM, and electron backscatter diffraction (EBSD). Particular attention was paid to defect formation mechanisms, including porosity, cracking, and the influence of multiple powder mixtures.

1. State of the Art

This chapter provides an overview of the fundamental concepts required to understand the results and discussion. It covers Additive Manufacturing (AM), with a focus on the Laser Powder Bed Fusion (LPBF) process used in this study, followed by an overview of High-Entropy Alloys (HEAs) as the materials investigated here.

1.1. Additive Manufacturing

Additive Manufacturing (AM), more commonly known as 3D printing, refers to a group of manufacturing processes that build objects layer by layer. Although it is often considered modern technology, it dates back to the 1960s when layer-based polymerization and laminated object manufacturing were first experimented [1]. AM gained popularity in the mid-1980s, with the commercialization of the first viable system in 1986 [2]. Initially used for polymer prototyping and visual models, AM expanded its application to metal and ceramic manufacturing with the emergence of powder bed-based technologies in the early 2000s. This allowed AM to become viable for both structural and functional manufacturing [3].

Compared to conventional manufacturing processes, which shape or remove material from an existing workpiece, Additive Manufacturing builds parts by adding material layer by layer. Conventional methods typically rely on machining, carving material into shape, or injection molding, which forms a part by compressing molten material inside a mold. These methods are generally referred to as subtractive manufacturing, as material is removed or reshaped from an existing piece, as illustrated in Figure 1(a) [4].

In contrast, AM begins with raw materials such as powders or wires, used with or without additives like binders or catalysts. The material is then consolidated through processes like polymerization, sintering, or melting and solidification, often involving heat or light to form a dense solid. The part is then built layer by layer, as in Figure 1(b), directly from a digital 3D model created using Computer-Aided Design (CAD) [4].

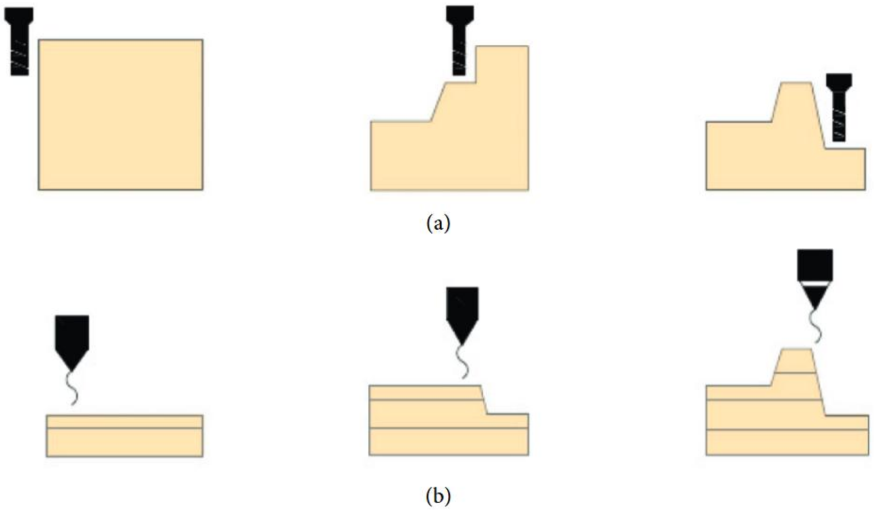

Figure 1: Illustration of (a) subtractive manufacturing and (b) additive manufacturing [66]

1.1.1. Advantages of Additive Manufacturing

This straightforward process, which directly converts a CAD model into a finished part, offers several key advantages for Additive Manufacturing, the most significant of which are:

- **Freedom of Geometry & Design**

Due to its layer-by-layer method, AM offers incredible freedom of geometry. This enables the fabrication of complex shapes that would be impossible using conventional, tool-based methods. It also allows the creation of intricate internal channels and the integration of multiple components into a single part. Lattice designs can also be employed to produce lightweight structures by reducing material usage and minimizing manufacturing constraints [4,5].

- **Reduced Waste**

Unlike conventional manufacturing methods that remove material from a solid block, additive manufacturing builds parts layer by layer. This significantly reduces waste, as most of the material becomes part of the final product. The main sources of waste in AM are the support structures required for overhanging or vertical features, as well as unused material, which can often be recycled, depending on the AM method used [4,5].

- **Short Production Cycle**

The direct link between CAD models and manufacturing processes enables rapid part development in AM. This facilitates prototyping and customization, as design modifications can be implemented quickly without disrupting the production chain. Multiple design iterations can be tested within a short time span, which is particularly valuable during prototyping [4,5].

- **Independence of cost and complexity:**

In AM, part cost is mainly determined by the volume of material and the build time, while geometric complexity has only a minor effect. This phenomenon, often referred to as "complexity for free", allows the design of intricate geometries without a significant impact on part cost (Figure 2). In addition, AM costs remain relatively constant with production volume because the main expenses come from the machine itself and the raw materials, rather than from tooling. This makes AM cost-efficient for small production batches, as illustrated in Figure 2. In contrast, conventional manufacturing methods are limited in both cost efficiency and achievable complexity [4–6].

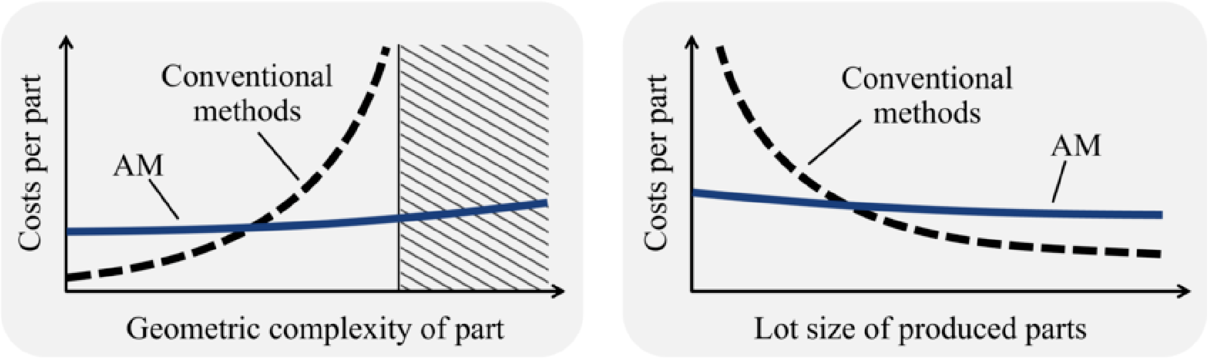

Figure 2: Visualization of "complexity for free" and small lot size advantage of AM compared to conventional manufacturing methods [6]

1.1.2. Limitations of Additive Manufacturing

Additive Manufacturing also presents several limitations that arise from the layer-by-layer nature and the specific process used. These depend on factors such as the energy source and the material bonding mechanism. The main drawbacks of AM are summarized below:

- **Microstructural Heterogeneity & Anisotropy:**

During the build process, parts are exposed to thermal stresses caused by repeated melting and rapid solidification. These conditions lead to microstructural heterogeneity and anisotropy, which can influence the final material properties [4,5].

Microstructural heterogeneity refers to variations in grain size, phase distribution, or chemical composition between microscopic regions of the material.

Anisotropy, on the other hand, describes the dependence of material properties on direction. It is inherent to the layer-by-layer process, since layers are stacked and bonded sequentially, creating potential weaknesses along the build direction [4,5].

- **Lack of Precision & Surface Quality:**

AM parts typically exhibit rough surfaces due to the layer-by-layer deposition process [4,5]. The formation of successive layers creates small steps on inclined surfaces, known as the stair-stepping effect, which leads to higher surface roughness compared to machined parts [7,8]. Other process-related factors, such as thermal gradients and variations in material deposition, can also cause dimensional inaccuracies, resulting in warping or distortion [9]. Post-processing is therefore required to achieve high-quality surfaces, increasing both manufacturing time and overall cost [4,5].

- **Building Platform Restrictions:**

The use of a building platform in AM imposes several limitations, the main one being the maximum achievable part size. The build volume is constrained by the size of the platform or the chamber, which inherently limits the dimensions of producible parts [9].
Scaling up is also challenging in AM, as larger platforms lead to higher thermal gradients and residual stresses, both of which can affect the final product quality [10].

- **Large Lot Size & Non-Complex Products:**

In AM, part cost remains relatively constant regardless of the production volume. This is advantageous for small batch manufacturing but becomes a disadvantage for large lot sizes, where conventional methods become more cost-efficient once the break-even point is reached (Figure 2) [4,5].
Similarly, AM part cost is only weakly affected by geometric complexity, making it ideal for highly complex parts but less competitive when producing simple geometries (Figure 2) [4,5].

1.1.3. Additive Manufacturing Processes for Metals

This study focuses on the development of a metallic alloy using the Laser Powder Bed Fusion (LPBF) process. Table 1 presents the different AM processes suited for metals.

Table 1: AM processes suited for Metals [4,9–11]

AM CATEGORY	METAL AM PROCESS	PROCESS DESCRIPTION
POWDER BED FUSION (PBF)	Direct Metal Laser Sintering (DMLS)	PBF builds parts by selectively melting or sintering layers of powders using a focused energy source such as a laser or an electron beam.
	Laser Powder Bed Fusion (LPBF)	
	Electron Beam Melting (EBM)	
	Direct Metal Laser Melting (DMLM)	
DIRECT ENERGY DEPOSITION (DED)	Laser Cladding	DED processes use a concentrated energy source (laser, electron beam, or electric arc) to melt and deposit material simultaneously. They are widely used for repairing existing components, adding features to substrates, or building large metal structures.
	Laser-Directed Energy Deposition (L-DED)	
	Laser Engineered Net Shaping (LENS)	
	Electron Beam Directed Energy Deposition (EB-DED)	
	Wire-DED	
	Thermal Energy	
BINDER JETTING (BJ)	Binder Jetting (BJ)	BJ selectively deposits a liquid binder onto powder layers to form a “green” part, which is then post-processed through curing, debinding, and sintering to produce the final component.

MATERIAL JETTING **(MJ)**	NanoParticle Jetting (NPJ)	NPJ deposits droplets containing metal nanoparticles, which are then consolidated through curing and sintering to form dense metallic parts.
SHEET LAMINATION **(SL)**	Laminated Object Manufacturing (LOM)	Thin metallic foils are cut to the desired shape, typically using a laser or precision blade, and then bonded layer by layer using adhesives (LOM) or ultrasonic welding (UAM)
	Ultrasonic Additive Manufacturing (UAM)	
MATERIAL EXTRUSION **(ME)**	Fused Deposition Modeling (FDM)	Material is extruded through a heated nozzle that selectively deposits the molten feedstock to create a 3D structure. Depending on the material, the process can be followed by washing and sintering to obtain the final part.
	Bound Powder Extrusion (BPE)	
COLD SPRAY **(CSAM)**	Cold Spray	Metal particles are projected at supersonic velocities and bond to the substrate through high velocity impact, without melting. This method is suitable for thick coatings, rapid repair, and heat-sensitive materials.

1.1.4. Laser Powder Bed Fusion (LPBF)

Laser Powder Bed Fusion (LPBF) is an additive manufacturing process in which a thin layer of metallic powder is spread across a build platform and selectively melted by a high-intensity laser. Melting and rapid solidification occur locally, allowing the part to be built layer by layer from a CAD model [4,5,11].

A typical LPBF system (Figure 3) includes a laser source, a movable build platform, a powder delivery and recoating mechanism (e.g., roller or scraper), and a process control unit. After each layer is solidified, the platform is lowered and a new powder layer is spread to maintain a uniform bed [4,5,12]. LPBF commonly uses fine metallic powders in the 30–45 µm range, which promote high packing density and enable the fabrication of parts with fine features [4,12].

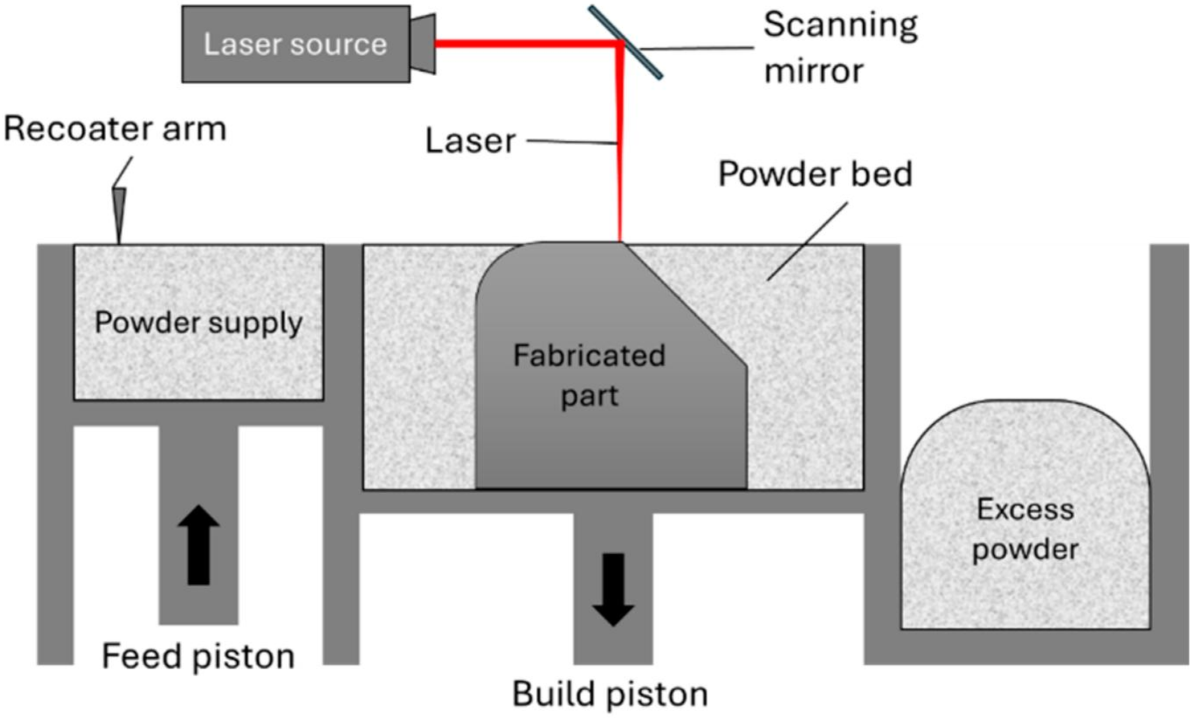

Figure 3: Typical internal schematic of an LPBF machine [67]

LPBF offers several advantages over conventional manufacturing methods. It allows the production of complex geometries without the constraints associated with machining or molding, reduces material waste, and increases flexibility in design. Compared with other metal AM techniques, LPBF generally provides finer resolution, better dimensional accuracy, and improved surface quality. Rapid solidification during the process also contributes to refined grain structures in the as-built material [4,13].

However, LPBF also presents notable limitations. High cooling rates and steep thermal gradients, typically on the order of 10^5–10^8 K/s, generate significant thermal stresses, segregation, and non-equilibrium phases, which complicate microstructure prediction [14]. The repeated thermal cycling inherent to the process can promote fatigue initiation, with subsurface or interlayer pores often acting as crack initiation sites [15].

Further defects may arise from powder contamination, trapped gas, or evaporation during melting, leading to porosity or local warpage [16,17]. Melt pool stability strongly influences surface roughness, defect formation, and the stair-stepping effect typical of layer-based manufacturing. Although these limitations cannot be fully eliminated, extensive research focuses on controlling these phenomena to improve part quality and reduce defect levels [18].

1.1.4.1. **Working Principle**

In LPBF, fabrication of parts is based on a repetition of four fundamental steps, powder deposition, laser exposure, melt pool formation, and solidification. These steps take place in a sealed and inert atmosphere, typically argon or nitrogen, to minimize oxidation phenomena during melting. The printing process begins by spreading a uniform powder layer across the substrate plate. The characteristics of this layer strongly depend on the rheological properties of the powders. Powder morphology and size distribution influence packing density and spreadability, which determine how efficiently the laser energy is absorbed and how consistently the melt pool develops across the previous layers[4,12].

Next, the laser scans the layer according to the associated CAD model. As pictured in Figure 4, the metallic powder absorbs the laser energy, producing a localized melt pool whose shape and size depends on parameters such as heat conduction, surface tension, and gravity [12,17]. During exposure, several thermophysical phenomena occur, including radiation absorption, phase transitions, fluid flow, and heat diffusion into the previous layers, the substrate, and the surrounding powder [12]. Since LPBF does not involve mechanical compaction, melt pools are highly sensitive to variations in laser input and powder characteristics, with capillary forces playing a major role in stabilizing the liquid region [4,12,17,18].

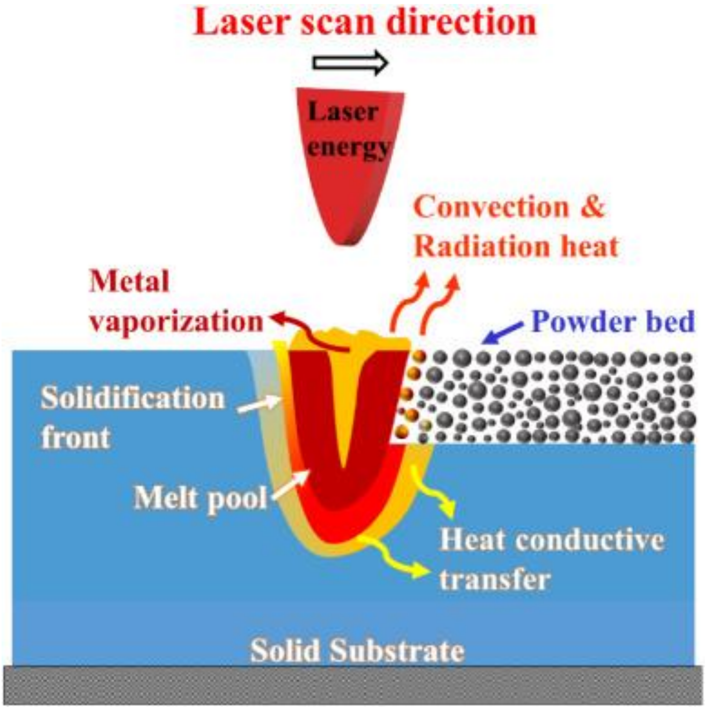

Figure 4: Schematic of thermal phenomena occurring during LPBF [68]

During melting, the thermal environment is characterized by high heating and cooling rates and steep temperature gradients. Inside the melt pool, temperatures can reach around 10^5°C, followed by cooling rates on the order of 10^5-10^8 K/s as heat dissipates through the previous layers, the substrate, and nearby powder (Figure 4) [17]. These high gradients promote rapid solidification and the formation of non-equilibrium microstructures [13]. LPBF typically operates in a full melting regime, unlike some other PBF processes that rely on partial melting or solid-state sintering, allowing re-melting of previously solidified material, which enhances interlayer bonding and overall densification [4,12,13,16].

After the complete scan of a layer, the build platform is lowered by one layer thickness to allow deposition of a new powder layer. During each cycle, the laser melts both the fresh powder and the upper region of the previously solidified layer, ensuring continuity between layers [12]. Heat redistribution into adjacent powder can also lead to partial sintering outside the intended melt track, which may alter powder behavior over time and influence recyclability and flow characteristics [4,5,12,15,16].

When the final layer is processed the part remains in the powder bed until thermal equilibrium is reached, which limits oxidation and reduces warpage during cooling. The part is then extracted, and the remaining powder is removed for reuse or recycling [4,5,12].

Thus, the key elements of LPBF rely on the four-step cycle, powder deposition, selective laser exposure, melt pool formation, and solidification, carried out under controlled thermal and atmospheric conditions. The local melt pool dynamics, rapid solidification, and interlayer re-melting enable the production of dense and complex metallic structures.

1.1.4.2. **Rheological properties of powders**

In Additive Manufacturing, powder properties play an important role in the finished product as they directly influence the surface finish, porosity, and both the mechanical and chemical properties. The two major properties are powder morphology and spreadability [19].

Morphology refers to the shape and size of powder particles, which can be defined as blocky, spherical, or irregular [20].
Spreadability describes the ability of a powder layer to evenly and consistently cover the build platform during deposition. A good spreadability is necessary to obtain high-quality components with low surface roughness and reduced porosity [21].

Both properties are closely related to the sphericity of the powders. In fact, spherical powders generally exhibit better flowability, improved spreadability, and thus gives a more uniform powder bed [20]. In contrast, powders with non-spherical morphologies tend to spread unevenly, producing a non-uniform powder bed with increased risks of spattering, and defect formation. This is due to the powder dispersion which is necessary to ensure consistent heat distribution during laser melting [20]. The quality of the powder also influences physical properties such as hardness and ductility, as well as chemical properties including reactivity, thus corrosion [22].

Powder quality and morphology are both strongly related to the production method used [23]. Powder production methods can be grouped into physical, mechanical, and chemical processes, as shown in Figure 5. Physical processes include atomization, melt spinning, and rotating electrode techniques. Mechanical methods comprise milling or grinding, and chemical processes involve reduction, electrolysis, or carbonyl synthesis. Each method comes with advantages and limitations, and the choice depends on the desired application, cost, and desired alloys [24].

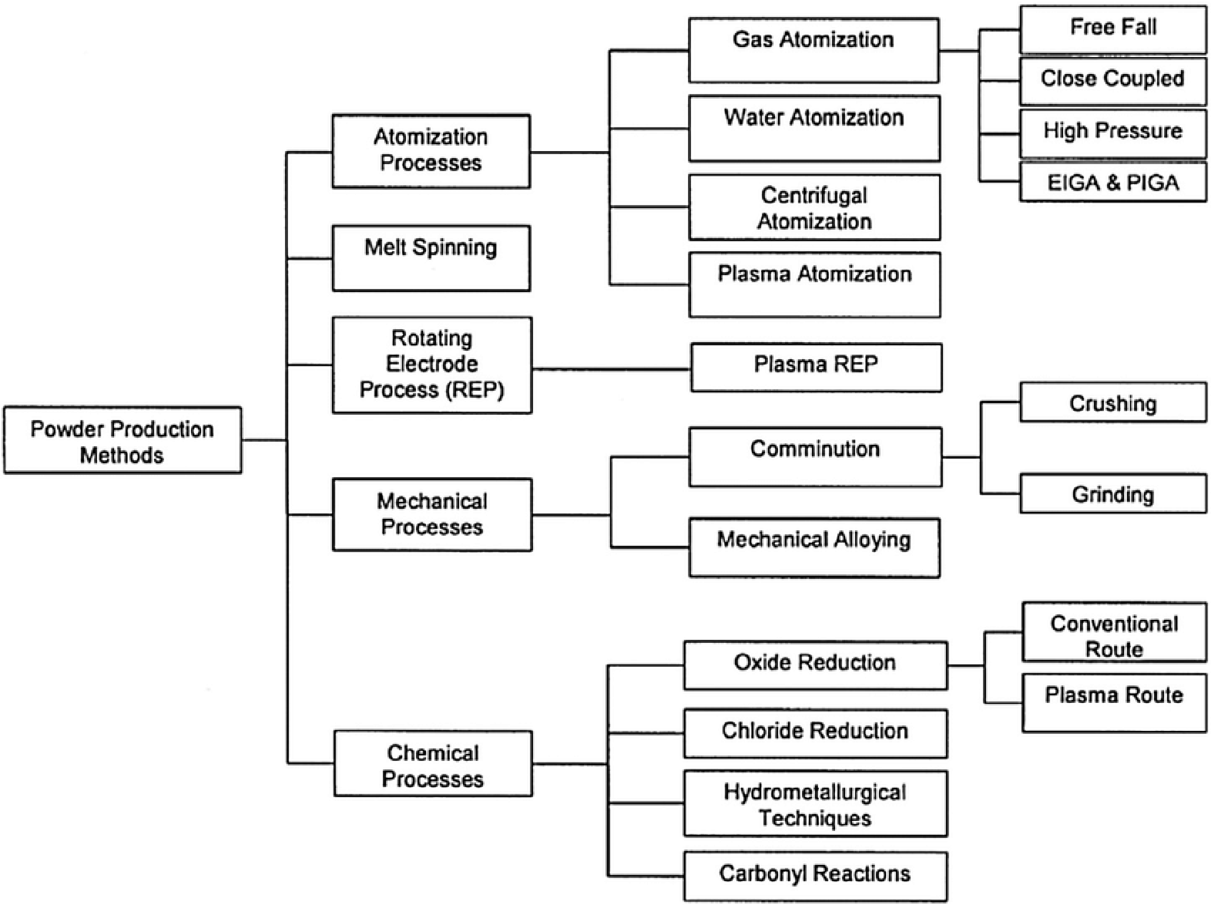

Figure 5: Methods of powder production [24]

Chemical processes rely on chemical reactions to precipitate or reduce metallic powders from precursor compounds. They often produce powders with very high purity, fine particle sizes, and controlled composition which can be necessary for certain industrial applications.
However, the resulting shapes can range from dendritic to sponge-like depending on the process. This makes chemical processed powders quite unsuitable for AM purposes due to their less favorable morphology and high production cost [22].

Mechanical methods use bulk materials they crush into fine particles using repeated deformation, fracture, and cold welding. The powders produced are generally highly irregular, angular powders with wide particle-size distribution and rough surfaces. This morphology leads to poor flowability and inconsistent powder-bed spreading, which makes them generally unsuitable for powder-bed fusion AM [20,21].

Physical processes, especially atomization methods, are the most popular powder production techniques in the AM industry. In fact, they can produce powders with spherical morphology, good flowability, and controlled particle size distribution [18,19,24].

Atomization works by breaking up a molten metal into droplets that solidify into powder particles. The specific method used (pressurized gas, plasma torch, water jets, rotating electrode speed) affects sphericity, oxygen content, and cooling rate, which can directly influence powder rheology and microstructure [18,19,24].

The powders used in this thesis were produced via gas atomization, the most widely used atomization method for AM alloys. This method uses a high-velocity inert gas jet to pulverize a molten alloy, forming droplets that solidify into nearly spherical particles. Gas-atomized typically yields powders with high sphericity, good flowability and spreadability, and narrow particle-size distribution. However, these powders usually exhibit satellites which can decrease flowability and increase interparticle friction which may influence spreadability [20,21,25].

1.1.4.3. **Printing Parameters**

The major printing parameters that influence LPBF process, shown in Figure 6, are laser power, scanning speed, layer thickness, and hatch distance. These can be put into relation to compute the volumetric energy density (E_d) and the linear energy density (E_l). Energy densities are used as a simplified comparison of process settings and are frequently used to correlate processing conditions with melt-pool stability, defect formation, and overall part quality [17,18,26].

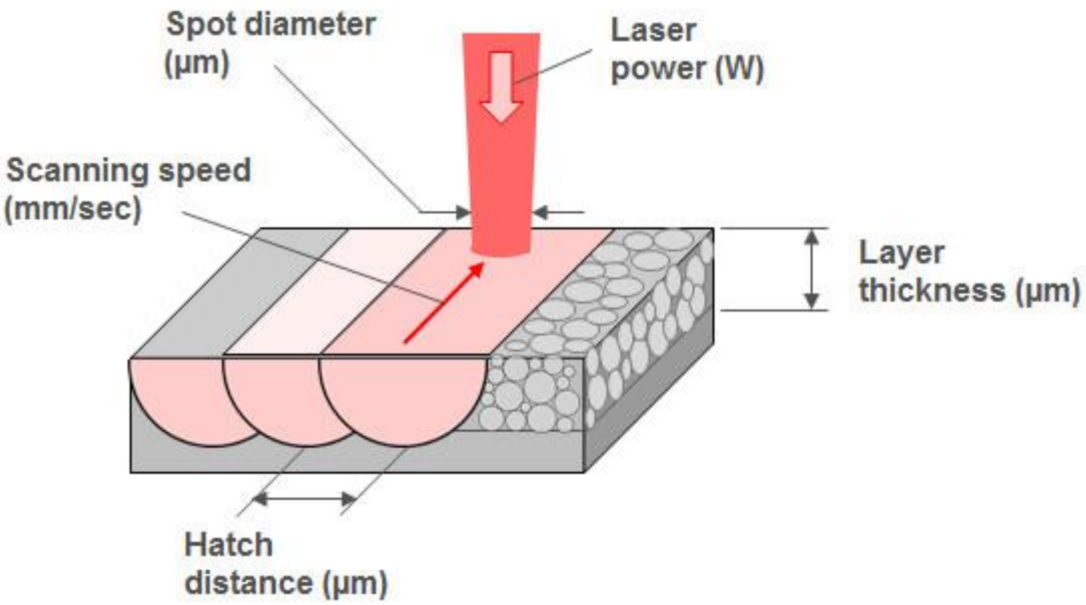

Figure 6: Illustration of the main LPBF parameters [69]

- **Laser power**

Laser power refers to the energy delivered by the laser beam per time unit. In LPBF, it is a major processing parameter because it determines the amount of heat transferred to the powder bed. Low laser power generally promotes shallow melt pools and partial melting, increasing the risk of lack-of-fusion defects. In contrast, high laser power improves melting efficiency but also raises the risks of keyholing, vaporization, spattering, and excessive residual stresses. Thus, laser power must be selected in combination with the other process parameters to ensure a stable melt pool and the formation of dense, defect-free parts [10,17,18].

- **Scanning speed**

Scanning speed refers to the velocity of the laser beam when moving across the powder bed. It directly affects the exposure time between the laser and the material, thus influences the melt-pool size, thermal gradients, and solidification behavior. High scanning speeds will reduce the time during which the laser interacts with the material, leading to smaller and shallower melt pools that may result in partial melting and lack-of-fusion defects if coupled with insufficient laser power. In contrast, low scanning speeds increase the energy input per unit length, which promotes deeper melt pools while also increasing the risk of excessive heat, thus keyholing, and excessive evaporation. Similarly to the laser power, scanning speed must be balanced with other printing parameters to achieve stable melting, consistent track morphology, and overall high-quality parts [10,14,18].

- **Hatch distance**

Hatch distance refers to the spacing between two adjacent scan tracks within the same layer. It influences the overlap between neighboring melt pools, which is key to achieve uniform densification. Large hatch distance will typically result in insufficient overlap of the melt pools, leaving unmolten regions between tracks and an increase in lack-of-fusion defects and anisotropic mechanical properties. Oppositely, small hatch distance may lead to excessive overlapping, causing repeated remelting of previously solidified material. This can lead to higher residual stresses, distortion, and increased production time. Hatch distance also needs to be tuned with other printing parameters such as laser power and scanning speed to ensure continuous track bonding and consistent microstructure throughout the build [13,18,27].

- **Layer thickness**

Layer thickness refers to the height of each powder layer deposited across the build platform. It governs the amount of material that must be fully melted in a single pass, thus affecting the melt pool penetration and thermal gradients. Thick layers require higher energy input to achieve sufficient melting; insufficient energy may lead to partially melted regions and lack-of-fusion defects. In contrast, thinner layers generally improve surface quality, dimensional accuracy, and need less energy to fully melt. However, for similar dimensions, thinner layers will lead to increased build time and may lead to excessive remelting of previously solidified layers. Layer thickness must be balanced with other printing parameters to achieve high-quality parts [10,13,28].

- **Energy density**

Linear energy density (E_l) and volumetric energy density (E_d) are metrics commonly used to describe the combined effect of the main LPBF parameters [13,18].

Linear Energy Density (E_l):

$$E_l = \frac{P}{v_s} \tag{1}$$

Volumetric energy density (E_d):

$$E_d = \frac{P}{v_s \cdot h \cdot t} \tag{2}$$

Where, P is the laser power [W], v_s the scanning speed [mm/s], h the hatch distance [mm], and t the layer thickness [mm].

Linear energy density represents the energy input per unit length of a scan track, where volumetric energy density represents the energy input per unit volume of processed material. E_l is typically used in single-track studies, while E_d is more commonly employed for identifying defect regimes, such as lack of fusion at low E_d, and keyholing at high E_d [10,17].

However, these metrics have some limitations. Energy densities do not account for powder-related factors such as particle morphology, absorptivity, or thermal conductivity, as well as several important process variables, such as scan strategy or build plate preheating. Thus, identical energy-density values can correspond to significantly different melt-pool conditions and defect regimes [13,24,26].

- **Scan strategy**

Scan strategy refers to the pattern followed by the laser during the scanning of each layer. It strongly influences melt pool stability, heat distribution, and residual stresses. Four major scan strategies are commonly used in LPBF, as shown in Figure 7 [9,13,29].

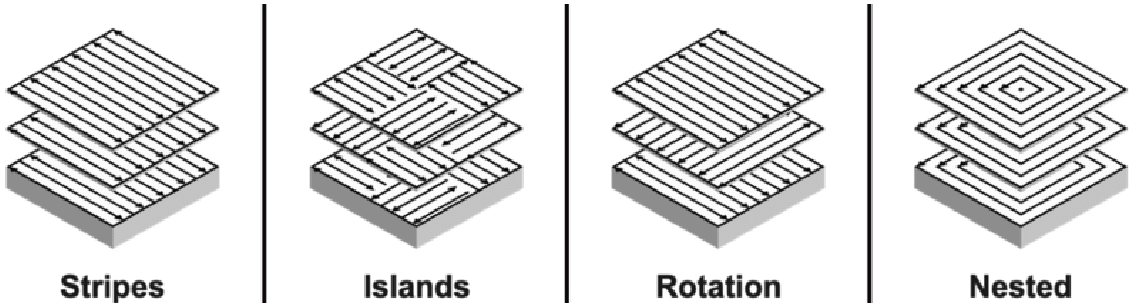

Figure 7: Illustration of different types of scan strategies [25]

Stripes consists in scanning long, continuous tracks and repeating these tracks across the build. This strategy is efficient but may generate directional heat accumulation, potentially increasing thermal gradients along the scan direction [9,29].

Islands divide the layer into small square or rectangular regions that are scanned independently. This reduces long-range thermal gradients and helps homogenize temperature distribution. However, this creates boundaries between islands which may become sites for incomplete fusion if the overlap is insufficient [9,13,29].

Rotation strategies alternate the scan direction between layers, typically rotating under a fixed angle at each iteration. Angles of 45°, 67°, and 90° are commonly used for rotating patterns. This method helps reduce anisotropy and avoid directional heat accumulation which tends to reduce residual stresses, warping and cracking [9,10,29].

Nested scan strategy consists of inward or outward patterns following the contours spaced by hatch distance. This technique typically improves dimensional accuracy at part edges but may lead to increased exposure time due to repeated remelting near the contours [13,29].

The selected pattern and rotation scheme have a direct impact on thermal history, microstructure development, defect formation, and overall part quality. It is then necessary to find a balance between the set of printing parameters and the scan strategy to obtain a good part [10,13,29].

- **Build plate preheating**

Build plate preheating consists of raising the temperature of the substrate prior to and during the printing process. Its main purpose is to reduce thermal gradients generated during rapid melting and solidification [10,26]. Low substrate temperature leads to steep gradients, increasing residual stresses, and risk of warping or cracking, which can be typically seen in HEAs [30,31].

Preheating the substrate helps mitigate these stresses by reducing the cooling rates and promoting a more uniform solidification [17,18]. Interlayer bonding is also improved, while the formation of cold spots or microcracks is inhibited [15,29]. However, excessive preheating temperatures may cause grain coarsening or unwanted phase formation [24,32].

In most conventional LPBF applications, the build plate is either unheated or only mildly preheated, since many alloys can be processed without elevated substrate temperatures [27]. In contrast, HEAs usually develop high thermal stresses during processing, making them prone to cracking [30,31]. Preheating then becomes a key parameter to reduce thermal gradients, stabilize melt pool behavior, and thus improve processability.

1.1.4.4. **Typical Defects**

Laser Powder Bed Fusion is prone to multiple types of defects originating from the rapid thermal cycling, localized melting, and powder-based nature of the process [10,26]. These can affect the mechanical, chemical, and physical properties of the final part, making it necessary to understand how they form to optimize both the process and the alloy development [7,9,10,13,26].

The most frequent defects are porosities which can form through multiple mechanisms, the most common being keyhole instability, lack-of-fusion (LoF), and entrapped gases [17,28,33]. Each mechanism generates pores with distinct morphologies, distributions, and causes [15].

Other defects commonly seen in LPBF include balling, which promotes track discontinuity [18]. Cracks are also frequent and often formed due to high thermal gradients during rapid solidification [27,34]. Oxide inclusions may also form; they are typically observed with contaminated powders or insufficient shielding [21,24].

Defects are directly related to processing parameters, powder characteristics, and alloy properties [20]. It is then possible to link each defect formation to process related causes [10,13].

• Porosity

Porosity is the most frequent defect in LPBF, typically formed from incomplete or unstable melting during laser exposure [10,13]. Pores reduce the density of the material and negatively affect mechanical properties as they act as crack initiation sites [7]. The three most common mechanisms that generate porosity are keyhole instability, lack-of-fusion due to insufficient melting, and entrapped gas due to the powder or the atmosphere inside the chamber [17,33]. Each mechanism generates pores with different morphologies, shown in Figure 8. It is then possible to relate each type of pore to processing conditions, thus allowing the optimization of the process that helps to mitigate these defects [28].

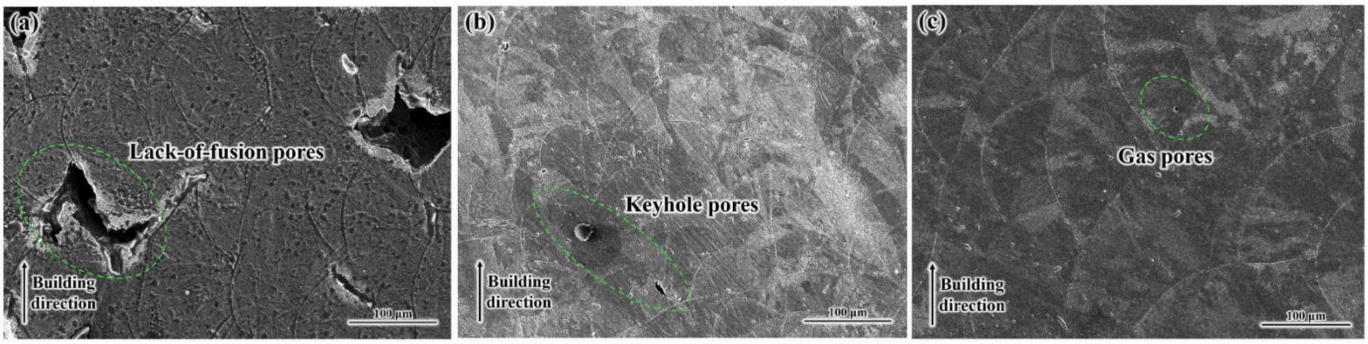

Figure 8: (a) Lack-of-fusion, (b) keyhole, (c) gas pores micrographs [33]

○ Lack-of-Fusion (LoF) pores

LoF pores form due to insufficient energy input to fully melt the powder layer or to remelt the underlying material. This leads to unmolten regions between adjacent laser tracks or between successive layers, creating irregular voids [10,13]. These pores are typically elongated with sharp-edges (Figure 8.a) and tend to be aligned with the melt pool boundaries.

This pore mechanism can be associated with low volumetric energy density caused by insufficient laser power, excessive scanning speed, large hatch distances, or poor overlap between tracks [28]. Reduced powder absorptivity can also promote LoF defects which can be induced by poor powder spreading, or powder characteristics [20]. Since LoF pores originate from insufficient melting, they can be minimized by adjusting the printing parameters to increase volumetric energy density [33].

○ Keyhole pores

Keyhole pores originate from excessive energy input, which causes deep and narrow vapor depressions to form at the center of the melt pool [17]. It can be associated with high volumetric energy density that is achieved either when the laser power is too high, or when the scanning speed is too low. The material reaches vaporization temperatures, and recoil pressure develops, driving the melt downward and creating a keyhole-shaped cavity. Figure 9 shows the evolution of the cavity which elongates due to laser reflections inside the sidewalls, increasing local energy absorption, and deepening the keyhole [26].

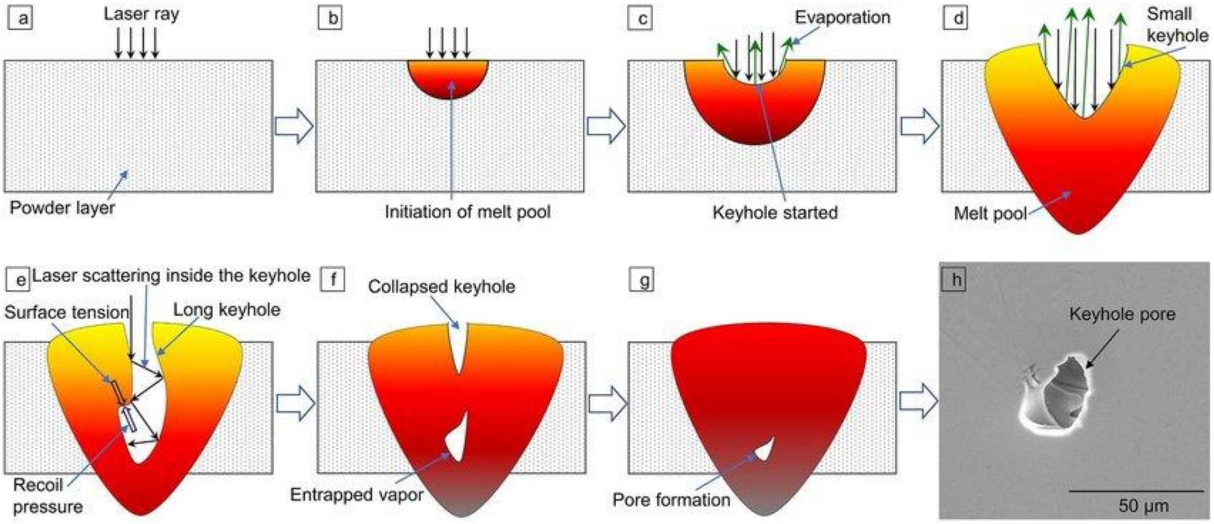

Figure 9: Keyhole formation and pore formation due to collapse [70]

Keyholes are inherently unstable, if the recoil pressure fluctuates or the laser exits the region before the liquid fills the cavity, the keyhole collapses and traps vapor, forming a . The pores formed are typically near-spherical shaped (Figure 8.b and Figure 9), and often surrounded by marks left by the collapse event [13].

Keyhole porosities are linked to high volumetric energy densities, promoted by excessive laser power, low scanning speeds, or combinations that concentrate heat locally. Thus, it is necessary to adjust the energy input to achieve melt pool stability and prevent keyhole formation [10].

○ Trapped Gas pores

Trapped gas pores form when gas becomes enclosed within the melt pool, which then solidifies before the bubbles can escape. These pores typically originate from entrapped gas inside the powder particles or from gas generated during melting, such as vaporized alloy or residual moisture [24]. During laser exposure, the gas can form bubbles within the melt pool. If the melt pool has a short lifetime, or a high viscosity, the gas bubbles cannot escape before the metal solidifies [10].

Gas pores are generally small, spherical, and homogeneously distributed throughout the material, as shown in Figure 8.c. These pores do not exhibit elongated or collapse-related morphologies which enables to easily differentiate them from keyhole and LoF pores [13].

The major cause of gas porosity is the powder quality. Internal porosity, adsorbed gases, or contamination in the powder can promote the formation of gas pores [20,21]. However, process parameters can also influence their formation if they combine low melt pool temperatures with excessive evaporation, thus leading to low bubble mobility and increased gas generation respectively [33].

Trapped gas pores cannot be eliminated, but it is possible to minimize this mechanism. In fact, high quality powders, monitored storage conditions, and optimized environmental and printing parameters help reduce this phenomenon [13].

- **Balling**

Balling refers to the formation of spherical droplets along the scan track. As shown in Figure 10, this defect occurs when the molten metal becomes unstable and retracts under the influence of surface tension. Instead of wetting the underlying layer, the liquid metal contracts into beads, increasing surface roughness and reducing bonding [13].

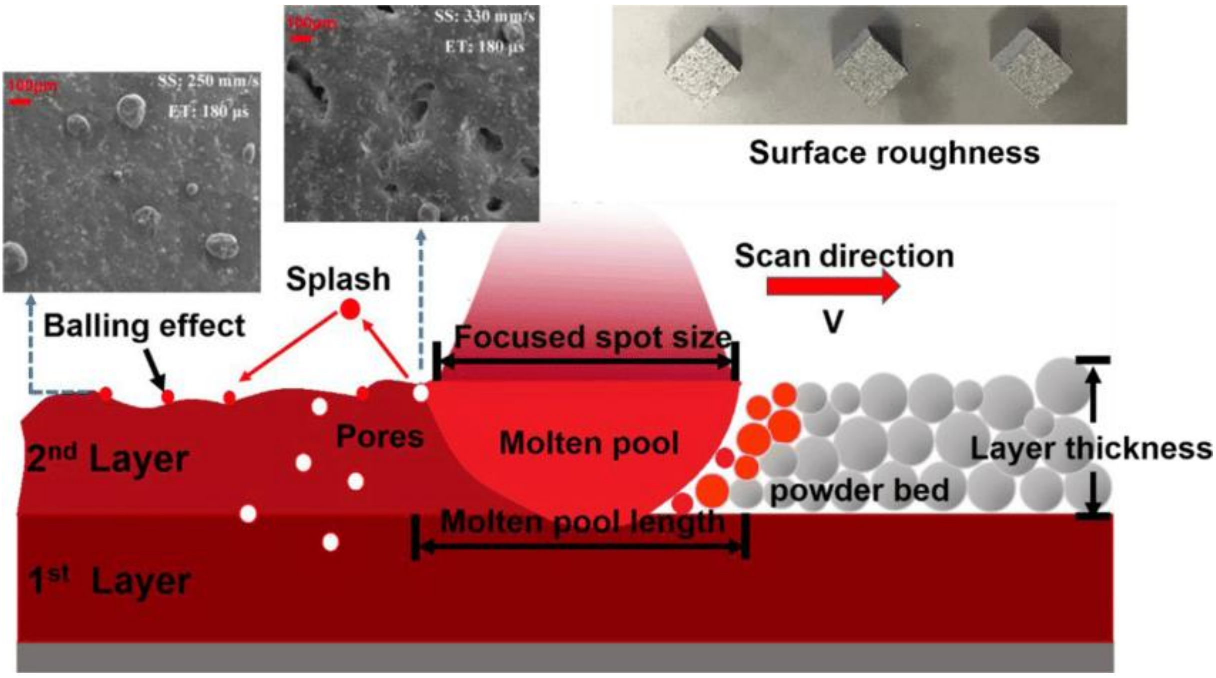

Figure 10: Illustration of balling effect caused by high laser power [71]

Balling tends to develop when the melt pool is too small to remain stable. This can be due to low volumetric energy density, caused by low laser power, high scanning speed, or thick layers, which results in poor wetting and insufficient melting. Ultra rapid solidification can also promote balling by preventing the melt pool from spreading [18,34]. Low melt pool fluidity due to powders with high oxide content, irregular morphology, or poor spreading may further promote balling [13,21].

Balling can also be coupled with splashing, projecting small particles from the melt pool, which can contribute to surface roughening and porosity. These defects can accumulate which may affect future tracks [26].

This mechanism can be mitigated by ensuring a stable and deeper melt pool. This can be done by adjusting the printing parameters, optimizing the layer thickness, and by using high quality powders [10].

- **Cracks**

Cracks are very common in LPBF and occur from the combination of rapid thermal cycling, steep thermal gradients, and the material's behavior to solidification [10,26]. Extreme heating and cooling conditions due to repeated melting of the powder and the underlying layers generate high residual stresses. If these stresses exceed the local strength or ductility of the material, a crack may form [9].

Different types of cracks exist depending on the temperature at which they occur. Solidification cracks form during the final stage of melt pool solidification, when the material is still partially liquid. As shown in Figure 11, they typically form along interdendritic regions where low-melting or segregated elements concentrate. The mushy zone can tear apart as it solidifies due to the presence of a wide solidification range, high solidification shrinkage, or insufficient feeding of the remaining liquid. In LPBF, this type of crack is generally intergranular and propagates along columnar grain boundaries aligned with build direction [27,34]. HEAs are particularly prone to this mechanism due to chemical segregation and the formation of transient phases in the mushy zone [30].

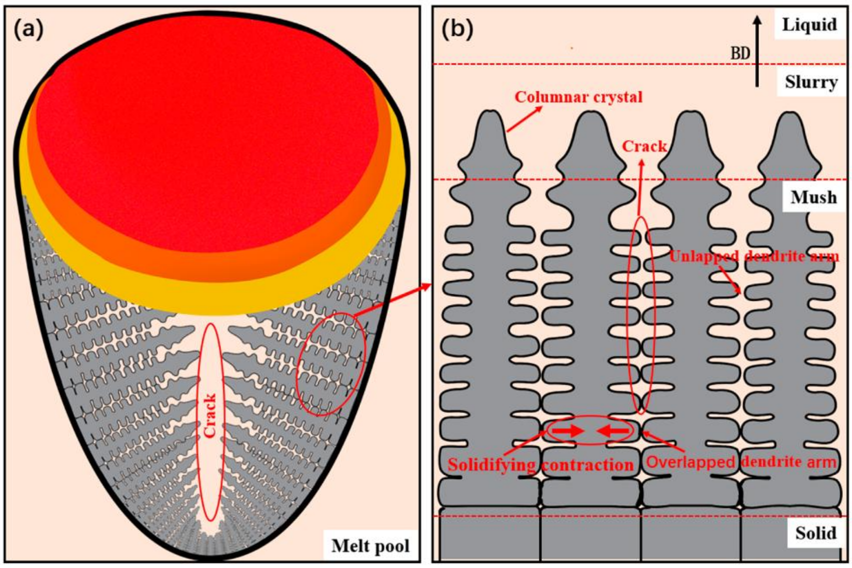

Figure 11: (a) Schematic diagram of the solidification of molten pool and (b) directional solidification of columnar crystals [34]

When the material is fully solidified but remains at high temperatures, solid-state cracks can form. These cracks are the results of different thermal contractions between the layers, or from high residual stresses induced by rapid cooling. The tensile stresses generated by the Upper layer contractions may affect the underlying material initiating cracks. Solid-state cracks often follow grain boundaries and are promoted by columnar microstructures, anisotropic thermal expansion, or high hardness phases [32].

Liquation cracks come from the heat-affected zone, next to the melt pool. During laser exposure, previously solidified material might be fully or partially remelted. If this liquid film does not wet the solid grain properly or resolidifies too rapidly, cracks can initiate along the boundaries it formed. Liquation cracks are promoted by low-melting elements segregation, oxides, or undesired elements at grain boundaries [13].

All these mechanisms are linked by the combination of material characteristics and LPBF process conditions. High scanning speed, insufficient preheating, unstable melt pools, or poor shielding may increase the thermal gradients and weaken interlayer bonding, promoting the formation of cracks. To mitigate their formation, it is important to reduce thermal stresses by preheating the substrate, optimizing printing parameters, and using appropriate compositions with narrow solidification ranges [10,34].

- **Oxide inclusion**

Oxide inclusions occur when oxygen reacts with the molten metal during LPBF, generating solid oxide particles trapped within the material. Typically, they originate from surface oxides on the powder particles or due to insufficient shielding during printing [13,24]. Even low oxygen levels can lead to inclusion formation due to the melt pool being small and repeatedly reheated. In HEAs, this effect can be further promoted by reactive elements such as aluminum or chromium [30].

Most oxides come from powders that are partially oxidized during production or storage. When the oxide layer on the particles is stable or too thick to dissolve, it can become part of the melt pool and incorporate between layers [20]. Process conditions such as inadequate inert gas flow, poor chamber sealing, or turbulence near the melt pool can increase local oxygen levels, promoting oxidation [21].

Oxide inclusions act as stress concentration sites and weaken interlayer bonding. To mitigate this defect, it is necessary to use powders with controlled oxygen concentrations, store them properly to prevent oxidation, and ensure good shielding conditions during the printing process [13].

1.2. High Entropy Alloys (HEAs)

Conventional alloys played a core role in the development of materials throughout history (Figure 12). They are typically based on one principal element, mixed with additional elements, in smaller quantities, to enhance or modify specific properties. This design strategy enabled major technological advances, from early copper-tin bronzes to modern steels and superalloys [35,36]. However, modern advanced engineering applications require materials with improved mechanical, chemical and thermal performances that conventional alloys cannot comply with which motivated the development of new alloy design approaches.

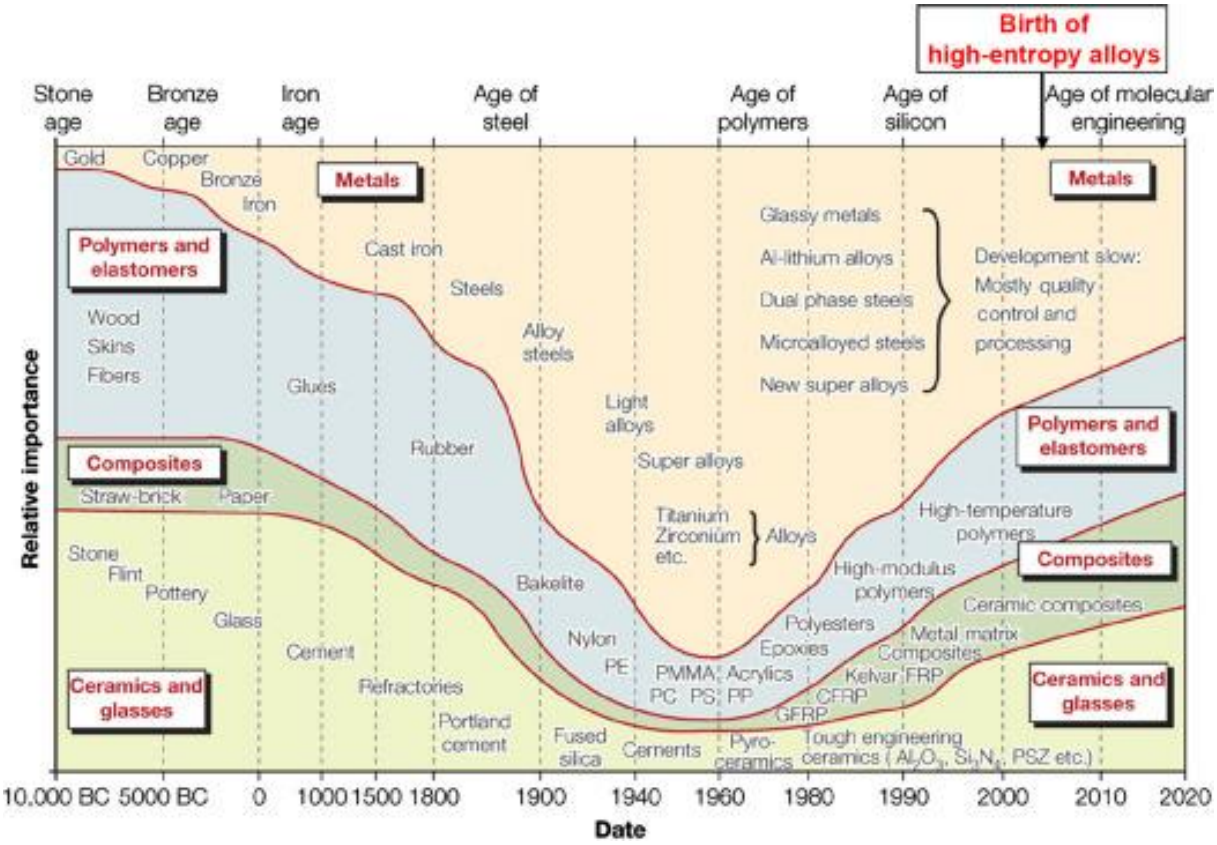

Figure 12: History chart of engineering materials marked with the birth of HEAs [62]

High Entropy Alloys (HEAs) represent a significant change in alloy design strategy. Instead of relying on a single dominant element, HEAs are composed of several principal elements in near-equiatomic proportions. They were discovered independently by Cantor et al., and Yeh et al. in 2004. Cantor developed an equimolar CoCrFeMnNi alloy that showed single-phase face-centered cubic (FCC) solid solution, despite its multicomponent composition [37,38]. Simultaneously, Yeh introduced the term “high entropy alloy” and proposed that high configurational mixing entropy can stabilize solid solution phases in alloys with equiatomic or near-equiatomic compositions [39]. These concepts define the new class of alloys that are HEAs with their unique structural and functional behaviors.

Due to their promising mechanical and functional properties, HEAs have attracted high interest. Multiple HEAs exhibit high strength combined with good ductility, improved fatigue resistance, and enhanced corrosion or oxidation behavior [40,41]. These properties come from their wide compositional design space, tunable microstructures, and specific deformation mechanisms.

Additionally, HEAs can be produced via conventional metallurgical manufacturing processes. Typically, the methods used are vacuum arc melting, induction melting, casting, and additive manufacturing. Powder-based techniques, such as mechanical alloying followed by spark plasma sintering are also employed [42]. Recently, AM became an important fabrication method for HEAs due to the extremely high heating and cooling rates involved, which reduce atomic diffusion and suppress the formation of intermetallic compounds [43].

1.2.1. **Definitions and interpretations**

Since their introduction in 2004, multiple definitions of High Entropy Alloys have been proposed. The term is now used in a broader sense than in the original papers by Yeh, and Cantor [38,39]. The main idea is that HEAs do not rely on a single principal element; instead, they are made with several elements in comparable proportions. Various criteria were suggested to classify HEAs, such as a minimum number of principal elements, atomic fraction ranges, or configurational mixing entropy limits [40,41].

These criteria lead to overlapping alloy families. Thus, terms such as High Entropy Alloys (HEAs), Compositionally Complex Alloys (CCAs), and MultiPrincipal Element Alloys (MPEAs) are used interchangeably, although they typically emphasize different aspects of the design. These concepts keep the base idea of having no single element dominant composition while broadening the compositional space. The compositional space shown in Figure 13, reflects this evolution with conventional alloys only using one to two dominant elements and multicomponent regions of HEAs and CCAs [40].

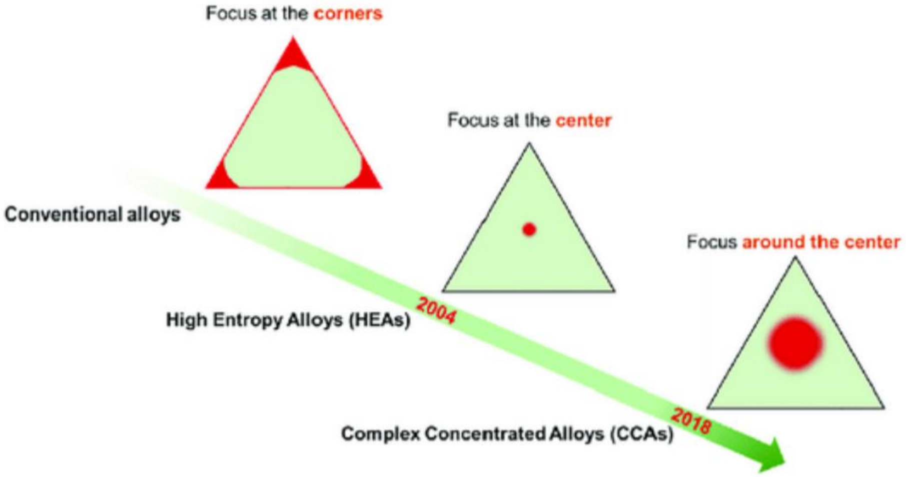

Figure 13: Ternary alloy systems illustrating the evolution of alloy design with the introduction of HEAs and CCAs [72]

Equiatomic HEAs are often considered a subset of the wider MPEA/CCA space. They correspond to compositions where the configurational entropy becomes sufficiently high to stabilize simple solid solutions over intermetallic compounds [39,41,44].

Several quantitative criteria were proposed to classify High Entropy Alloys and predict their tendency to form simple solid solutions rather than intermetallic compounds. These criteria are not universally accepted, but they provide useful guidelines for interpreting compositional effects in multicomponent alloys. The most frequently used parameters are the configurational mixing entropy, atomic size difference, thermodynamic stability indicators, and electronic structure descriptors [40,41].

- **Configurational mixing entropy ($\Delta \boldsymbol{S_{mix}}$)**

Configurational mixing entropy describes the degree of disorder associated with distributing different atomic species on the lattice sites of a solid solution. For multicomponent alloys such as HEAs, it quantifies how many distinct atomic configurations are possible, thus how entropy contributes to the thermodynamic stability of the material. It can be quantified using equation (3).

$$\Delta S_{mix} = -R \sum_{i} c_i \ln(c_i) \tag{3}$$

Where R is the gas constant, and c_i is the atomic fraction of element i.
For an equiatomic n-component alloy, this can be simplified to equation (4).

$$\Delta S_{mix} = R \ln(n) \tag{4}$$

Which shows that HEAs can achieve much higher mixing entropies than conventional alloys [40,41].

For HEAs, it was assumed that a sufficiently large configurational entropy could stabilize simple solid-solution phases by lowering the Gibbs free energy relative to ordered intermetallic compounds. This was introduced by Yeh et al., who proposed that high entropy favors random substitutional structures in multicomponent systems [39], which was supported by the observation of a single FCC phase in Cantor's work [38].

It was later proven that entropy alone does not guarantee solid-solution formation, since enthalpy and atomic size effects can counteract it. However, ΔS_{mix} remains as a descriptor for understanding HEA behavior [40,41].

- **Atomic size difference ($\boldsymbol{\delta}$)**

Atomic size difference serves to quantify the difference in atomic radii between the constituent elements in an alloy. It allows to estimate the degree of lattice distortion expected within a solid solution. In HEAs, it gives understand for both thermodynamic stability and mechanical behavior. It can be quantified using equation (5).

$$\delta = 100\sqrt{\sum_i c_i\left(1-\frac{r_i}{\bar{r}}\right)^2} \tag{5}$$

Where c_i is the atomic fraction of element i, r_i its atomic radius, and $\bar{r} = \sum_i c_i r_i$ the average atomic radius of the alloy elements.

The higher the atomic size difference, the greater the mismatch between atomic sizes, producing stronger lattice distortion. This distortion affects the Gibbs free energy of the solid solution, thus influencing the nature of the phases within the alloy, which can remain as a single-phase or tends to form intermetallics [40,41]. Some studies suggested that solid solutions were most likely to form when $\delta \leq 6\%$, whereas higher mismatches promoted phase separation or ordering [40,41].

Similarly to configurational mixing entropy, atomic size difference is not a defining criterion of HEAs, but a commonly used descriptor. It enables to identify compositions that are more likely to form stable solid solutions and guides the selection of element combinations with compatible atomic radii [40,41].

- **Balance between mixing enthalpy and configurational entropy (Ω)**

The thermodynamic behavior of HEAs is strongly influenced by the balance between mixing enthalpy and entropy. The mixing enthalpy ΔH_{mix} represents the chemical interactions between different atomic species and is defined in equation (6).

$$\Delta H_{mix} = \sum_{i\neq j} c_i c_j \Delta H_{ij} \tag{6}$$

Where c_i is the atomic fraction of element i, and ΔH_{ij} is the mixing enthalpy between elements i and j.

Negative values indicate attractive interactions that may favor ordered intermetallics, while small negative or slightly positive values support disordered solid solutions [40,41].

In HEAs, the stability of a solid solution depends on the competition between this mixing enthalpy and the configurational entropy $T\Delta S_{mix}$ from the Gibbs free energy (equation (7)).

$$G = \Delta H_{mix} - T\Delta S_{mix} \tag{7}$$

The original motivation behind the concept of high entropy alloys was that high configurational entropy would lower the free energy at elevated temperatures which would counter moderate enthalpic tendencies to order [38,39]. However, for strongly negative ΔH_{mix}, entropy contribution is overridden, leading to ordered phases even in equiatomic, high entropy compositions [40].

To correlate the two parameters, some studies suggested the Ω parameter as an empirical guideline for predicting solid-solution formation (equation (8)).

$$\Omega = \frac{T_m \Delta S_{mix}}{|\Delta H_{mix}|} \tag{8}$$

Where T_m is the composition average melting temperature, ΔS_{mix} the mixing entropy and ΔH_{mix} the mixing enthalpy.

It is assumed that, for $\Omega > 1.1$ simple solid solutions are favored. Although this limit is not universal, Ω is widely used for HEAs design as it combines both enthalpy and entropy indicators in a single parameter [40,41].

- ### Valence Electron Concentration (VEC)

Valence Electron Concentration is an electronic structure descriptor widely used to predict the stable crystal structure of high entropy alloys. It represents the average number of valence electrons contributed by each atom in the alloy using equation (9).

$$VEC = \sum_i c_i \, VEC_i \tag{9}$$

Where, c_i is the atomic fraction and VEC_i is the valence electron count of element i.

VEC is relevant for alloys where the stability of FCC and BCC structures correlate strongly with electronic filling. Empirical observations showed that FCC solid solutions tend to form when $VEC \geq 8$, BCC solid solutions are favored when $VEC \leq 6.87$, and FCC+BCC dual phases are typically seen in the intermediate range ($8 \geq \ VEC \geq 6.87$) [41].

This criterion is one of the most practical tools for predicting phase selection in multicomponent alloys. In contrast to entropy-based parameters, VEC reflects the physical mechanism of filling the electron states that stabilize either the close-packed FCC lattice or the more spaced BCC lattice [40].

1.2.2. Four core effects of HEAs

High Entropy Alloys are often described through four care effects that explain their behavior and distinguish them from conventional alloys. High entropy effect, sluggish diffusion, severe lattice distortion, and cocktail effect were proposed using theoretical and experimental studies to provide an explanation on the unexpected phase stability and mechanical properties of these alloys [37,39–41].

These effects are not only related to physical laws and do not necessarily apply equally to all systems, but they capture frequent observations across many HEAs. High entropy effect relates to the stabilization of simple solid solutions at elevated temperatures [39,40]. Sluggish diffusion refers to reduced atomic mobility in multicomponent alloys [41]. Severe lattice distortion describes the local structural irregularities produced by atomic size and chemical mismatch [40,41]. Finally, cocktail effect displays the properties obtained by complex, non-linear interactions between multiple principal elements [40,44].

These concepts are useful for analyzing HEA behavior, guiding alloy design, and explaining why these materials often exhibit unusual combinations of mechanical, thermal, and chemical properties. Also, these effects are complementary to the quantitative descriptors discussed in section 1.2.1 [40,41].

- **High Entropy Effect**

The high entropy effect is deeply linked to the configurational mixing entropy parameter discussed in section 1.2.1. In multicomponent alloys, the entropy term contributes significantly to the Gibbs free energy at high temperatures, favoring the formation of disordered solid solutions at large values, and promoting ordered intermetallics otherwise [39–41].

In early studies, it was suggested that sufficiently high mixing entropy could stabilize simple phases despite the chemical complexity of the composition [38,39]. However, recent studies showed that entropy alone does not dictate phase stability. The high entropy effect competes with enthalpic interactions, atomic size mismatch, and kinetic constraints, and its influence depends strongly on composition and temperature [40,41,44].

Now, instead of being considered a single-phase behavior factor, the high entropy effect is known to favor solid-solution formation when other conditions, such as moderate mixing enthalpy and limited size mismatch, are also satisfied [40,41].

- **Sluggish diffusion**

Sluggish diffusion effect was proposed to describe the reduced atomic mobility expected in multicomponent alloys where several elements occupy the same sublattice. The presence of many different atomic species, with distinct sizes and bonding characteristics, was hypothesized to increase the complexity of diffusion, thus slow down diffusion compared with conventional alloys [40,41]. It was also suggested that reduced atomic mobility would help stabilize high temperature solid solutions by limiting the formation of intermetallic phases [39,44].

However, later studies observed that, while some HEAs exhibit lower diffusion for certain elements or along specific crystallographic directions, others show diffusion rates comparable to or even higher than conventional alloys [37,40]. Thus, the sluggish diffusion effect is now seen as a behavior that depends strongly on composition, bonding environment, and local chemical order [41,44].

This concept is used to interpret phase stability and microstructural evolution in multicomponent systems. For some HEAs, reduced diffusion can suppress long-range ordering and slow down phase separation, particularly during short processing times or under non-equilibrium conditions as additive manufacturing [43]. It is also viewed as a useful conceptual tool for understanding kinetic effects in multicomponent alloys while acknowledging that diffusion behavior can vary between alloys [40].

- **Severe lattice distortion**

Severe lattice distortion refers to the stronger local distortions of the crystal lattice exhibited in multicomponent solid solutions. As illustrated in Figure 14, HEAs have several elements with different atomic radii and bonding characteristics which occupy random lattice sites. Thus, it generates fluctuations in local atomic spacing and elastic strain fields [40,41]. Unlike dilute alloys, surrounded mostly by atoms of a single element, HEAs form an environment with neighboring atoms which differ in size, electronegativity, and bonding strength, creating significant local variations [37,44].

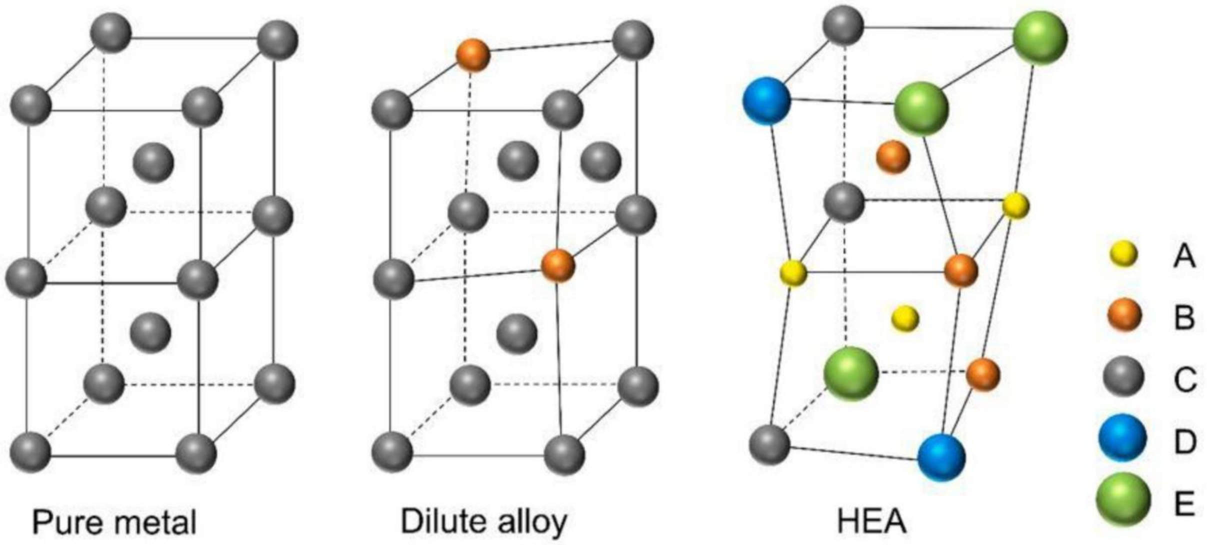

These local distortions influence the mechanical and physical behavior of HEAs in several ways. In a mechanical point of view, lattice distortions act as obstacles to dislocation motion,

Figure 14: Schematic representation of lattice distortion in BCC pure metals, conventional dilute alloys and HEAs, with different elements from A to E [73]

increasing solid-solution strengthening beyond what is typically observed in dilute alloys [40,41]. This effect is suggested to be one of the main reasons why many HEAs exhibit high strength combined with good work-hardening ability, particularly at low temperatures [40,44].

At atomic scale, lattice distortion modifies local bonding energies and may change the thermodynamics of phase stability. It can stabilize disordered solid solutions by increasing the energetic penalty associated with forming ordered structures, although the magnitude of this effect is composition-dependent and not universally dominant [40,41]. In some HEAs, particularly those with large atomic size mismatches (high δ parameter), severe distortion was linked to sluggish grain growth and resistance to recrystallization due to the high stored elastic strain around solute atoms [40,43].

Severe lattice distortion should not be viewed as a uniform or homogeneous effect but more as a local phenomenon whose intensity varies with chemical complexity, size mismatch, and short-range order. Overall, this effect describes how the multicomponent nature of HEAs generates locally strained atomic environments that strengthen the alloy, influence deformation mechanisms, and contribute to phase stability [40,41].

- **Cocktail effect**

The cocktail effect is a conceptual idea used to describe the properties obtained by the combination of multiple principal elements in comparable proportions. In contrast to conventional alloys, where solute additions typically change a dominant base element property, the behavior of HEAs often reflects non-linear or synergistic interactions between multiple constituents [39–41]. As a result, the properties of HEAs cannot be predicted as a simple weighted average of the properties of the individual elements [37,44].

Multiple mechanisms may contribute to the alloy properties. The electronic structure, bonding characteristics, and local chemical environment are influenced by the presence of multiple principal elements [40,41]. The cocktail effect is not a single physical mechanism but rather a description of how multiple factors act together, including lattice distortion, entropy contributions, and thermodynamics interactions, to produce material behavior that is difficult to attribute to a single added element [40,44].

Because of its complexity, the cocktail effect is often considered a qualitative guiding concept rather than a quantitative design rule. Overall, the cocktail effect reflects the idea that multicomponent alloys explore regions of composition space where collective interactions dominate, leading to unexpected or enhanced properties [41,44]. While it is difficult to formalize and predict, it remains valuable as a conceptual framework for motivating HEA research and explaining why these alloys can outperform conventional materials.

1.2.3. Phase formation in HEAs and corrosion behavior

Phase formation in HEAs is influenced by competing thermodynamic and electronic factors that produce solid solutions, ordered phases, or multiphase microstructure depending on composition. Early studies showed that chemically complex systems often stabilize into simple FCC and BCC lattices, despite their high number of alloying elements. This behavior is largely attributed to a balance between mixing enthalpy, configurational entropy, and electronic structure [40,41].

FCC phases are typically observed in systems with high valence electron concentration (VEC), limited atomic size mismatch, and moderately negative mixing enthalpies. Alloys from the Co-Cr-Fe-Mn-Ni family, such as the Cantor alloy, commonly form FCC [38,41]. These FCC solid solutions are not only ductile but also generally provide good corrosion resistance. This is due to their homogeneous chemistry promoting stable passive film formation, especially in Cr-containing HEAs.

In contrast, BCC phases are stabilized in alloys with lower VEC values, strong atomic size mismatch, or highly refractory elements such as Nb, Ta, and Mo [40,42]. Al additions, common in corrosion focused HEAs, also often shift the structure from FCC to BCC or dual FCC+BCC configurations. This transition is associated with increased chemical heterogeneity and may influence oxidation and corrosion response depending on the stability of Al-rich or Cr-rich passive layers [40,41].

Ordered phases such as B2 (ordered BCC) and $L1_2$ (ordered FCC) may also form when specific pairs of elements have strongly negative mixing enthalpies. These phases modify both mechanical and corrosion behavior. This leads to localized ordering or segregation that can create micro-galvanic couples, affect passive film composition, and introduce preferential dissolution zones, especially under additive manufacturing’s rapid solidification conditions [40,43].

From a corrosion perspective, phase formation is very important as corrosion resistance in HEAs depends strongly on multiple factors. Chemical homogeneity, as single-phase solid solutions typically corrode more uniformly. Elemental partitioning, such as the segregation of Al, Cr, or Mo, affects passive film quality [40,41,43]. Presence of ordered or secondary phases, which may act as anodic or cathodic sites. Finally, short-range order, which can influence passive film composition and protectiveness [40,41].

Overall, even though HEAs are defined structurally and thermodynamically, their corrosion behavior is closely related to phase stability. Thus, FCC structure favoring homogeneous passive layers, or Al-induced BCC/B2 phases affecting oxidation behavior, are useful guidelines for designing corrosion-resistant HEAs [40,41].

2. Materials and Methods

This section is dedicated to describing the different materials and equipment, and the methodology that were used during this study. Hereunder the different powders and powders mixtures will be detailed as well as the outcoming samples, along with the instruments used for their creation and characterization.

2.1. Base Powders

To achieve an alloy with high corrosion resistance, multiple elements are selected. Aluminum (**Al**), Chromium (**Cr**), Iron (**Fe**), Manganese (**Mn**) and Nickel (**Ni**) were chosen based on their influence on the microstructure and the properties of the alloys.

Powders of SS 316L, and Nickel-Chromium (80-20 wt. %) alloys were employed for their high concentration of the selected elements, as detailed in Table 2. To adjust the composition, Al and Mn elemental powders were used.

Table 2: Chemical Composition in wt.% of 316L & Ni-Cr powders

Powder	**Composition Wt.%**										
316L	**Cr**	**Fe**	**Mn**	**Ni**	**Mo**	**C**	**N**	**O**	**P**	**Si**	**S**
	17.6	65.72	0.91	12.6	2.34	0.02	0.09	0.03	0.01	0.67	<0.01
Ni-Cr	**Cr**	**Fe**	**Mn**	**Ni**	**Mo**	**C**	**N**	**O**	**P**	**Si**	**S**
	19.45	0.47	0.01	78.78	-	0.02	-	-	-	1.06	<0.01

The morphology of the 316L, Ni-Cr and Al powders is spherical, and Mn elemental powder has an irregular morphology, as shown in Figure 15.

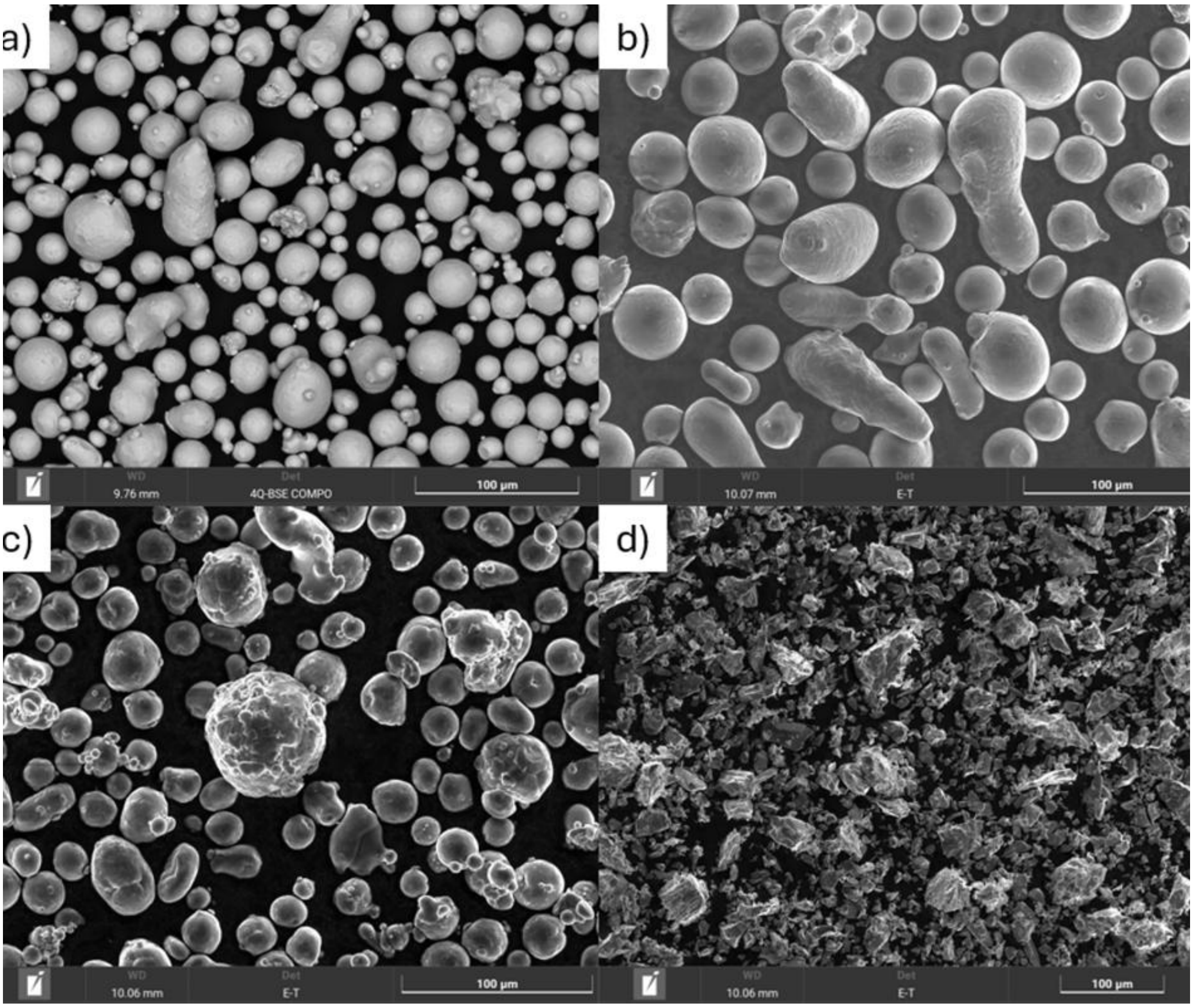

Figure 15: SEM micrographs of powders: (a) 316L, (b) Ni-Cr, (c) Al, and (d) Mn

The size range of the powders was provided by the suppliers (Table 3). The powders used in this study were all fabricated using gas-atomization. The suppliers are Carpenter Additive© for the 316L, and Nanografi© for the Ni-Cr, Al, and Mn powders. Further information can be found in Appendix A – Product sheet of SS 316L powder, and Appendix B – Product sheet of Ni-Cr, Mn, and Al powders.

Table 3: Powder size ranges of selected powders

Powder	**316L**	**Ni-Cr**	**Al**	**Mn**
Size	15-53 µm	15-53 µm	20-35 µm	44-53 µm

2.2. Powder Preparation

2.2.1. Preparation for Differential Thermal Analysis (DTA)

DTA samples were prepared using around 700mg of powders mixture for each composition (Table 4) and mixed for a few minutes.

Table 4: DTA compositions tested

Chemical Formula	**Composition at. %**							
$CrFe_{2.11}MnNi_2$	**Al**	**Cr**	**Fe**	**Mn**	**Ni**	**Mo**	**Si**	**S**
	-	16.09	33.96	16.09	32.17	0.704	0.688	0.007
$Al_{0.25}Cr_{1.25}Fe_{2.5}MnNi_{2.62}$	**Al**	**Cr**	**Fe**	**Mn**	**Ni**	**Mo**	**Si**	**S**
	3.225	16.13	32.26	12.9	33.87	0.668	0.654	0.007
$Al_{0.39}Cr_{1.11}Fe_{2.22}MnNi_{2.33}$	**Al**	**Cr**	**Fe**	**Mn**	**Ni**	**Mo**	**Si**	**S**
	5.426	15.5	31.01	13.95	32.56	0.643	0.629	0.007
$Al_{0.86}Cr_{1.43}Fe_{2.86}MnNi_3$	**Al**	**Cr**	**Fe**	**Mn**	**Ni**	**Mo**	**Si**	**S**
	9.23	15.39	30.77	10.77	32.31	0.638	0.624	0.007

2.2.2. Preparation for Laser Powder Bed Fusion (LPBF)

Single track experiment was performed on $CrFe_{2.11}MnNi_2$ using a 1kg powders mix detailed in Table 5. The powders were weighed individually, added successively to the mixture, and hand-mixed for 2 hours.

Table 5: Powder quantity used in 1kg powders mix for single track $CrFe_{2.11}MnNi_2$

Powder	$CrFe_{2.11}MnNi_2$
	Quantity (g)
316L	515.6
Ni-Cr	301.8
Mn	153.96

For LPBF cubic samples printing of $1cm^3$, $CrFe_{2.11}MnNi_2$, and $Al_{0.25}Cr_{1.25}Fe_{2.5}MnNi_{2.62}$ were both used. Powders mixtures of 2.7kg each were prepared as detailed in Table 6. The powders were weighed individually, added successively to the mixture, and hand-mixed for 2 hours.

Table 6: Powder quantity used in 2.7kg powders mixtures for cubic samples printing of $CrFe_{2.11}MnNi_2$ and $Al_{0.25}Cr_{1.25}Fe_{2.5}MnNi_{2.62}$

Powder	$CrFe_{2.11}MnNi_2$	$Al_{0.25}Cr_{1.25}Fe_{2.5}MnNi_{2.62}$
	Quantity (g)	**Quantity (g)**
316L	1 392.2	1 342.96
Ni-Cr	814.96	897.3
Mn	415.7	336.7
Al	-	42.9

2.3. Sample Production

2.3.1. Differential Thermal Analysis (DTA)

Netzsch - STA 449 C Jupiter Thermo-microbalance (Figure 16), was used for differential thermal analysis. This device allows precise temperature control and monitoring over a wide range, from ambient temperature to 1550°C using integrated thermocouples for direct temperature measurement [45]. This system is equipped with mass flow controllers that enable control of the experimental atmosphere. Argon (Ar) was used as the purge and protective gas to ensure an inert environment.

Figure 16: Netzsch-Gerätebau GmbH - STA 449 C Jupiter Thermo-microbalance [45]

In DTA, both the sample and an inert reference material are subjected to the same controlled temperature program. The thermal behavior of the sample is then compared to that of the reference by continuously recording the temperature difference between them as heating or cooling occurs. When the sample undergoes a physical or chemical transition, such as melting, crystallization, oxidation, or decomposition, its temperature deviates from that of the reference, producing a peak on the DTA curve.

The DTA curve is a plot of the temperature difference with respect to the time or temperature. A positive peak indicates an exothermic reaction (heat release), while a negative peak represents an endothermic reaction (heat absorption). Each peak corresponds to the start of a thermal event, while the area under the peak is proportional to the heat involved in the process. This method serves to identify phase transformation, reaction temperatures, and to study the thermal stability of materials.

For this study, DTA measurements were carried out with a heating rate of 5°C/min up to 1550°C, followed by cooling at the same rate to ambient temperature. The tested compositions are listed in Table 4.

2.3.2. **Laser Powder Bed Fusion (LPBF)**

LPBF single tracks and printed cubic samples were fabricated using the Aconity MINI LPBF printer (Figure 17). This device is used for weldable metallic component printing using raw metallic powders [46].

Figure 17: Aconity MINI LPBF printer [46]

The Aconity MINI has a build space of 140mm in diameter by 190mm in height, with access to a large variety of process parameters for fast part production or small batches. Its gas tight design, inert gas (argon), and recirculation system allows to precisely control the environment for processing of highly reactive materials or weld fumes [46].

The device is equipped with the Aconity Studio Control Software which allows the control of the processing parameters and environmental conditions [46].

For further information, the technical specifications of the Aconity MINI can be found in Table 7.

Table 7: Aconity MINI specifications [46]

Build Space	Ø 140 x H 190 mm^3
Laser Configuration	Single Mode 200W
Optics Configuration / Spot Size	F-Theta / 80 µm
Build plate preheating Temperature	500 °C / Ø 140 x H 150 mm^3
Layer Thickness	Down to 10 µm
Maximum Scan Speed	12 m/s
Inert Gas Type / Pressure	Argon 4.6 / 6 bar
Inert Gas Consumption	< 5 l/min during process < 60 l/min during purging
Residual Oxygen Content	< 100 ppm
Applicable Materials	All weldable materials

2.3.2.1. **Single Track**

Single track experiments were conducted on $CrFe_{2.11}MnNi_2$ to determine optimal laser scan speed and laser power ranges for printing, using a 1kg powders mixture (Table 5). Other printing parameters were kept constant, with a laser spot size of 80 µm, hatch distance of 100µm, layer thickness of 30µm, supply factor of 3, 67°–67° unidirectional scan strategy, build plate preheating temperature of 500°C, and an argon gas flow of 2m/s.

53 tracks were performed using different combinations of scan speed and laser power, shown in Figure 18. Scan speed ranges from 200 to 2,000 mm/s while laser power ranges from 100 to 200W. These parameters led to linear energy densities (equation (1)) varying from 0.0625 to 1J/mm. The different parameter sets of scanning speed, power, and linear energy densities can be found in Appendix C – Table of single-track parameter sets.

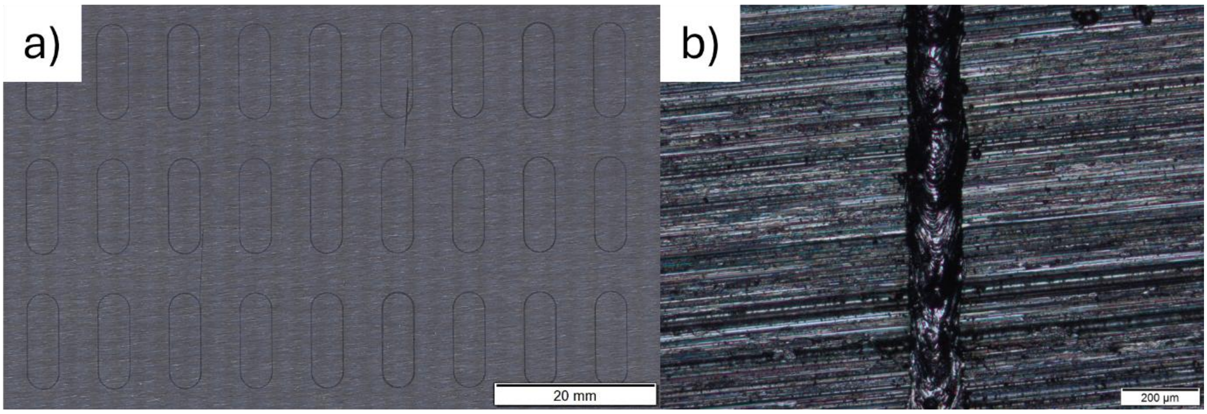

Figure 18: (a) Overview of the upper section of the single-track array, and (b) close-up of a melt track (100W|200mm/s) of $CrFe_{2.11}MnNi_2$ alloy

2.3.2.2. **Cubic Samples**

Two batches of $1cm^3$ cubic samples were printed using $CrFe_{2.11}MnNi_2$ and $Al_{0.25}Cr_{1.25}Fe_{2.5}MnNi_{2.62}$ compositions (Table 4), for which 2.7kg powders mixtures were prepared per composition (Table 6). A batch of cubic samples is composed of 20 cubic samples with sides of 10mm, as presented in Figure 19.

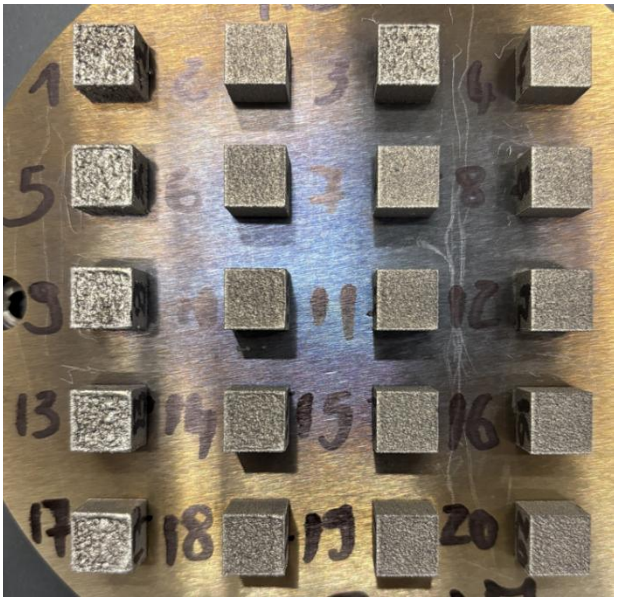

Figure 19: Overview of the 20 Al0.25Cr1.25Fe2.5MnNi2.62 cubic samples

For cubic samples printing, multiple parameters are kept constant across the entire batch. These include a laser spot size of 80µm, a hatch distance of 100µm, a layer thickness of 30µm, a supply factor of 3, a 67°-67° unidirectional scan strategy, a 500°C preheating of the build plate, and a 2m/s argon gas flow. Each cubic sample differs based on the sets of laser scan speed and laser power, which are based on the analysis of the single tracks. The selected laser scan speed and power ranges for $CrFe_{2.11}MnNi_2$ cubic samples vary from 200 to 1,000mm/s in scan speed and between 100 to 200W for laser power. The sets of parameters as well as the volumetric energy densities (equation (2)) for $CrFe_{2.11}MnNi_2$ cubic samples printing are detailed in Table 8.

Table 8: Printing Parameters for CrFe2.11MnNi2 Cubic Samples

Sample	Laser Power P [W]	Laser Scan Speed V_s [mm/s]	Volumetric Energy Density E_d [J/mm^3]
1	100	200	166.7
2	100	400	83.3
3	125	400	104.2
4	125	600	69.4
5	150	200	250.0
6	150	400	125.0
7	150	600	83.3
8	150	800	62.5
9	175	200	291.7
10	175	400	145.8
11	175	600	97.2
12	175	800	72.9
13	175	1000	58.3
14	185	400	154.2
15	185	600	102.8
16	185	800	77.1
17	200	200	333.3
18	200	400	166.7
19	200	600	111.1
20	200	800	83.3

Based on the analysis of the $CrFe_{2.11}MnNi_2$ cubic samples, the laser powers and scan speeds were modified to achieve better surface finish and higher densities. For the $Al_{0.25}Cr_{1.25}Fe_{2.5}MnNi_{2.62}$ cubic samples printing, laser power varies from 100 to 200W and the scanning speed varies from 400 to 1,000mm/s, as seen in Table 9.

Table 9: Printing Parameters for the $Al_{0.25}Cr_{1.25}Fe_{2.5}MnNi_{2.62}$ Cubic Samples

Sample	Laser Power P [W]	Laser Scan Speed V_s [mm/s]	Volumetric Energy Density E_d [J/mm^3]
1	100	400	83.3
2	100	600	55.6
3	125	400	104.2
4	125	600	69.4
5	150	400	125.0
6	150	600	83.3
7	150	800	62.5
8	150	1000	50.0
9	175	400	145.8
10	175	600	97.2
11	175	800	72.9
12	175	1000	58.3
13	185	400	154.2
14	185	600	102.8
15	185	800	77.1
16	185	1000	61.7
17	200	400	166.7
18	200	600	111.1
19	200	800	83.3
20	200	1000	66.7

2.4. Pycnometer Analysis

Surface densities of the cubic samples were measured using a gas pycnometer, the AccuPyc II Series 1345 Pycnometer, shown in Figure 20. This device determines material density using the gas displacement method. This process consists of a precisely calibrated chamber, into which a sample is placed, which is filled with a small volume of inert gas, which is helium in this study. Measurements are based on the pressure variation resulting from gas expansion into the known volume of the chamber to compute the sample's volume according to Boyle's law. The measured volume can then be combined with the sample's mass to obtain its density [47].

Figure 20: AccuPyc II Series 1345 gas Pycnometer
[47]

Each measurement is repeated 5 times to compute an average value and minimize experimental variability.

The density of the powder's mixtures (ρ_{mix}) used to produce the samples were also measured to compute the relative density of each sample, using equation 10.

$$\% \, Relative\ Density = \frac{\rho_{sample} \cdot 100}{\rho_{mix}} \tag{10}$$

With,

- ρ_{sample}: density of a cubic sample (g/cm^3)
- ρ_{mix}: density of the powders mix used for printing (g/cm^3)

2.5. Profilometer Analysis

The surface profile and roughness of the samples were measured using a 3D optical surface measurement profilometer, the Alicona InfiniteFocus G5 profilometer (Figure 21).
This device uses a focus variation method, a non-contact optical method that combines the small depth of focus of an optical system with vertical scanning to generate precise 3D surface topography [48]. The system uses a coaxial LED light source coupled with an optical microscope with various interchangeable objective lenses (2.5x, 5x, 10x, 20x, 50x, and 100x magnifications) for large area overviews and detailed micro-scales analyses [48]. The integrated Alicona MeasureSuite software allows the control of a motorized x-y stage and a high-precision z-axis drive [48]. This software enables fully automated surface reconstruction, and the computation of dimensional and roughness parameters [48].

Figure 21: Alicona InfiniteFocus G5 profilometer [48]

Measurements were performed on each sample using the 100x magnification lens to reconstruct a three-dimensional surface profile of the top layer of the 1cm^3 cubic samples. The resulting topographical data were analyzed to determine quantitative roughness parameters such as the height distribution, the average roughness (R_a), and the peak-to-valley height (R_z).

2.6. Microstructure characterization

2.6.1. Sample preparation

In order to perform microstructural characterization, the samples were sectioned along the building direction using spark erosion machining with a Charmilles Technologies Robofil 310 [49]. The samples were then mounted in Bakelite cylinders using the STRUERS Citopress-1 (Figure 22), then polished using STRUERS Tegramin-30 machines (Figure 22).

Figure 22: (left) STRUERS Citopress-1 and (right) STRUERS Tegramin-30 [50]

The polishing procedure begins with a pre-polishing using silicon carbide (SiC) abrasive papers of 400, 800, and 1,200 grit, each applied for 1 minute under water and at a rotational speed of 200rpm.

Final polishing was performed using synthetic polishing cloths combined with diamond suspension solutions at a rotational speed of 150 rpm. The MD Dac cloth with a 9 µm diamond suspension was first used for 3 minutes, followed by the MD Nap cloth with a 3 µm diamond suspension for 3 minutes. The third step employed the MD Nap cloth with a 1 µm diamond suspension for 2 minutes, and the final polishing was carried out using the MD Chem cloth with OPS (oxide polishing suspension) for 10-20 minutes. All consumables were supplied by STRUERS [50].

For Selective Electron Microscopy (SEM), the samples were coated with conductive silver paint to ensure electrical continuity between the sample surface and the metallic holder, as shown in Figure 23.

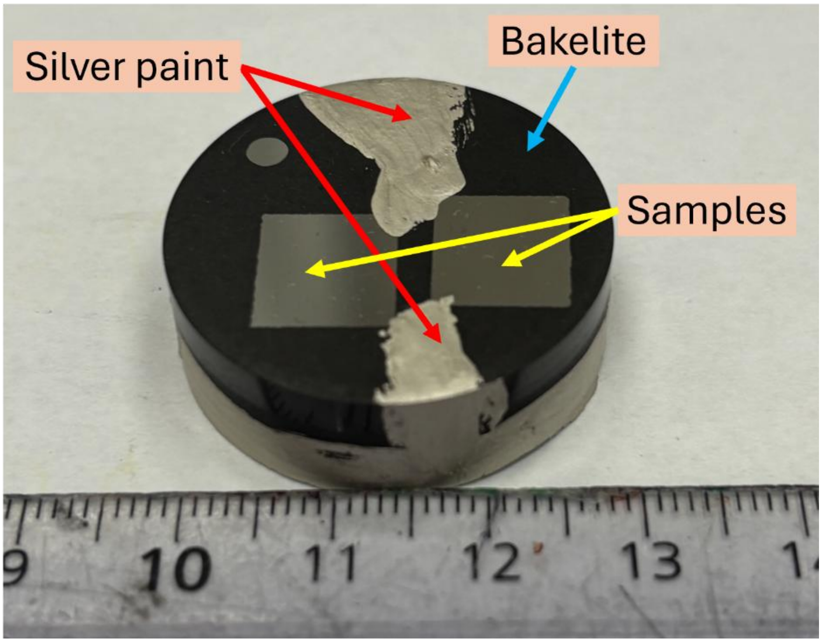

Figure 23: Sample prepared for SEM, in Bakelite and with silver paint

2.6.2. Optical Microscope (OM) and stream analysis software

Preliminary defect identification and porosity assessment were performed using an Olympus BX60 optical microscope and its integrated Stream Analysis Software [51]. The BX60 microscope is a reflected/transmitted-light optical microscope with interchangeable objective lenses and a digital camera module for live image capture and analysis.

The device was used for general overviews of the samples and detailed images at magnifications of 2.5x, 5x, 10x, 20x, and 50x. The Stream Analysis Software was used for image acquisition, processing, and semi-quantitative analysis in the case of porosity measurement using the phase fraction estimation tool based on color contrast, with manually adjusted image segmentation and thresholding. The resulting optical images provided qualitative identification of visible defects and allowed semi-quantitative estimation of porosity.

2.6.3. Scanning Electron Microscope (SEM)

The Tescan Clara Ultra-High-Resolution Scanning Electron Microscope (UHR-SEM), on Figure 24, was used to obtain micron-scale images of the samples for surface and microstructural characterization. The Clara system is designed for high-resolution imaging using a field-emission electron source and multiple analytical detectors for compositional and crystallographic analysis.

Figure 24: Tescan Clara Ultra-High-Resolution Scanning Electron Microscope [74]

Images were primarily acquired using Back-Scattered Electron (BSE) mode which enhances compositional contrast based on atomic number differences. Additional analyses were performed using Energy-Dispersive X-ray Spectroscopy (EDS) for elemental identification and mapping, Wavelength-Dispersive X-ray Spectroscopy (WDS) for high precision elemental analysis with improved spectral resolution compared to EDS, and Electron Back-Scattered Diffraction (EBSD) to determine grain orientation, phase distribution and crystallographic texture.

3. Results

This chapter presents the experimental and numerical results obtained during this study. The results are organized in chronological order, from the powders and mixture optimization to the samples characterization.

3.1. Powders selection and mixture optimization

3.1.1. Mixture oriented powders selection and final compositions selection

This section presents the results of the compositional and powder selection optimization process that led to the definition of the four alloy compositions investigated in this study.
The optimization was based on a filtering strategy starting from an initial compositional space which included all possible combinations of Al, Cr, Fe, Mn, Ni, and Mo with predominant face-centered cubic (FCC) phase stability. Also, aluminum was the only element allowed to be absent, to consider both Al-containing and Al-free alloys.

Throughout this work, alloy compositions are expressed using a Mn-normalized stoichiometric notation, where each elemental coefficient represents the number of moles of that element per 1 mole of Mn.

First, the feasible compositions were filtered based on their predicted phase constitution, keeping only those with high FCC phase fraction. This initial screening was performed by established empirical phase-stability criteria commonly used HEAs design, including the valence electron concentration (VEC), atomic size mismatch (δ), and thermodynamic stability parameters (as Ω), defined in section 1.2.1, which are known to correlate with FCC, BCC, or mixed phase formation. According to these criteria, FCC solid solutions are generally favored for VEC values above 8, low atomic size mismatch, and sufficiently high Ω values, whereas increasing aluminum content progressively stabilizes BCC/B2 phases.

Based on these criteria, different FCC phase fraction thresholds were defined depending on the aluminum atomic fraction. For Al-free compositions, only fully FCC alloys were retained. For compositions with intermediate aluminum contents ($0.05 \leq \text{Al} \leq 0.4$), a stricter criterion of 98 vol. % of FCC fraction was applied. For higher aluminum contents ($0.45 \leq \text{Al} \leq 0.7$), where partial BCC/B2 stabilization is expected due to aluminum's strong BCC-stabilizing effect, compositions exhibiting FCC fractions above 85 vol. % were considered. The screening was then further refined using Thermo-Calc, a calculation of phase diagram software (CALPHAD), employing the TCHEA database, to make prediction of equilibrium phase fractions as a function of composition.

In a second step, the remaining compositions were further refined based on their elemental concentrations to comply with the definition of compositionally complex alloys (CCAs), characterized by multiple principal elements within defined atomic fraction ranges. CCAs are defined as alloys containing multiple principal elements (≥ 4), each with an atomic fraction typically between 5 and 35 at., ensuring the absence of a dominant base element and enabling non-equiatomic yet compositionally complex designs.

Finally, an additional selection step was performed based on mixture optimization constraints. To improve powder homogeneity and spreadability, the remaining compositions were evaluated with respect to practical mixing considerations, including the minimization of the number of different powders required, the maximization of individual powder utilization, and the compatibility with a commercially available Ni-Cr powder. This final filtering step resulted in the selection of four compositions retained for experimental investigations.

Table 10 presents the target alloy compositions obtained after filtering, together with the corresponding compositions achievable using the selected powder mixing strategy based on a commercially available Ni-Cr (80-20) powder.

Table 10: Theoretical atomic percentages of Al, Cr, Fe, Mn, Ni, and Si elements in each tested composition using different powder-mixing strategies

Powder Mixing strategy	Composition	Al [at. %]	Cr [at. %]	Fe [at. %]	Mn [at. %]	Ni [at. %]	Si [at. %]
Target	**$CrFe_{2.11}MnNi_2$**	-	16.086	33.96	16.086	32.172	0.688
	$Al_{0.25}Cr_{1.25}Fe_{2.5}MnNi_{2.62}$	3.225	16.129	32.259	12.904	33.871	0.654
	$Al_{0.39}Cr_{1.11}Fe_{2.22}MnNi_{2.33}$	5.426	15.504	31.009	13.954	32.559	0.629
	$Al_{0.86}Cr_{1.43}Fe_{2.86}MnNi_3$	9.23	15.385	30.77	10.77	32.308	0.624
Cr-stoichiometric	**$CrFe_{2.11}MnNi_2$**	-	16.47	34.91	16.47	29.53	1.357
	$Al_{0.25}Cr_{1.25}Fe_{2.5}MnNi_{2.62}$	3.31	16.55	33.26	13.24	31.24	1.380
	$Al_{0.39}Cr_{1.11}Fe_{2.22}MnNi_{2.33}$	5.56	15.90	31.94	14.31	29.99	1.325
	$Al_{0.86}Cr_{1.43}Fe_{2.86}MnNi_3$	9.46	15.77	31.68	11.03	29.77	1.315

3.1.2. Multiple powder hand mixing induced deviation

Table 11 presents the theoretical chemical compositions of the powder mixtures obtained through manual mixing, as calculated from the nominal compositions and mass fractions of the individual powders.

Table 11: Theoretical atomic percentages of Al, Cr, Fe, Mn, Ni, and Si elements obtained for each tested composition after hand mixing of powders

Composition	Al [at. %]	Cr [at. %]	Fe [at. %]	Mn [at. %]	Ni [at. %]	Si [at. %]
$CrFe_{2.11}MnNi_2$	-	16.5	34.97	16.5	29.61	1.36
$Al_{0.25}Cr_{1.25}Fe_{2.5}MnNi_{2.62}$	3.31	16.55	33.25	13.24	31.26	1.36
$Al_{0.39}Cr_{1.11}Fe_{2.22}MnNi_{2.33}$	5.56	15.89	31.93	14.30	30.01	1.32
$Al_{0.86}Cr_{1.43}Fe_{2.86}MnNi_3$	9.46	15.76	31.68	11.04	29.78	1.31

Table 12 summarizes the elemental content differences between the actual compositions of the manually mixed powders and the corresponding target compositions.

Table 12: Differences in atomic composition between the actual compositions obtained after hand mixing and the corresponding target compositions

Composition	ΔAl [at. %]	ΔCr [at. %]	ΔFe [at. %]	ΔMn [at. %]	ΔNi [at. %]	ΔSi [at. %]
$CrFe_{2.11}MnNi_2$	-	+0.41	+1.01	+0.41	−2.57	+0.67
$Al_{0.25}Cr_{1.25}Fe_{2.5}MnNi_{2.62}$	+0.06	+0.46	−0.71	−0.85	−0.91	+0.67
$Al_{0.39}Cr_{1.11}Fe_{2.22}MnNi_{2.33}$	+0.07	−0.20	−2.03	−1.79	−2.16	+0.63
$Al_{0.86}Cr_{1.43}Fe_{2.86}MnNi_3$	+0.06	−0.33	−2.28	−3.05	−2.39	+0.62

Close values between the target and the achieved compositions are obtained for some elements, while larger deviations are observed for others. The aluminum and chromium contents remain very close to the targets in all Al-containing alloys with differences of less than

0.5 at. %. In contrast, nickel is systematically lower than the target values for all compositions, with deviations ranging from around 1 to 2.6 at. %.

The largest deviations are observed for iron and manganese depending on the selected composition, with iron deviations ranging from about 1 to 2.3 at. % and Mn from around 0.4 to 3 at. %. Finally, silicon shows a consistent positive offset for all alloys, which corresponds to doubling in the content from a relative point of view.

3.1.3. Thermo-Calc Predictions

Thermodynamic calculations were performed using Thermo-Calc, a CALPHAD based computational software for predicting phase stability in multicomponent alloys. In this study, Thermo-Calc was used, employing the High Entropy Alloys database, to compute equilibrium phase fractions of the selected compositions under equilibrium conditions, enabling the identification of stable phases as a function of composition. This provided guidance for composition screening and selection.

Table 13 shows the equilibrium phase fraction predictions obtained using Thermo-Calc for the selected alloy compositions at a pressure of 100,000 Pa and a temperature of 1,000°C.

Table 13: Thermo-Calc equilibrium phase fractions predictions (vol. %) at 100,000 Pa and 1,000°C

Phase	FCC [vol. %]	BCC/B2 [vol. %]	AlN [vol. %]	M23C6 [vol. %]	σ [vol. %]
$CrFe_{2.11}MnNi_2$	100	-	-	-	-
$Al_{0.25}Cr_{1.25}Fe_{2.5}MnNi_{2.62}$	99.63	-	0.36	0.01	-
$Al_{0.39}Cr_{1.11}Fe_{2.22}MnNi_{2.33}$	99.64	-	0.35	0.01	-
$Al_{0.86}Cr_{1.43}Fe_{2.86}MnNi_3$	79.98	17.47	0.34	0.08	2.13

For the Al-free composition ($CrFe_{2.11}MnNi_2$), a fully FCC equilibrium state is predicted under the equilibrium conditions investigated. Alloys with low aluminum content ($Al_{0.25}Cr_{1.25}Fe_{2.5}MnNi_{2.62}$ and $Al_{0.39}Cr_{1.11}Fe_{2.22}MnNi_{2.33}$) also exhibit predominantly FCC phase stability, with minor fractions of secondary phases below 0.4 vol. %.

In contrast, the alloy with the highest aluminum content ($Al_{0.86}Cr_{1.43}Fe_{2.86}MnNi_3$) shows a more complex equilibrium phase constitution, characterized by a reduced FCC fraction (around 80 vol. %), the presence of a BCC/B2 phase (around 17 vol. %) and secondary phases including a σ phase at around 2 vol. %.

3.2. Differential Thermal Analysis measurements

This section presents the results obtained from Differential Thermal Analysis (DTA) performed on the four selected alloy compositions. The thermal behavior of each alloy is first described based on the DTA curves, with a focus on cooling and its peaks. These peaks are used to identify the main thermal events occurring during solidification and solid-state transformations.

In addition, the microstructures resulting from the DTA thermal cycles are characterized by observing the phases present at room temperature. Phase identification is performed through microstructural observations, focusing on the presence and distribution of FCC, BCC/B2, and secondary phases. Elemental distribution within the different phases was also investigated using energy-dispersive X-ray spectroscopy (EDX), including elemental mapping and point analysis.

3.2.1. DTA curves

Figure 25 presents the DTA cooling curves recorded at a cooling rate of 5°C/min for the four selected alloy compositions. Heating curves are not shown in this work, as the analysis focuses exclusively on the cooling segments in order to explain the solidification path and phase formation sequence. The curves exhibit multiple exothermic events occurring at different temperature ranges specified in Table 14, corresponding to successive thermal transformations during solidification and subsequent phase formation.

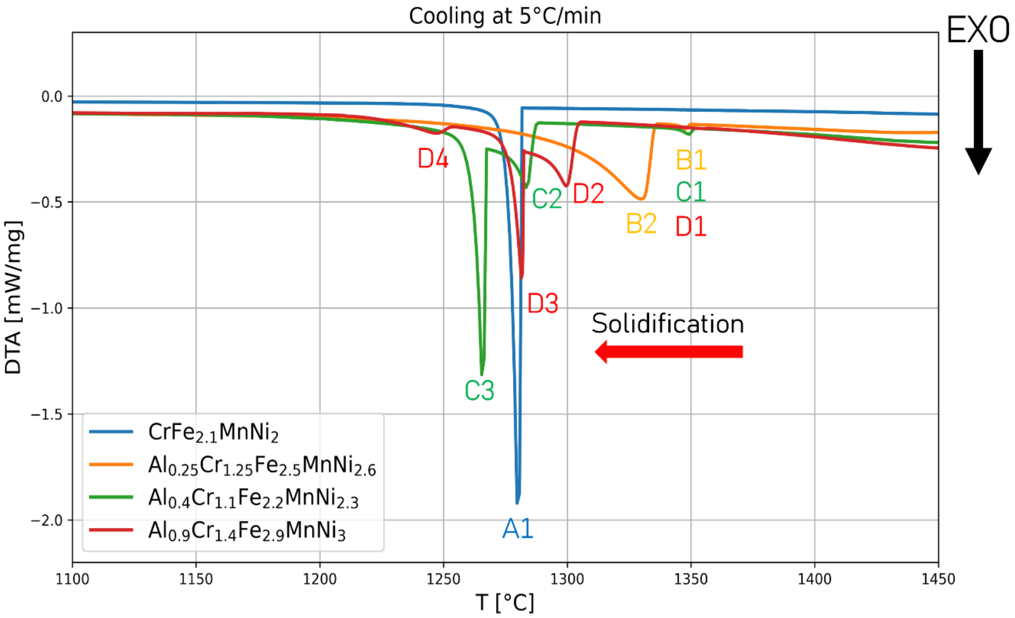

Figure 25: DTA cooling curves at 5°C/min for $CrFe_{2.1}MnNi_2$, $Al_{0.25}Cr_{1.25}Fe_{2.5}MnNi_{2.6}$, $Al_{0.4}Cr_{1.1}Fe_{2.2}MnNi_{2.3}$, and $Al_{0.9}Cr_{1.4}Fe_{2.9}MnNi_3$

The temperature with the onset and completion of these thermal events, together with the corresponding phase transformations, are summarized in Table 14.

Table 14: Principal cooling peaks for $CrFe_{2.1}MnNi_2$, $Al_{0.25}Cr_{1.25}Fe_{2.5}MnNi_{2.6}$, $Al_{0.4}Cr_{1.1}Fe_{2.2}MnNi_{2.3}$, and $Al_{0.9}Cr_{1.4}Fe_{2.9}MnNi_3$ DTA samples

Peak	**Start Temperature [°C]**	**End Temperature [°C]**	**Reaction or phase transformation**
A1	1273	1261	Liquid (L_0) → **FCC**
B1	1350	1343	Liquid (L_0) → **Iron oxides** + L_1
B2	1336	1318	Liquid (L_1) → **FCC**
C1	1345	1335	Liquid (L_0) → **Iron oxides** + L_1
C2	1292	?	Liquid (L_1) → **FCC** + L_2
C3	?	1260	Liquid (L_2) → **BCC/B2**
D1	1348	1353	Liquid (L_0) → **Iron oxides** + L_1
D2	1305	?	Liquid (L_1) → **FCC** + L_2
D3	?	1272	Liquid (L_2) → **BCC/B2** + L_3
D4	1255	1246	Liquid (L_3) → **Intermetallics**

For all compositions, the first major exothermic peak is associated with the primary solidification of the liquid phase into an FCC structure. Depending on the alloy composition, additional exothermic peaks are observed at higher or lower temperatures, indicating the occurrence of intermediate reactions involving the remaining liquid fractions (L_1, L_2, and L_3) and the formation of additional solid phases.

It is observed that the number, position, and intensity of the cooling peaks vary among the four alloys. Alloys with higher aluminum content exhibit a more complex thermal response, characterized by multiple exothermic events. The relative intensity of the DTA peaks is discussed qualitatively and should not be directly correlated with the amount of phase formed, as peak intensity is influenced by kinetic and thermal factors in addition to phase fraction.

3.2.2. DTA samples microstructures

Figure 26 shows an SEM micrograph of the $CrFe_{2.1}MnNi_2$ sample after DTA. The microstructure appears homogeneous over the observed area and is characterized by a single-phase morphology. The absence of compositional contrast suggests a fully FCC microstructure.

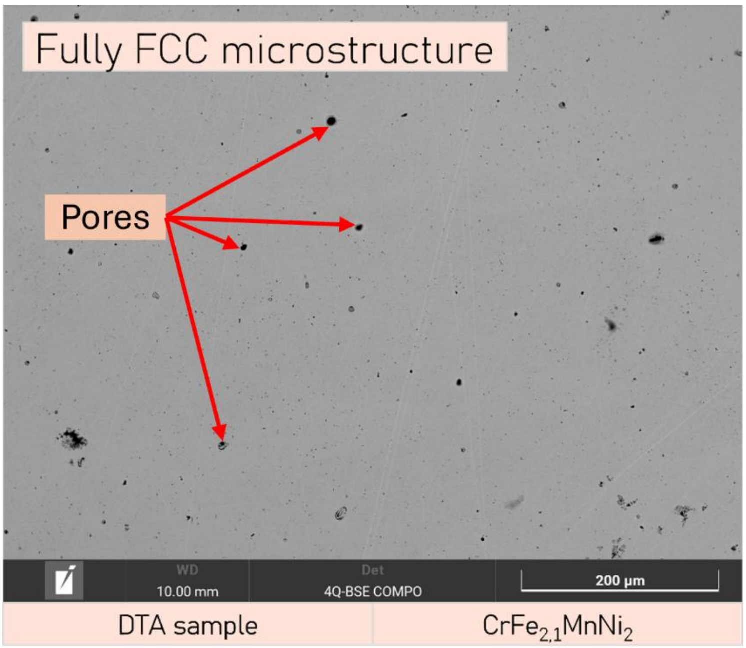

Figure 26: SEM-micrograph of $CrFe_{2.1}MnNi_2$ DTA sample

Figure 27 presents SEM micrographs of the $Al_{0.25}Cr_{1.25}Fe_{2.5}MnNi_{2.6}$ DTA sample at two magnifications. The microstructure is predominantly composed of a single FCC phase, exhibiting a uniform contrast. Grain boundaries are clearly visible, and no distinct secondary phases are visible, only isolated features are occasionally observed.

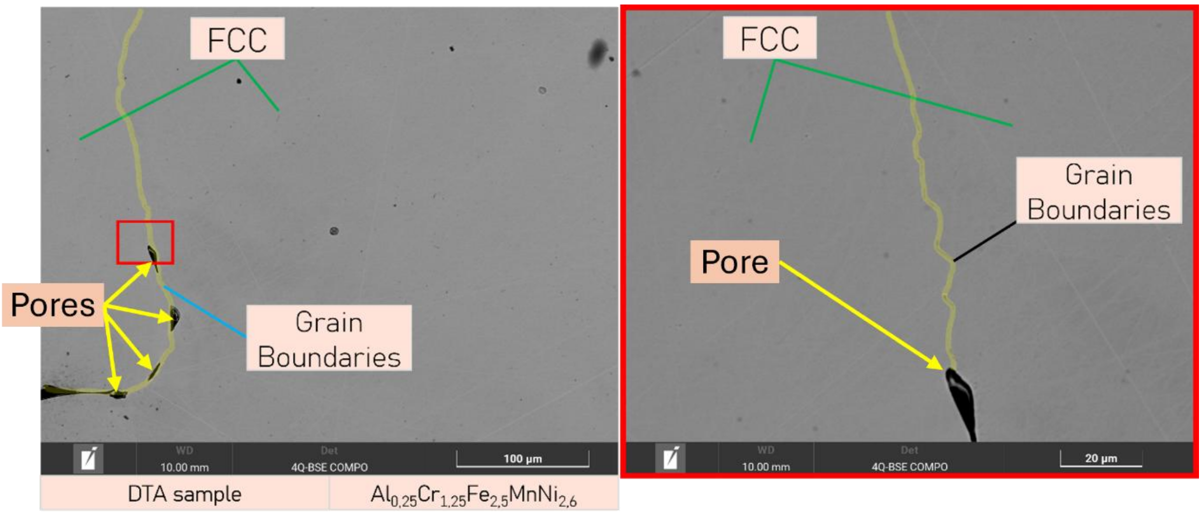

Figure 27: SEM-micrographs of $Al_{0.25}Cr_{1.25}Fe_{2.5}MnNi_{2.6}$ DTA sample

Figure 28 shows an SEM micrograph of the $Al_{0.4}Cr_{1.1}Fe_{2.2}MnNi_{2.3}$ DTA sample. The microstructure consists of an FCC matrix exhibiting a homogeneous contrast over the observed area.

In addition to the FCC matrix, isolated inclusions with distinct contrasts are observed. These features are locally distributed and were identified as Manganese sulfide inclusion (MnS) based on EDX analysis.

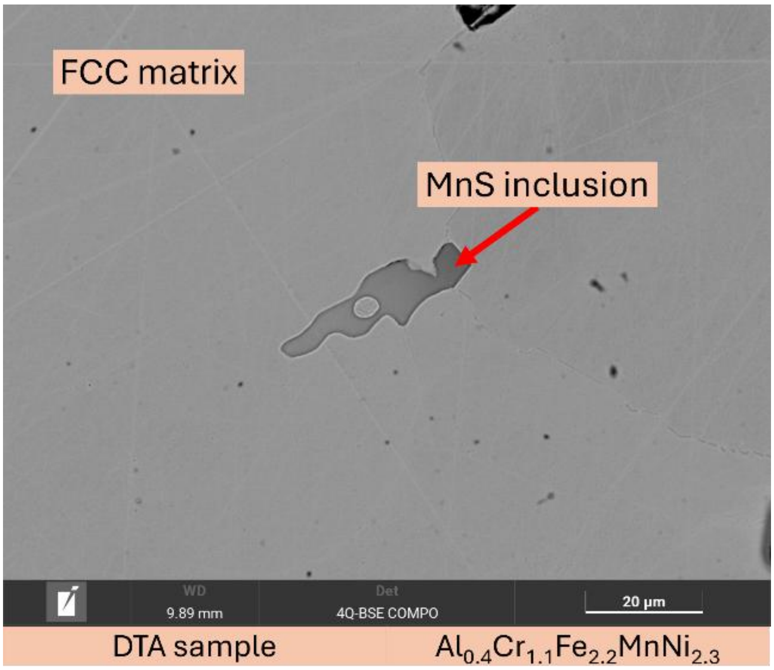

Figure 28: SEM-micrograph of $Al_{0.4}Cr_{1.1}Fe_{2.2}MnNi_{2.3}$ DTA sample

Figure 29 presents an SEM micrograph of the $Al_{0.4}Cr_{1.1}Fe_{2.2}MnNi_{2.3}$ DTA sample with the corresponding EDX elemental maps for Al, Cr, Fe, Mn, and Ni. The microstructure is composed of an FCC matrix within which distinct contrast regions can be observed which are identified as BCC/B2 phases.

The elemental maps indicate a homogeneous distribution of the elements within the FCC matrix. In the BCC/B2 regions, a clear change in elemental contrast is observed, with Al which is strongly enriched, while Cr and Fe are noticeably depleted relative to the FCC phase. Ni shows moderate enrichment in the BCC/B2 regions. In contrast, Mn exhibits only a very slight increase, showing close concentrations of manganese in both phases.

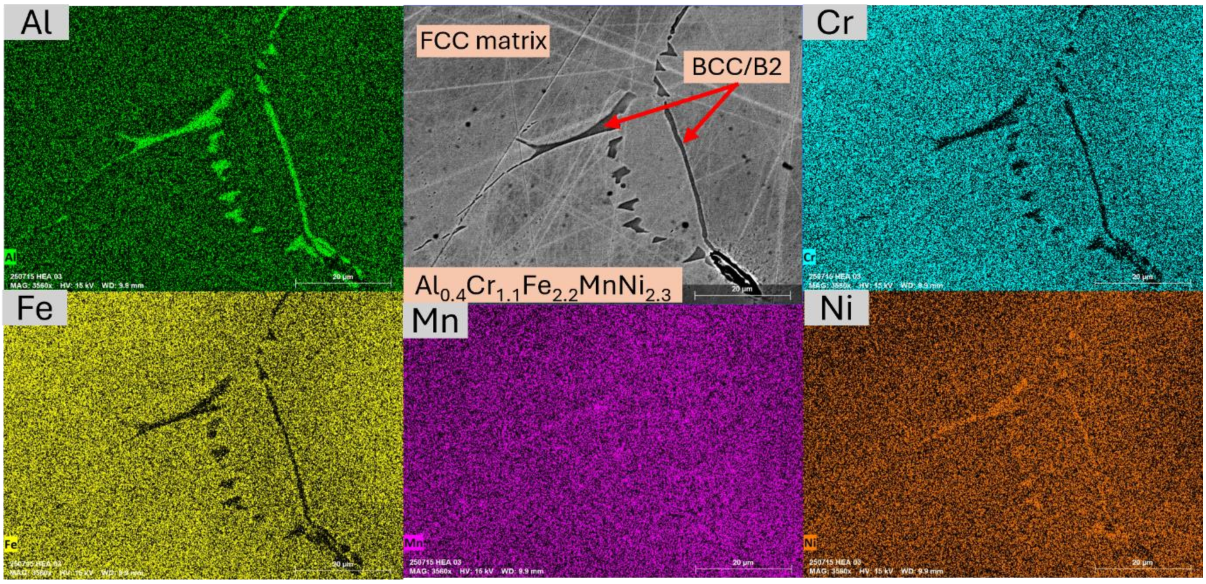

Figure 29: SEM micrograph and EDX elemental mapping of $Al_{0.4}Cr_{1.1}Fe_{2.2}MnNi_{2.3}$ DTA sample

Figure 30 shows a higher-magnification SEM micrograph of the $Al_{0.4}Cr_{1.1}Fe_{2.2}MnNi_{2.3}$ DTA sample, focusing on a BCC/B2 region.

Within the BCC/B2 region, additional fine features are observed and identified as intermetallic phases. These intermetallics are distributed homogenously inside the BCC/B2 phase.

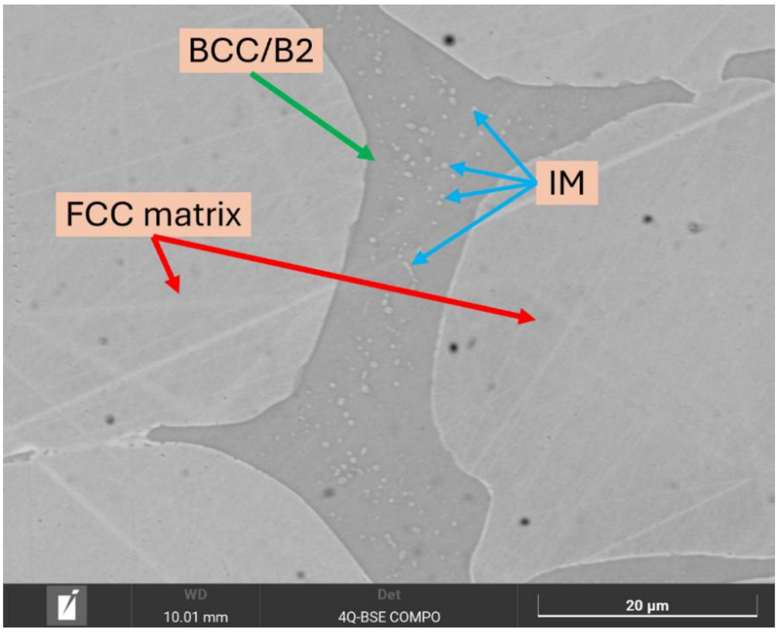

Figure 30: SEM-micrograph of $Al_{0.4}Cr_{1.1}Fe_{2.2}MnNi_{2.3}$ DTA sample

Figure 31 presents an SEM micrograph of the $Al_{0.9}Cr_{1.4}Fe_{2.9}MnNi_3$ DTA sample together with the corresponding EDX elemental maps.

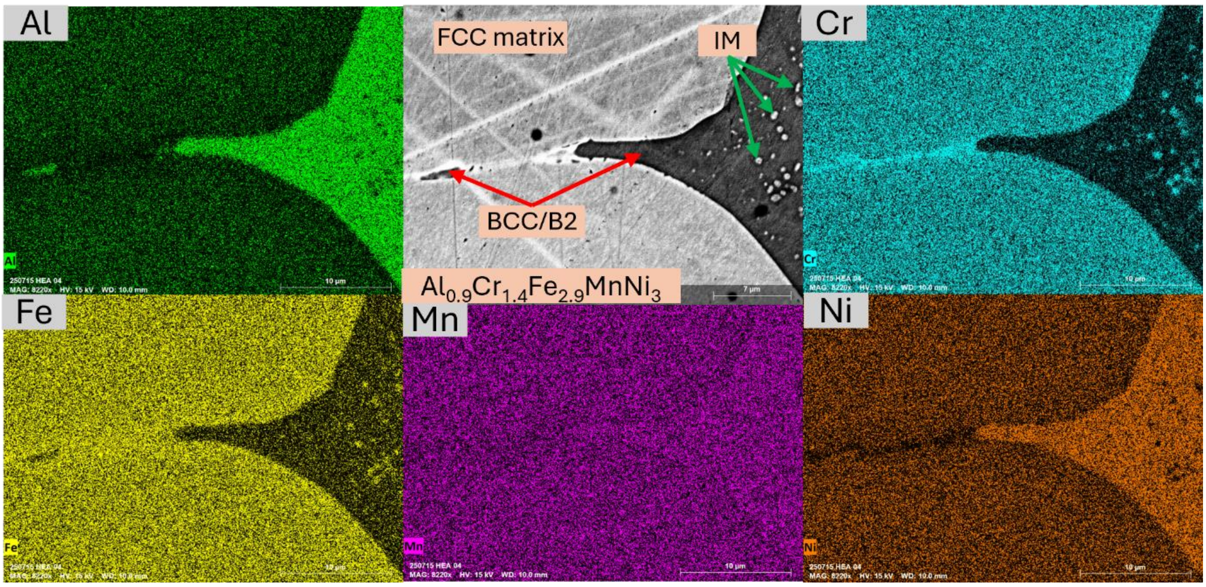

Figure 31: SEM micrograph and EDX elemental mapping of $Al_{0.9}Cr_{1.4}Fe_{2.9}MnNi_3$ DTA sample

The FCC matrix exhibits a homogeneous distribution of all investigated elements over the observed area. In contrast, the BCC/B2 regions show changes in elemental contrast, characterized by a strong enrichment in Al, a moderate increase in Mn and Ni contents, and a depletion in Cr and Fe. The intermetallic phases exhibit a different elemental distribution, with reduced Al and Ni contents, increased Cr and Fe, and Mn levels comparable to those observed in the BCC/B2 regions.

3.3. Process Maps

This section presents the process maps established for the investigated alloy compositions based on laser powder bed fusion experiments. The process map from single track experiments on $CrFe_{2.1}MnNi_2$ alloy are shown, together with optical microscopy images illustrating typical processing-related defects.

Process maps from cubic samples are reported for the $CrFe_{2.1}MnNi_2$ and $Al_{0.25}Cr_{1.25}Fe_{2.5}MnNi_{2.6}$ alloys LPBF printing. For each set of 20 1x1x1cm cubic samples, top view images of the printed samples are presented.

3.3.1. Single Tracks

Figure 32 presents the single track process map established for the $CrFe_{2.1}MnNi_2$ alloy as a function of laser power and scan speed. The map highlights the set of 20 parameter combinations selected for cubic sample printing, as well as regions associated with the occurrence of typical processing related defects.

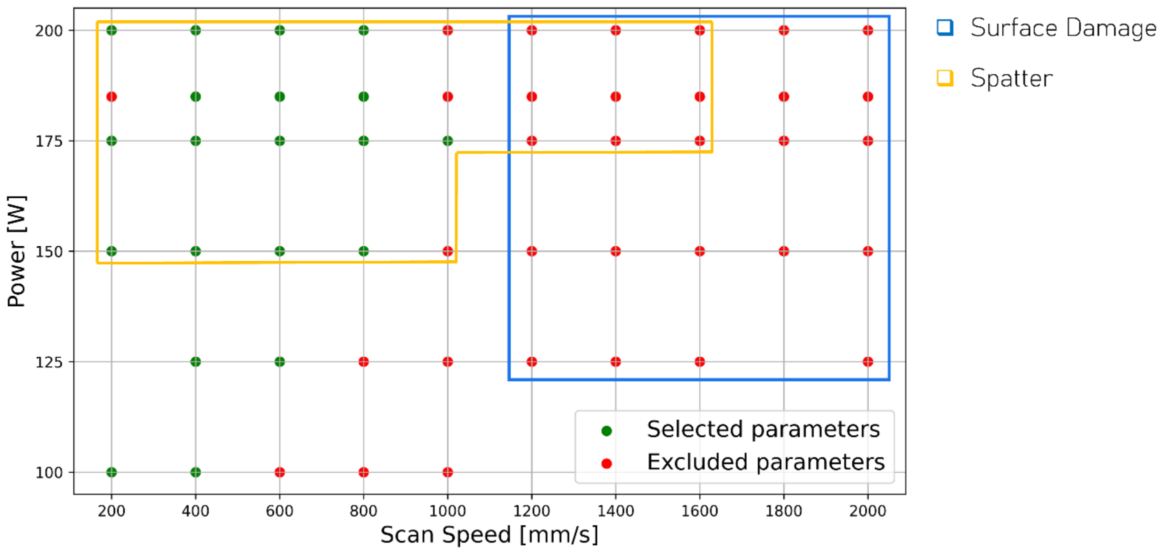

Figure 32: Single track experiment process map of $CrFe_{2.1}MnNi_2$ with selected parameters for cubic sample printing and regions associated with typical defects

Two main defect prone regions are identified on the map, corresponding to surface damage and spatter formation. Representative optical microscopy images of these defects are shown in Figure 33.a and 33.c. Surface damage is characterized by local substrate degradation around the track, while spatter is observed as ejected and resolidified material surrounding the track.

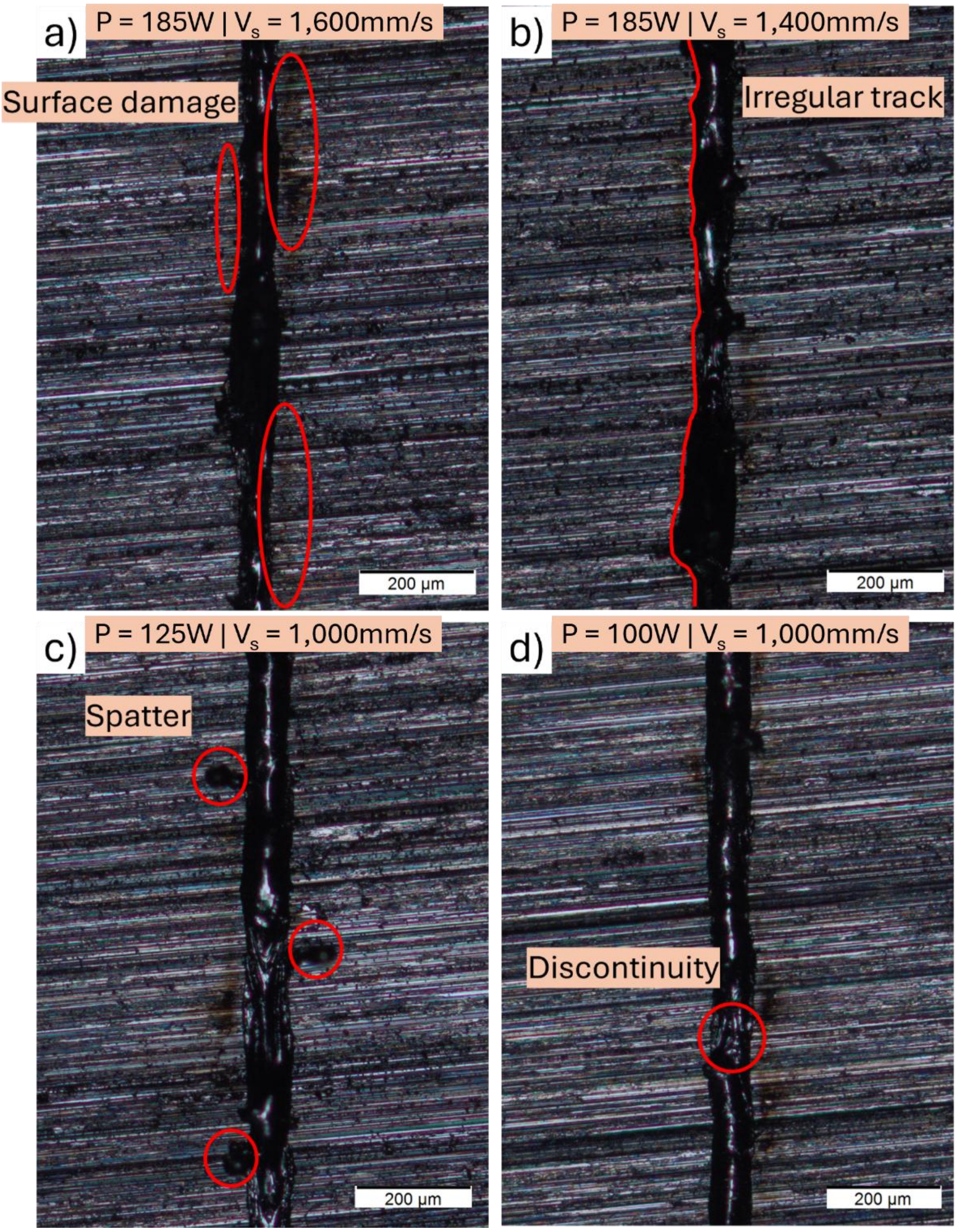

Figure 33: OM-micrographs of $CrFe_{2.1}MnNi_2$ single tracks with (a) surface damage, (b) irregular, (c) spatter, and (d) discontinuity defects.

Other defects, such as irregular track morphology and track discontinuity, are also observed on some samples, as illustrated in Figure 33.b and 33.d. However, these defects are not associated with specific regions of laser power and scan speed in the investigated parameter combinations of laser power and scan speed.

3.3.2. Cubic Samples

3.3.2.1. CrFe$_{2.1}$MnNi$_2$

Figure 34 presents the process map obtained from the fabrication of 1 cm^3 cubic samples of the CrFe$_{2.1}$MnNi$_2$ alloy as a function of laser power and scan speed. Two parameter sets resulted in interrupted builds, the (P = 100W| V$_s$ = 200mm/s) and (P = 150W| V$_s$ = 200mm/s) combinations. The cause of the interruption being a bad powder supply during the early stages of LPBF printing

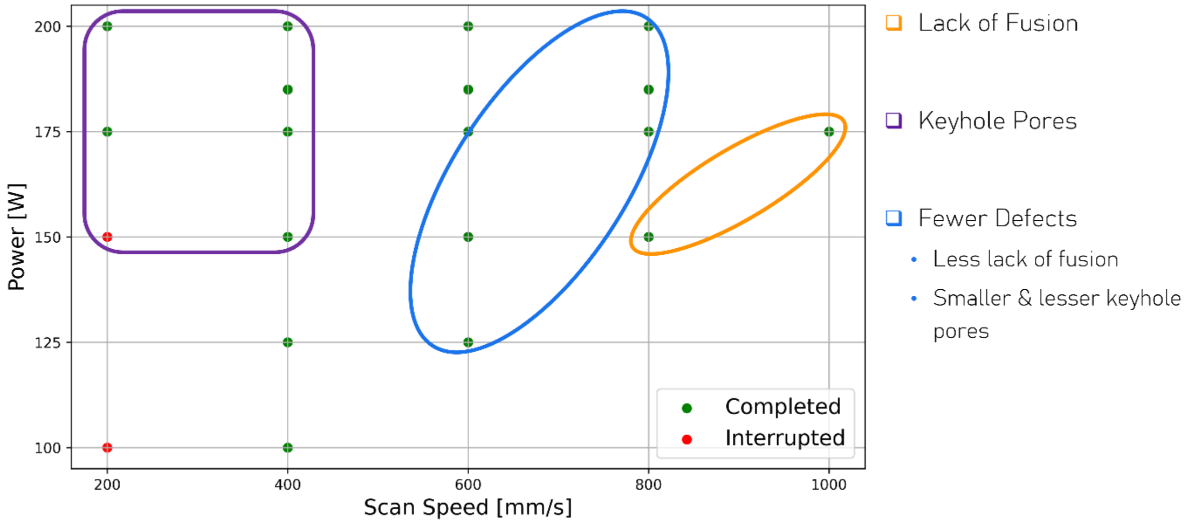

Figure 34: 1cm^3 cubic sample printing process map of CrFe$_{2.1}$MnNi$_2$ with interrupted samples and regions associated with typical defects

Distinct regions associated with typical defects are identified on the map, including areas dominated by lack-of-fusion defects, keyhole porosity, and a region exhibiting fewer observable defects.

Figure 35 shows the top view picture of the 18 cubic samples printed on the substrate, with the direction of the argon gas flow indicated. The interrupted samples (samples 1 and 5) are highlighted in red and samples 9 and 17, highlighted in blue, exhibit visible surface damage at the top layer.

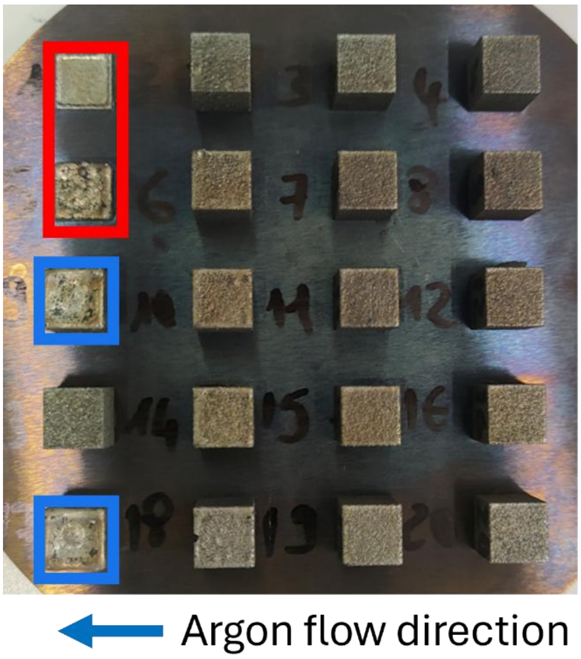

Figure 35: Top view of the 20 cubic $CrFe_{2.1}MnNi_2$ samples printed on the substrate with the direction of the argon gas flow during printing displayed

3.3.2.2. $Al_{0.25}Cr_{1.25}Fe_{2.5}MnNi_{2.6}$

Figure 36 presents the process map obtained from the fabrication of $1cm^3$ cubic samples of $Al_{0.25}Cr_{1.25}Fe_{2.5}MnNi_{2.6}$ alloy as a function of laser power and scan speed. For the investigated

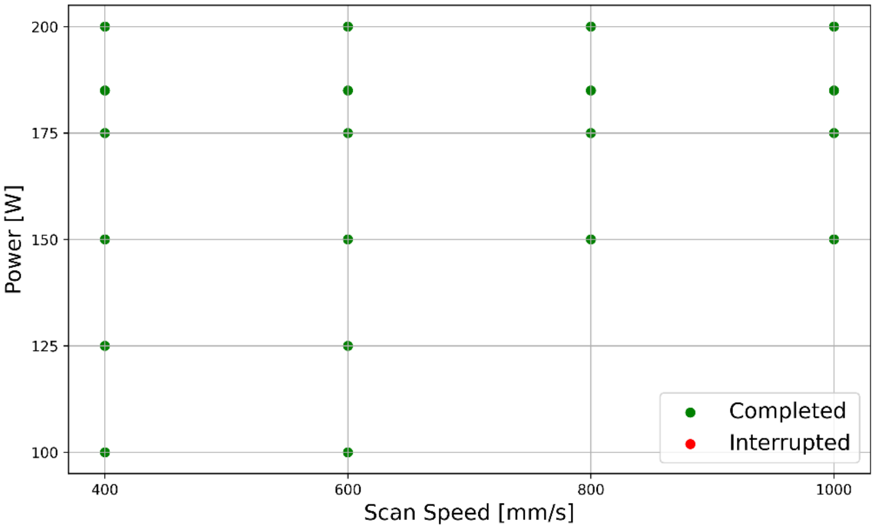

Figure 36: $1cm^3$ cubic sample printing process map of $Al_{0.25}Cr_{1.25}Fe_{2.5}MnNi_{2.6}$

parameter sets, all cubic samples were successfully completed, and no builds were interrupted.

Figure 37 shows the top view picture of the twenty printed cubic samples, with the direction of the argon gas flow indicated. Several cubes, highlighted in red, exhibit a visibly lower quality top layer surface compared to the other samples. These surface features can be seen on every 400mm/s scan speed samples.

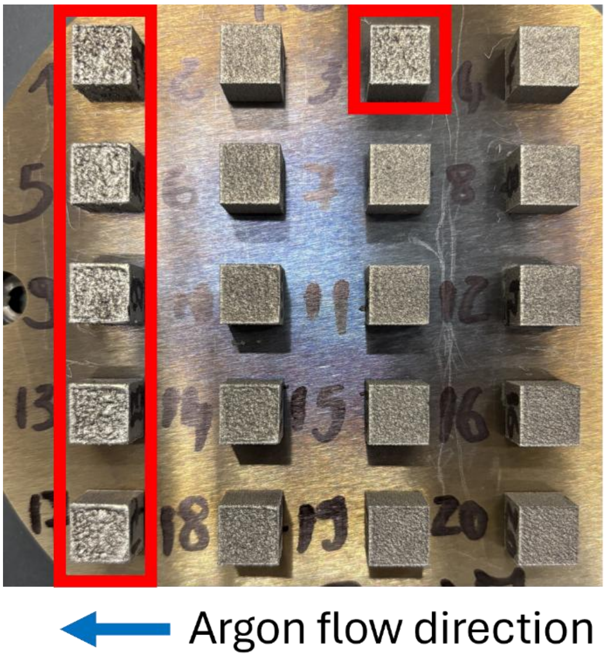

Figure 37: Top view of the 20 cubic $Al_{0.25}Cr_{1.25}Fe_{2.5}MnNi_{2.6}$ samples printed on the substrate with the direction of the argon gas flow during printing displayed

3.4. As-built density measurements

This section presents the as-built density measurements performed on the cubic samples using gas pycnometry. Relative densities are computed with respect to the measured densities of their corresponding powder mixtures. Table 15 summarizes the mean densities of the powders used for the fabrication of the $CrFe_{2.1}MnNi_2$ and $Al_{0.25}Cr_{1.25}Fe_{2.5}MnNi_{2.6}$ cubic samples.

Table 15: Mean density of powder's mixture $CrFe_{2.1}MnNi_2$ and $Al_{0.25}Cr_{1.25}Fe_{2.5}MnNi_{2.6}$

Powder composition	**Mean density [g/cm^3]**

$CrFe_{2.1}MnNi_2$	7.963
$Al_{0.25}Cr_{1.25}Fe_{2.5}MnNi_{2.6}$	7.780

3.4.1. $CrFe_{2.1}MnNi_2$

Figure 38 shows the relative density heat map of the $CrFe_{2.1}MnNi_2$ cubic samples as a function of laser power and scan speed.

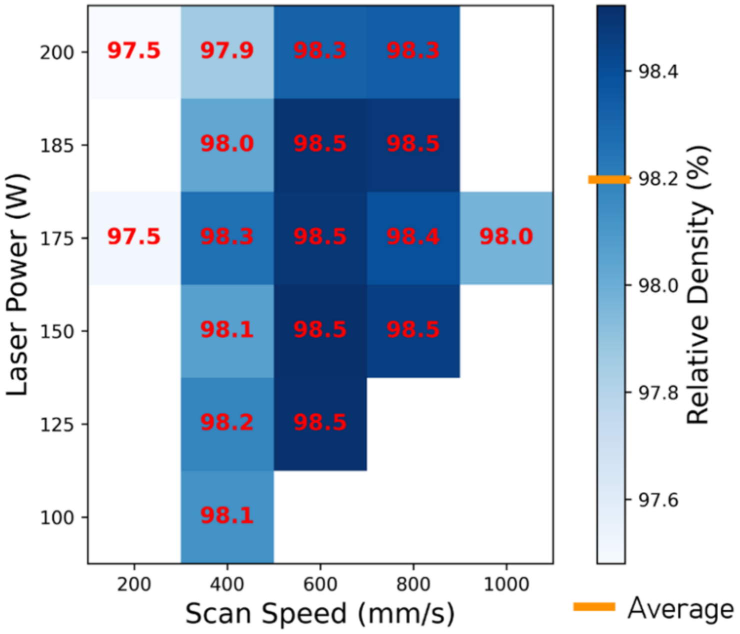

Figure 38: Relative density heat map of $CrFe_{2.1}MnNi_2$ cubic samples wrt. Laser power (W) and Scan speed (mm/s)

Lower relative densities are systematically observed for samples produced at a scan speed of 200mm/s. The highest relative densities are obtained for parameter combinations for laser power ranges from 125 to 185W and scan speed ranges from 600 to 800mm/s. The overall average relative density was also measured at around 98.2%.

3.4.2. $Al_{0.25}Cr_{1.25}Fe_{2.5}$MnNi2.6

Figure 39 presents the relative density heat map of the $Al_{0.25}Cr_{1.25}Fe_{2.5}MnNi_{2.6}$ cubic samples as a function of laser power and scan speed.

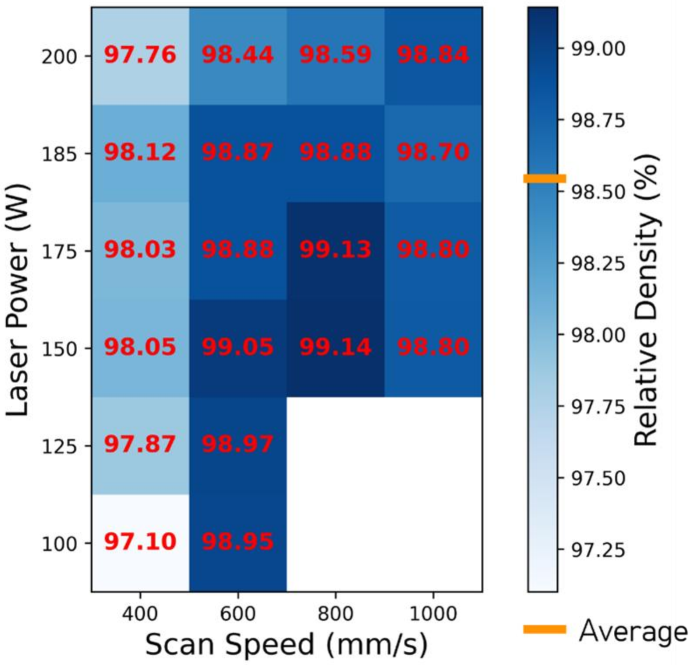

Figure 39: Relative density heat map of $Al_{0.25}Cr_{1.25}Fe_{2.5}MnNi_{2.6}$ cubic samples wrt. Laser power (W) and Scan speed (mm/s)

The highest relative densities are observed for laser power in the range of 150-175W combined with scan speeds between 600 and 800mm/s. The lower relative densities are measured for samples produced at the lowest scan speed of 400mm/s. The average relative density over the investigated parameter sets is approximately 98.55%.

3.5. As-built top layer profilometry

This section presents the characterization of the as-built top layer surfaces of selected cubic samples using three-dimensional optical surface profilometry. The analysis focuses on the surface morphology and height distributions obtained under different processing laser power and scan speed for the $CrFe_{2.1}MnNi_2$ and $Al_{0.25}Cr_{1.25}Fe_{2.5}MnNi_{2.6}$ alloys.

3.5.1. Surface morphology

Figure 40 shows representative three-dimensional surface profiles and corresponding height maps of the as-built top layers for both alloy compositions. For the $Al_{0.25}Cr_{1.25}Fe_{2.5}MnNi_{2.6}$ samples, case (a) exhibits a degraded surface morphology characterized by pronounced valleys and height variations, whereas case (b) displays a more homogeneous surface with reduced height fluctuations.

A similar contrast is observed for the $CrFe_{2.1}MnNi_2$ samples. Case (c) shows a highly irregular surface with deep valleys, including regions that could not be fully reconstructed due to excessive depth variations, while case (d) presents a smoother and more uniform top layer.

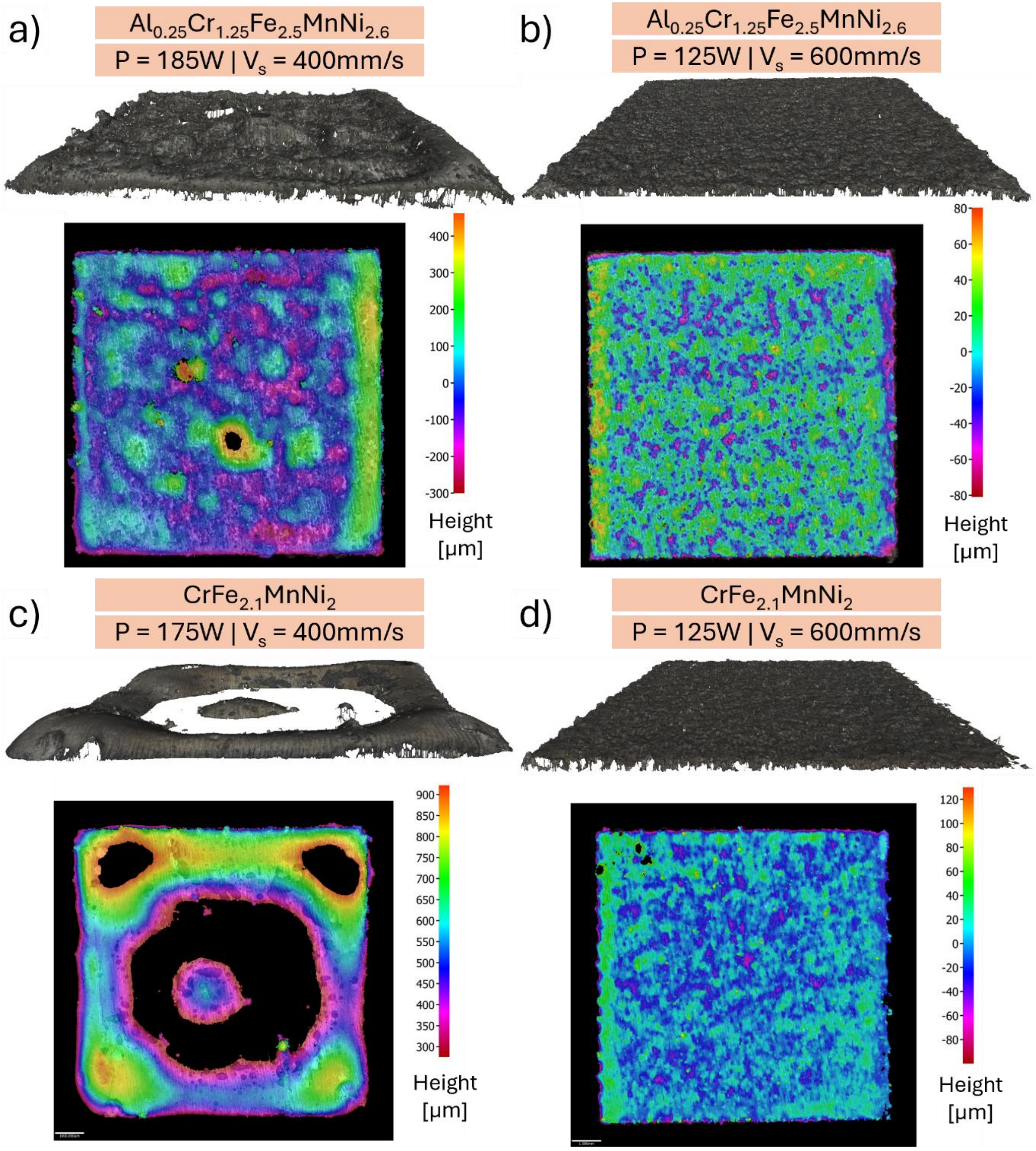

Figure 40: Top layer surface roughness with inclined views and top view height maps

The corresponding top layer height distribution histograms are presented in Figure 41 for each surface profile. Samples exhibiting higher surface quality show a near-normal height distribution centered around zero, indicating a more uniform surface height.

In contrast, samples with degraded surface morphology display broader and asymmetric distributions, with extended plateaus and tails aways from zero height. These distributions reflect the presence of pronounced peaks and valleys across the top layer surface.

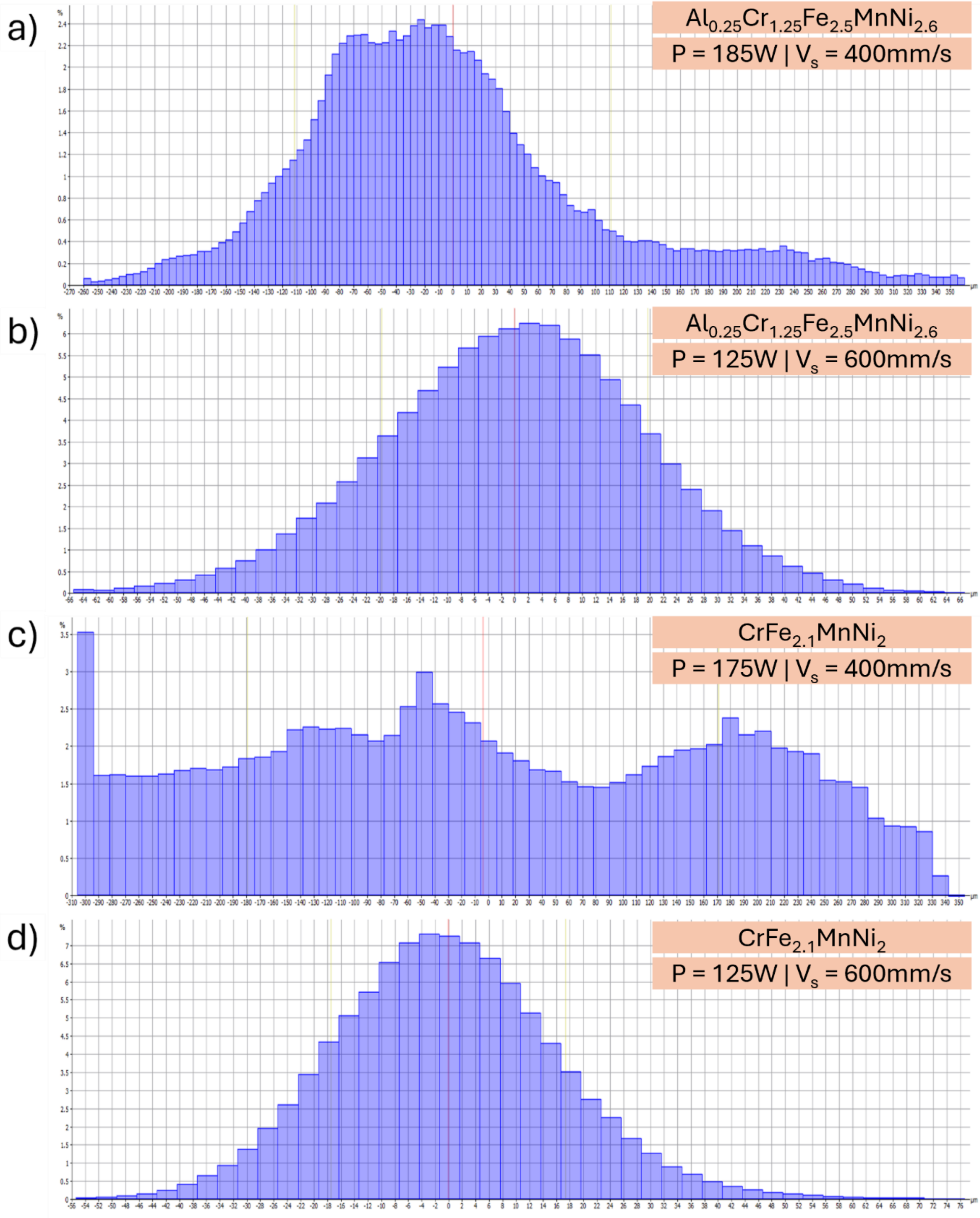

Figure 41: Top layer height distribution histograms

3.5.2. Average and maximum heights

Figures 42 and 43 present the heat maps of the average and maximum top layer heights, respectively, as a function of laser power and scan speed for both alloys. For the $CrFe_{2.1}MnNi_2$ samples, higher average and maximum heights are observed at lower scan speeds, particularly when combined with higher laser powers.

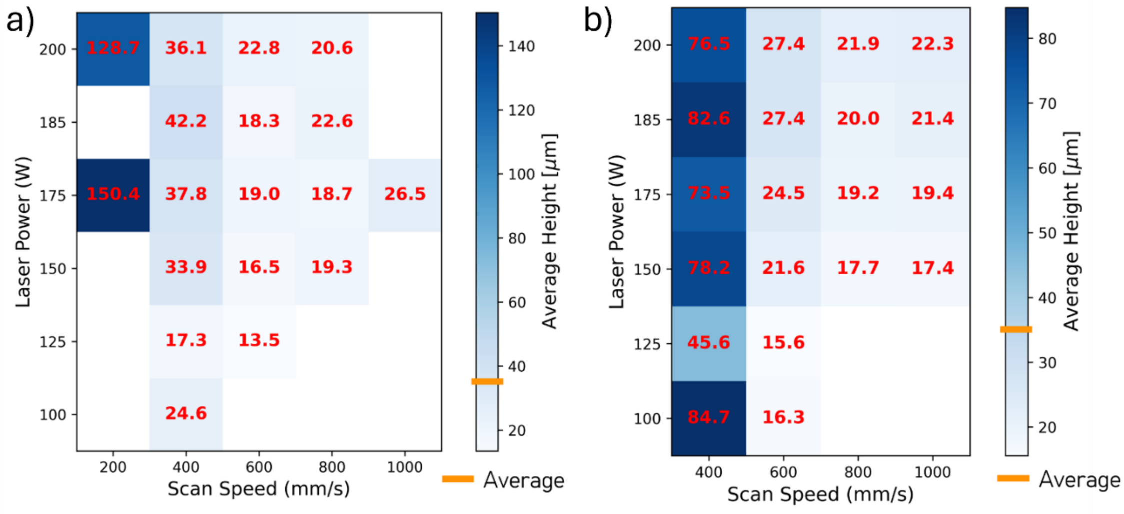

Figure 42: Top layer average height heat map of (a) $CrFe_{2.1}MnNi_2$ and (b) $Al_{0.25}Cr_{1.25}Fe_{2.5}MnNi_{2.6}$ cubic samples wrt. Laser power and scan speed

Similar observations can be made for the $Al_{0.25}Cr_{1.25}Fe_{2.5}MnNi_{2.6}$ cubic samples, for which the largest average and maximum height values occur at the lowest scan speeds. An increase in laser power is associated with higher surface height values for these samples across the different parameter sets

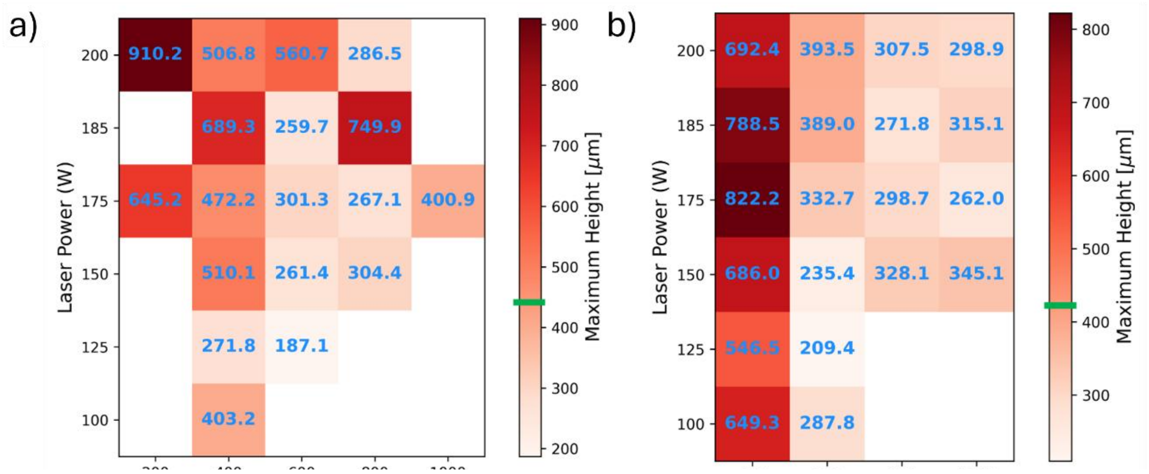

Figure 43: Top layer maximum height heat map of (a) $CrFe_{2.1}MnNi_2$ and (b) $Al_{0.25}Cr_{1.25}Fe_{2.5}MnNi_{2.6}$ cubic samples wrt. Laser power and scan speed

3.6. Microstructural characterization

This section presents the microstructural characterization of the as-built cubic samples using optical and electron microscopy techniques. The analysis includes the evaluation of porosity and defect distribution based on optical and SEM micrographs as well as the definition of the microstructural features observed using SEM.

Crystallographic information is further investigated using electron backscatter diffraction (EBSD) to identify the phases present and their spatial distribution. In addition, EDX spectroscopy is employed through elemental mapping and point analysis to analyze elemental partitioning, segregation, and the presence of inclusions.

3.6.1. Optical micrographs

3.6.1.1. Porosity analysis

Figure 44 present the as-built heat maps of the $CrFe_{2.1}MnNi_2$ and $Al_{0.25}Cr_{1.25}Fe_{2.5}MnNi_{2.6}$ cubic samples as a function of laser power and scan speed.

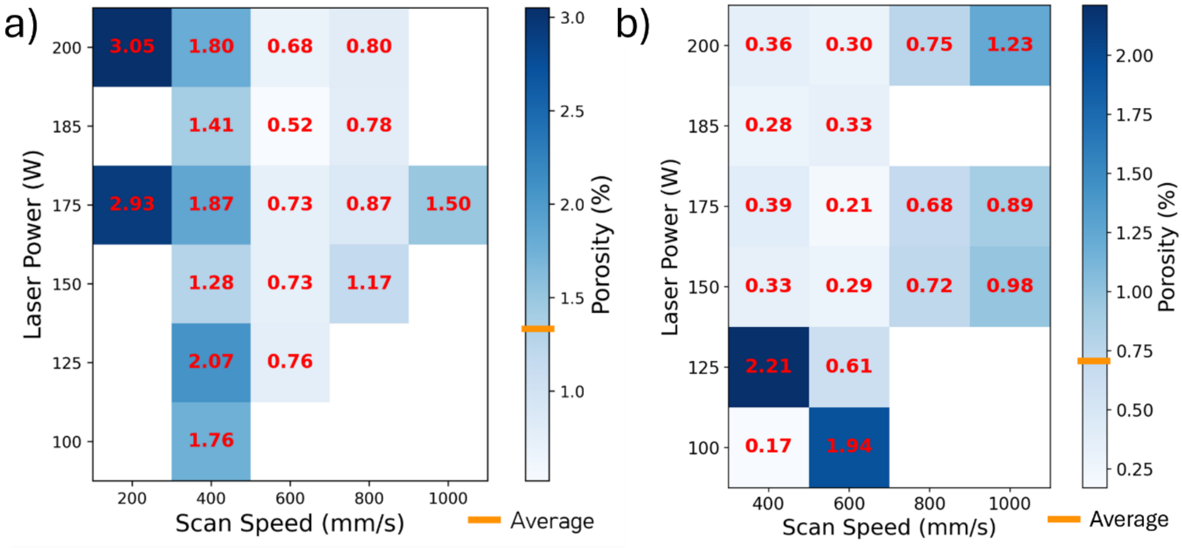

Figure 44: As-built porosity heat map of (a) $CrFe_{2.1}MnNi_2$ and (b) $Al_{0.25}Cr_{1.25}Fe_{2.5}MnNi_{2.6}$ cubic samples wrt. Laser power and scan speed

For the $CrFe_{2.1}MnNi_2$ alloy Figure 44.a, the highest porosity levels are observed at the lowest scan speed of 200mm/s. Samples produced at 400mm/s also exhibit elevated porosity values compared to higher scan speeds. The lowest porosity levels are obtained at a scan speed of 600mm/s, with a further reduction observed as laser power increases. The lowest porosity values are measured for samples produced at laser powers of 185W and 200W.

For the $Al_{0.25}Cr_{1.25}Fe_{2.5}MnNi_{2.6}$ alloy, Figure 44.b, a region of lower porosity is observed for laser powers between 150 to 200W combined with scan speeds of 400 and 600mm/s. An exception is observed for the sample produced at 100W and 200mm/s, which exhibits the lowest porosity achieved.

Representative optical micrographs of $CrFe_{2.1}MnNi_2$ cubic samples with different porosity levels are shown for comparison in Figure 45. Samples with low porosity exhibit a homogeneous distribution of small pores throughout the cross-section, whereas samples with higher porosity display larger pores, particularly concentrated near the sample boundaries. For some high porosity samples, at the top layer, a very low porosity region is observed, extending over a thickness of approximately 0.35 to 1mm.

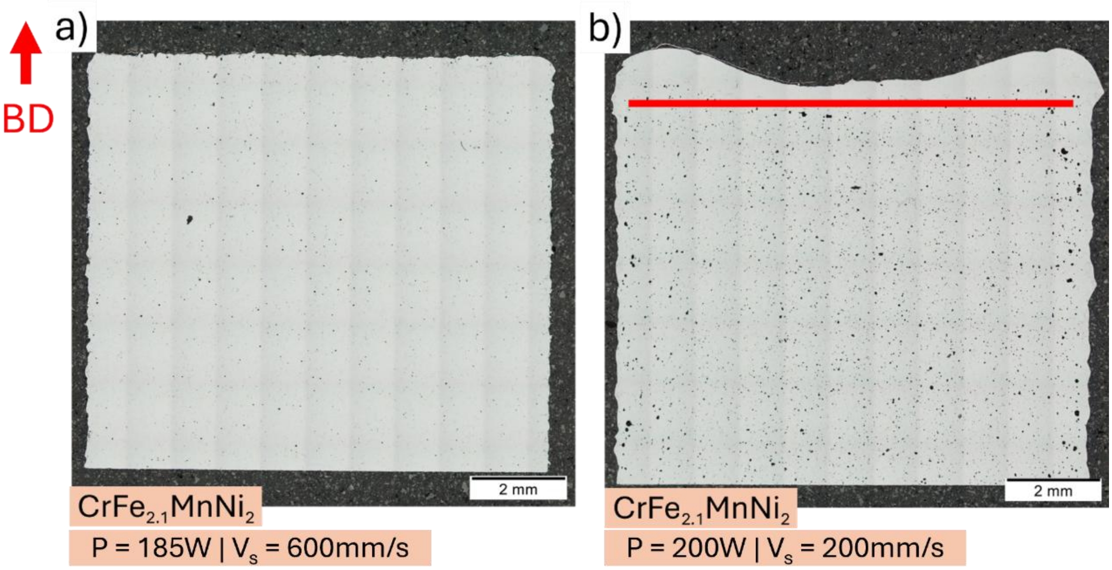

Figure 45: OM-micrographs of $CrFe_{2.1}MnNi_2$ cubic samples cross sections

3.6.2. Crystallographic structure (EBSD)

3.6.2.1. Phase distribution

Figure 46 and Figure 47 present the EBSD phase maps and corresponding pattern quality maps obtained for representative $CrFe_{2.1}MnNi_2$ and $Al_{0.25}Cr_{1.25}Fe_{2.5}MnNi_{2.6}$ cubic samples, respectively. For both compositions, the EBSD phase maps indicate a fully FCC crystallographic structure over the investigated regions.

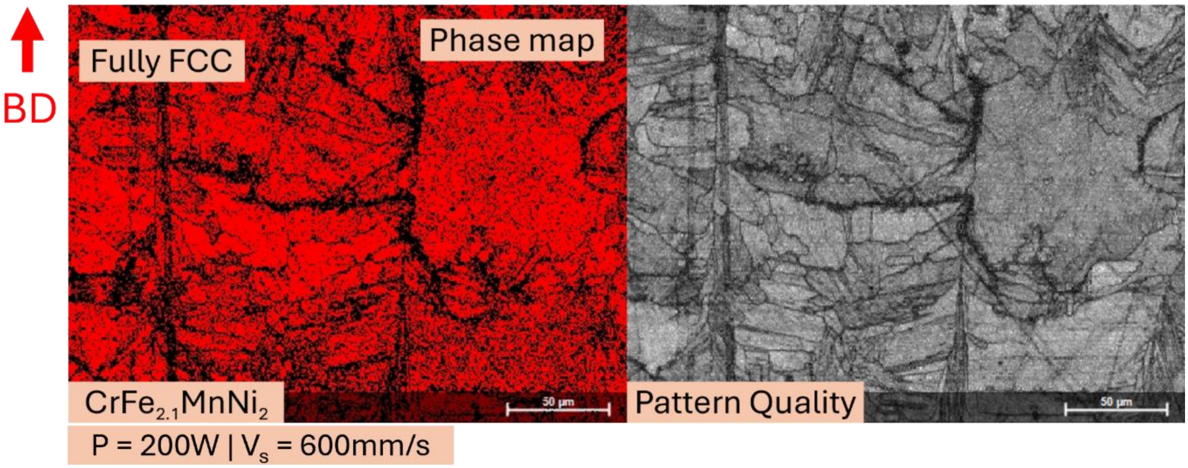

Figure 46: EBSD phase map and corresponding pattern quality

The associated pattern quality maps show spatial variations in indexing quality, with darker regions corresponding to lower pattern quality. Despite these local variations, no secondary phases are detected within the mapped areas.

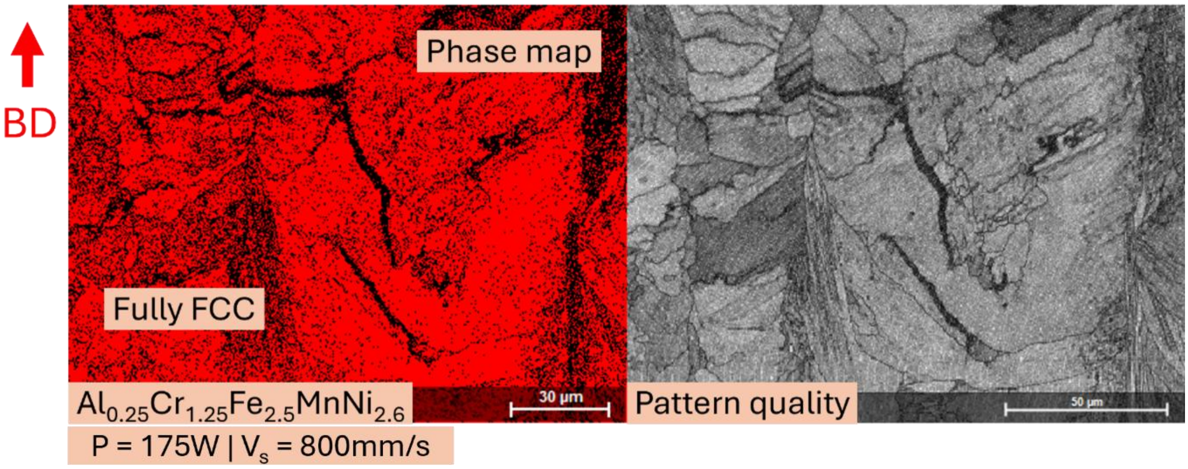

Figure 47: EBSD phase map and corresponding pattern quality

The FCC phase is homogeneously distributed throughout the analyzed cross-sections for both alloys.

3.6.2.2. **Grain morphology**

Figure 48 and Figure 49 show EBSD grain boundary maps and corresponding pattern quality images for the same regions. The microstructure is characterized by elongated, columnar grains predominantly oriented along the build direction.

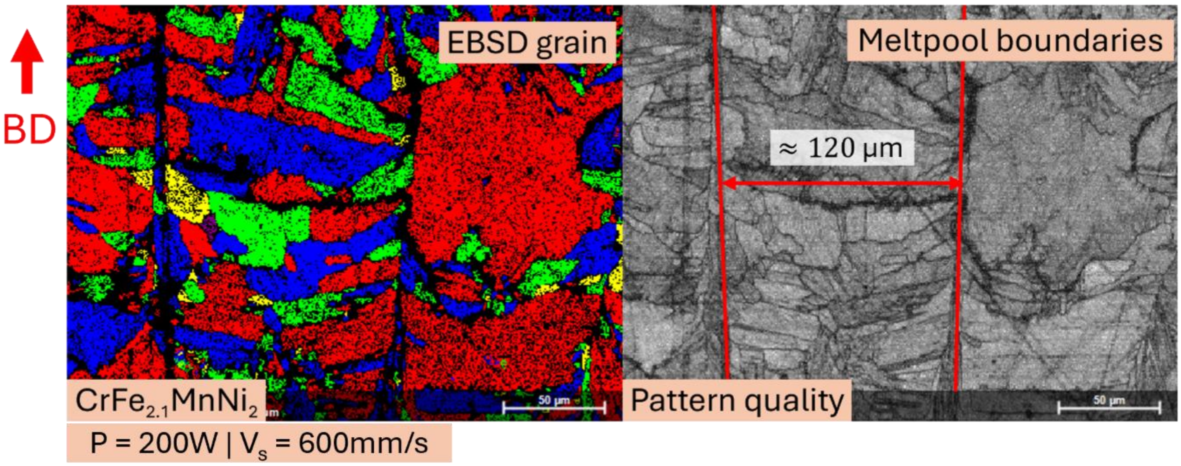

Figure 48: EBSD grain boundary map and corresponding pattern quality

The grain morphology is spatially correlated with the melt pool geometry, as melt pool boundaries are clearly visible in the pattern quality images and delineate regions of grain structure. The characteristics melt pool width is measured to be on the order of approximately 120µm for $CrFe_{2.1}MnNi_2$ and around 100µm for $Al_{0.25}Cr_{1.25}Fe_{2.5}MnNi_{2.6}$.

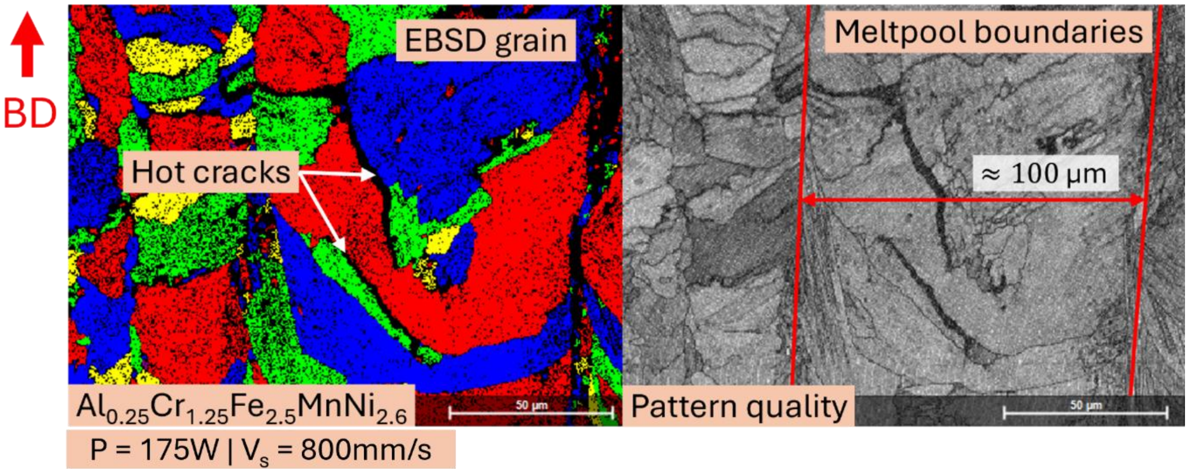

Figure 49: EBSD grain boundary map and corresponding pattern quality

3.6.3. **SEM micrographs**

3.6.3.1. **Cracks**

Figure 50 and Figure 51 present SEM micrographs illustrating cracking features observed in the as-built cubic samples. Cracks are predominantly located along grain boundaries, corresponding to intergranular cracking. These cracks are observed throughout the whole build and are present in all investigated samples.

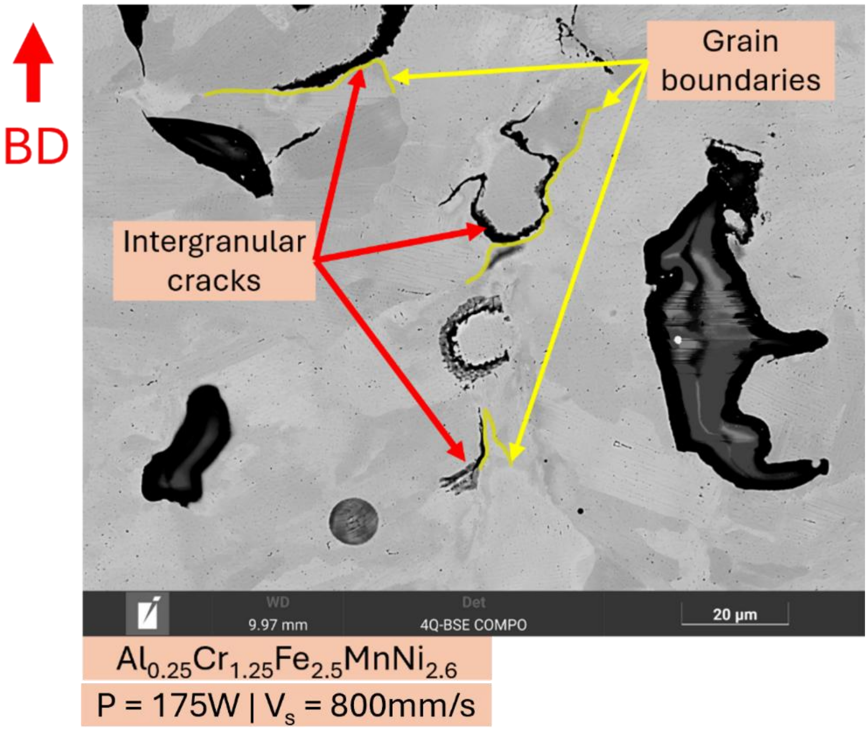

Figure 50: SEM-micrograph of $Al_{0.25}Cr_{1.25}Fe_{2.5}MnNi_{2.6}$ cubic sample

A higher density of cracks is observed at the top layer of the samples, as shown in Figure 51. These cracks often propagate across the microstructure and are frequently located near powder particles.

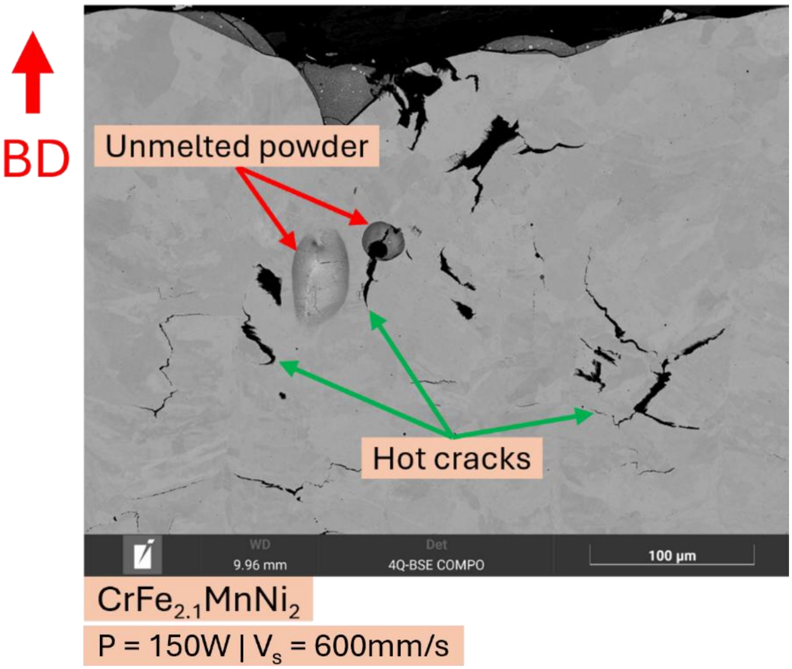

Figure 51: SEM-micrograph of $CrFe_{2.1}MnNi_2$ cubic sample

3.6.3.2. **Unmelted powders**

Figure 52 and Figure 53 show SEM micrographs highlighting the presence of unmelted powders and partially melted powder particles within the microstructure.

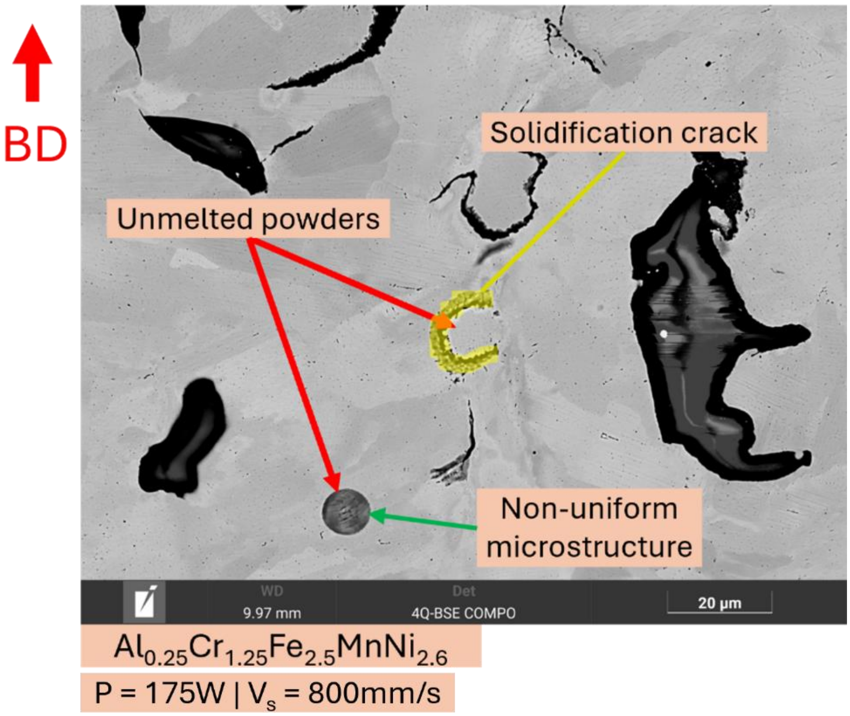

Figure 52: SEM-micrograph of $Al_{0.25}Cr_{1.25}Fe_{2.5}MnNi_{2.6}$ cubic sample

Two main morphologies are observed. Fully unmelted powder particles are characterized by a sharp and well-defined interface with the surrounding FCC matrix, indicating minimal interaction with the melt pool.

In contrast, partially melted powder particles exhibit a more diffuse interface with the surrounding microstructure. These regions are often associated with local microstructural heterogeneity and are frequently accompanied by solidification cracks at their boundaries.

A higher magnification view of a partially melted powder particle (Figure 53) reveals heterogeneous diffusion at the interface between the particle and the FCC matrix, with a visible transition zone separating the two regions.

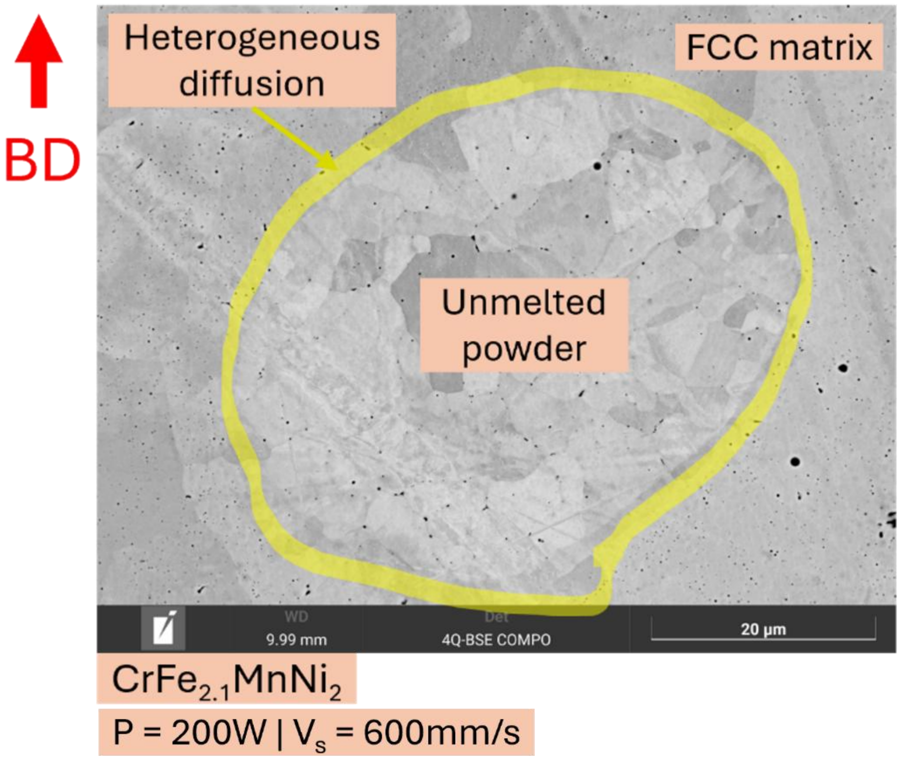

Figure 53: SEM-micrograph of $CrFe_{2.1}MnNi_2$ cubic sample at the top layer

3.6.3.3. **Pores**

Figure 54 and Figure 55 present SEM micrographs illustrating the different types of pores observed in the as-built cubic samples under various laser power and scan speed combinations.

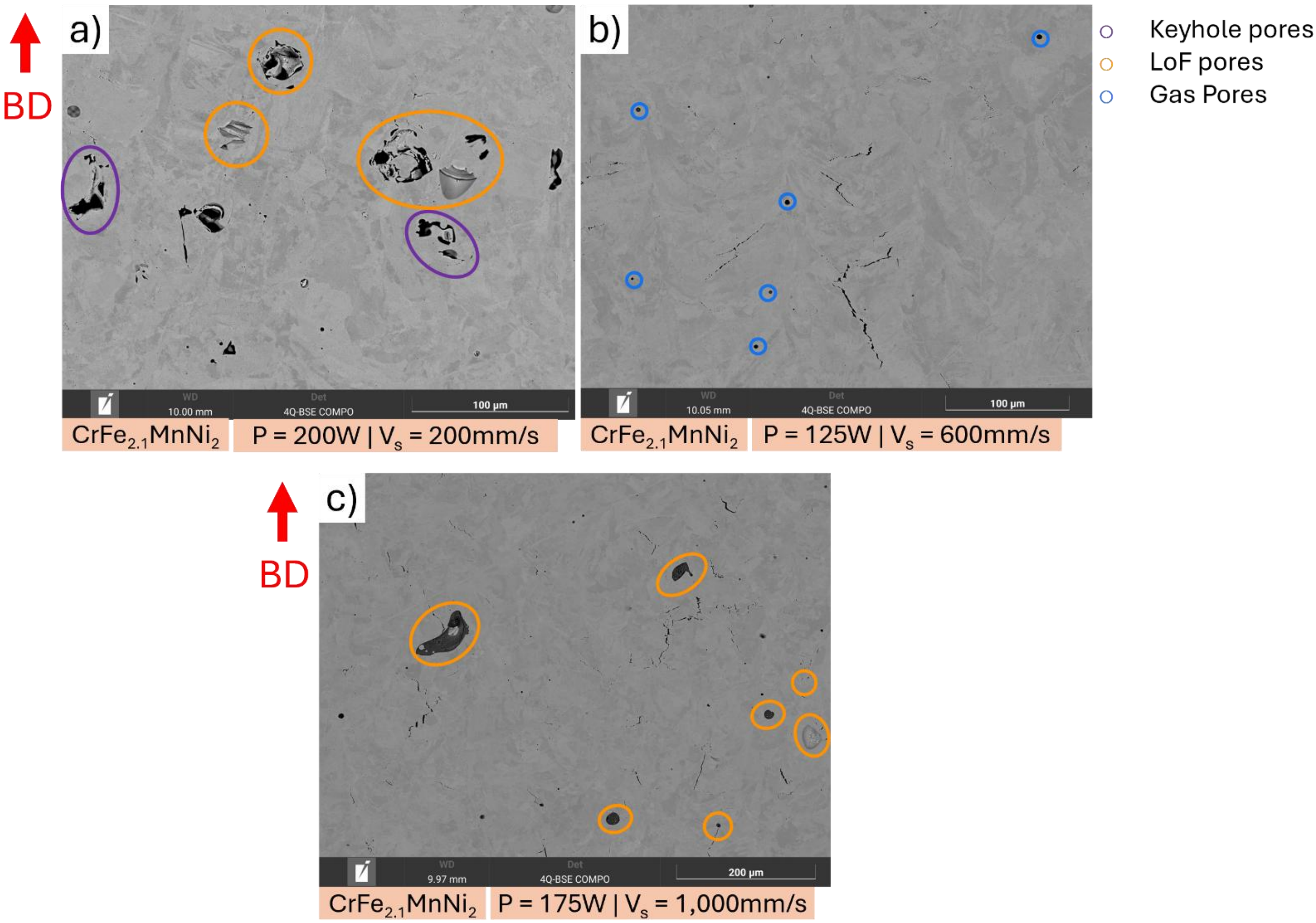

Figure 54: SEM-micrographs of CrFe$_{2.1}$MnNi$_2$ cubic samples

At high laser power combined with low scan speed, pores with morphology characteristics of keyhole porosity are observed and these pores are distributed throughout the build, as in Figure 54.a.

For intermediate scan speeds ranging from 600 to 800mm/s and medium to high laser powers in the range of 125-200W, as in Figure 54.b, the samples exhibit a reduced number of defects. In these conditions, gas pores are still present, while keyhole pores are no longer observed and only a limited number of lack-of-fusion pores can be identified.

Lack-of-fusion pores are predominantly observed at high scan speed, as shown in Figure 54.c. However, although their occurrence increases at high scan speeds, lack-of-fusion pores can be observed across every samples.

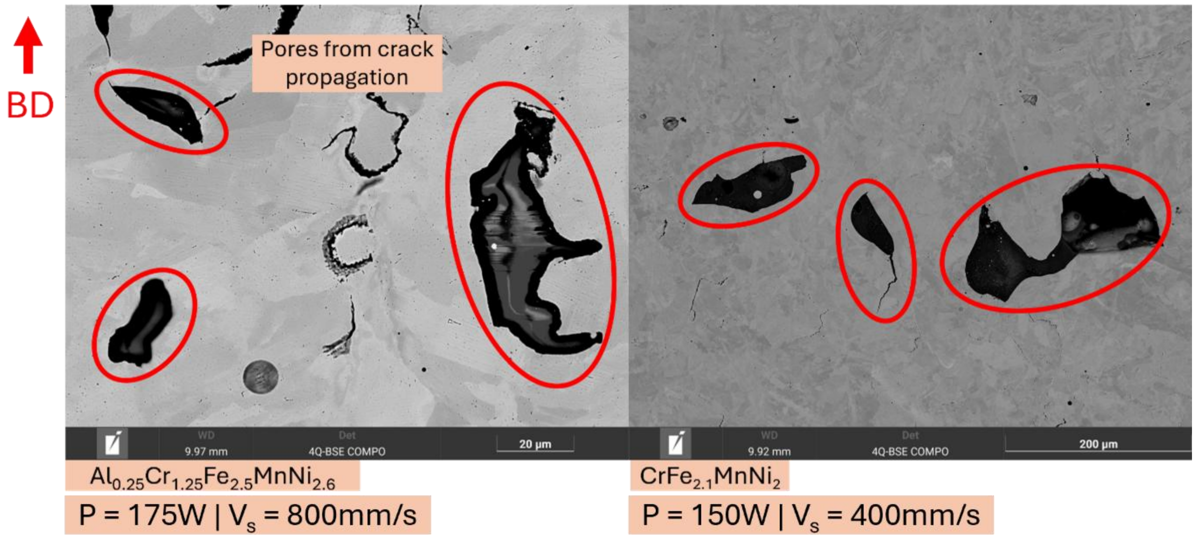

Figure 55: SEM-micrographs of (a) $Al_{0.25}Cr_{1.25}Fe_{2.5}MnNi_{2.6}$ cubic sample, and (b) $CrFe_{2.1}MnNi_2$ cubic sample

Pores associated with crack propagation are observed, as shown in Figure 55. These pores are typically located along grain boundaries or near unmelted powder particles and are distributed throughout the build.

3.6.4. EDX and elemental mappings

Figure 56 and Figure 57 present SEM micrographs and corresponding EDX elemental mappings of a $CrFe_{2.1}MnNi_2$ cubic sample, highlighting the presence of inclusions within the FCC matrix. The elemental maps reveal the presence of Si-rich inclusions, which are commonly observed on $CrFe_{2.1}MnNi_2$ samples.

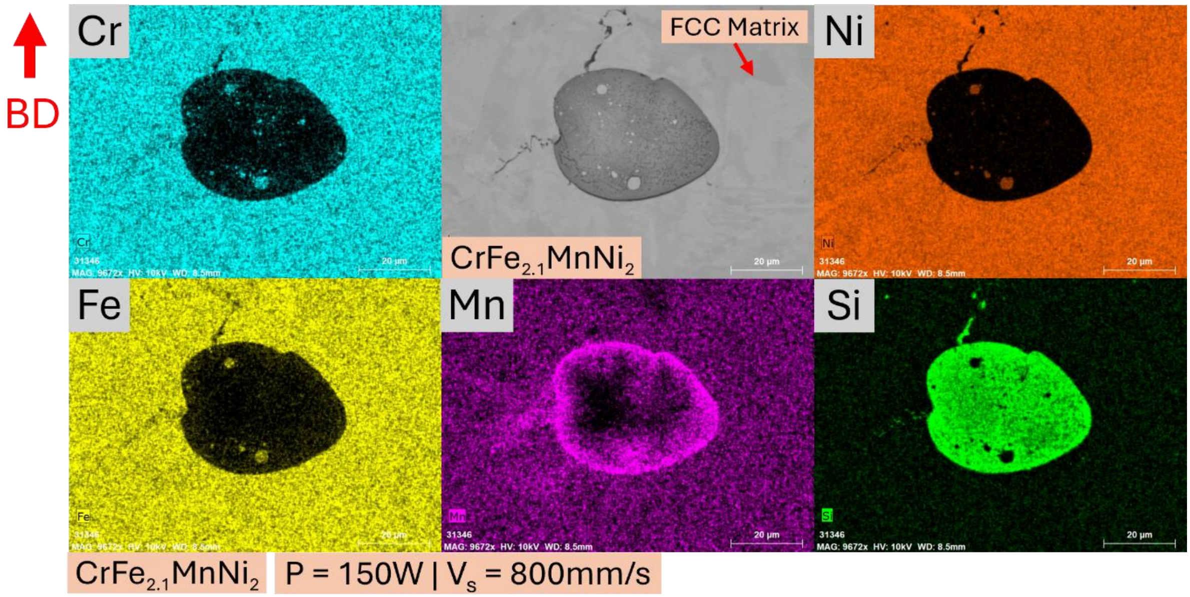

Figure 56: SEM-micrograph of $CrFe_{2.1}MnNi_2$ cubic sample with elemental mapping for Cr, Ni, Fe, Mn, and Si elements

The Si-rich inclusions are surrounded by a distinct Mn-enriched layer located at the interface between the inclusion and the surrounding FCC matrix. This interfacial region is clearly visible in the Mn elemental maps, forming a continuous shell around the inclusion.

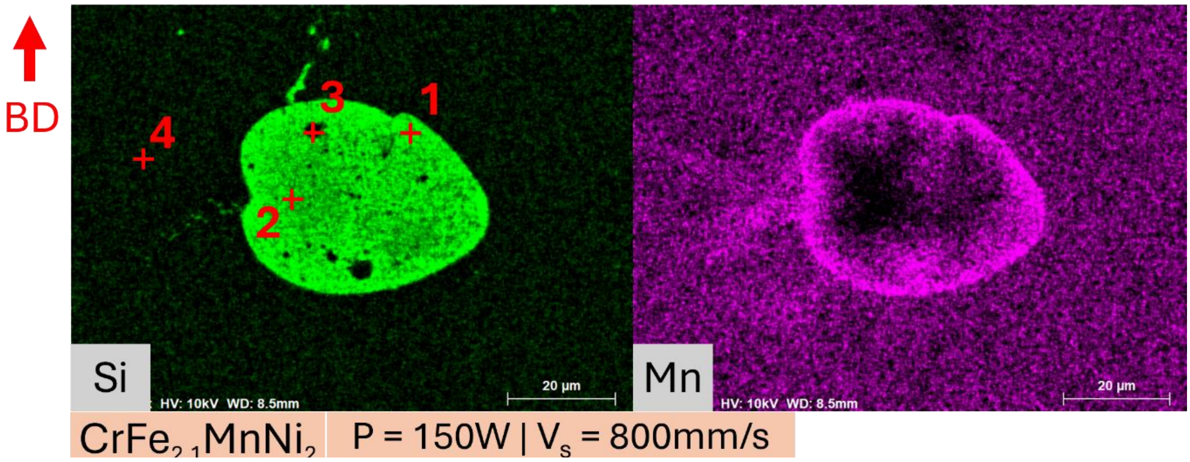

Figure 57: Elemental mapping of $CrFe_{2.1}MnNi_2$ cubic sample for Si, and Mn elements

Semi-quantitative EDX point analyses performed at selected locations (Table 16) provide the chemical composition of these regions. Point 2, located within the Si-rich inclusion, exhibits a high oxygen content, indicating the formation of silicon oxides within the matrix. Point 1, corresponding to the interfacial region, shows an increased manganese content compared to the surrounding matrix (point 4).

Regions located inside the Si-rich inclusion, such as point 3, exhibit chemical compositions nearly similar to that of the FCC matrix (point 4), suggesting the presence of locally embedded matrix-like material within the oxide inclusion.

Table 16: Chemical composition of EDX point analysis (Figure 57) for CrFe$_{2.1}$MnNi$_2$ $_1$MnNi$_2$ cubic sample (P = 150W | V$_s$ = 800mm/s)

Spectrum	Cr	Fe	Mn	Ni	Si	O
1 – wt.%	4.78	1.17	44.9	0.53	13.9	30.4
2 – wt.%	1.94	-	21.3	-	12.8	35.7
3 – wt.%	16.0	29.9	18.1	17.0	1.0	-
4 – wt.%	16.1	36.9	14.2	26.0	0.85	-

Figure 58 and Figure 59 present SEM micrographs and corresponding EDX elemental mappings of an Al$_{0.25}$Cr$_{1.25}$Fe$_{2.5}$MnNi$_{2.6}$ cubic sample, highlighting the presence of oxide inclusions within the FCC matrix. The elemental maps reveal inclusions enriched in aluminum and oxygen, indicating the formation of aluminum oxide phases in the as-built material.

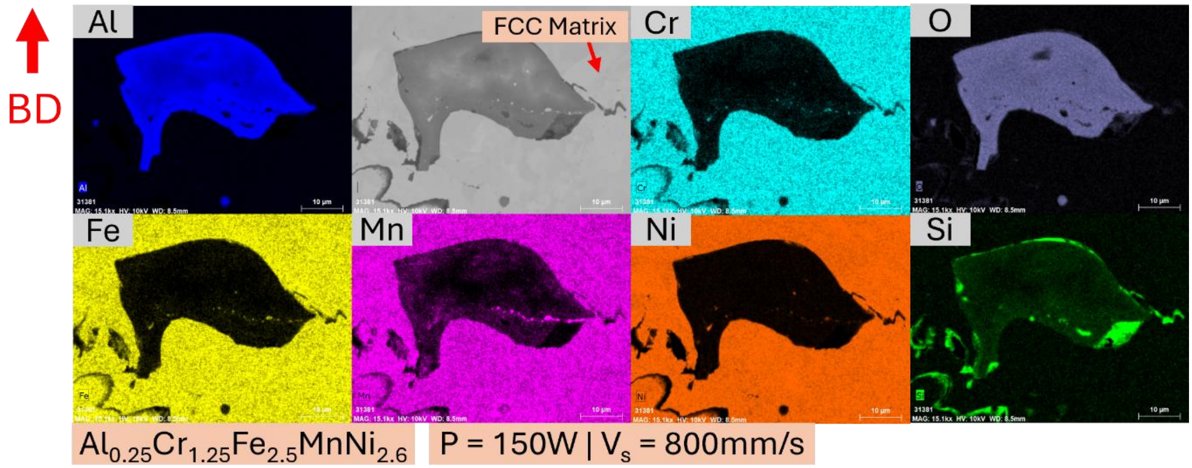

Figure 58: SEM-micrograph of Al$_{0.25}$Cr$_{1.25}$Fe$_{2.5}$MnNi$_{2.6}$ cubic sample with elemental mapping of Al, Cr, O, Fe, Mn, Ni, and Si elements

These Al-rich oxide inclusions are surrounded by an interfacial region enriched in silicon, which forms a distinct layer between the oxide inclusion and the FCC matrix. This interfacial Si-rich layer is clearly visible in the Si elemental maps and delineates the inclusion from the matrix.

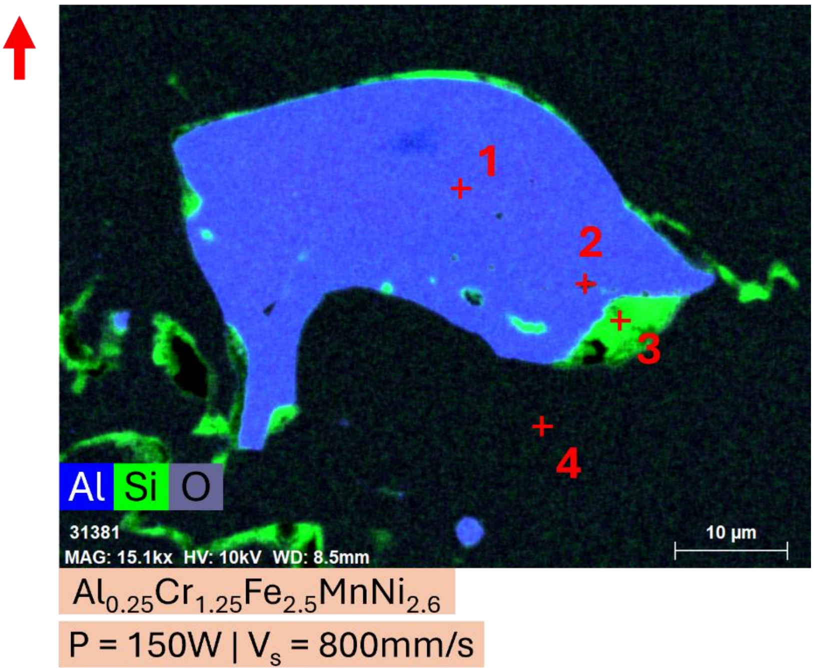

Figure 59: SEM-micrograph of $Al_{0.25}Cr_{1.25}Fe_{2.5}MnNi_{2.6}$ cubic sample (P = 150W | V_s = 800mm/s) with EDX point analysis for Al, Si, and O elements

Semi-quantitative EDX point analysis performed at selected locations (Table 17) confirm these observations. Point 1, located within the inclusion, exhibits a high aluminum and oxygen content, consistent with aluminum oxide formation. Point 3, corresponding to the interfacial region, shows elevated silicon and oxygen contents, indicating the presence of a silicon oxide layer. Localized regions with high manganese content are also observed. Point 4 corresponds to the FCC matrix.

Table 17: Chemical composition (wt. %) of EDX point analysis (Figure 59) of $Al_{0.25}Cr_{1.25}Fe_{2.5}MnNi_{2.6}$ cubic sample (P = 150W | V_s = 800mm/s)

Spectrum	Al	Cr	Fe	Mn	Ni	Si	O
1 – wt.%	44.63	0.93	-	4.95	-	-	18.18
2 – wt.%	1.56	4.37	13.03	61.33	11.01	2.19	-
3 – wt.%	-	1.13	3.03	0.79	-	33.76	32.84
4 – wt.%	3.31	14.03	29.15	12.79	26.54	1.21	8.93

Figure 60 and Figure 61 present SEM micrographs revealing the presence of nano scale inclusions distributed throughout the build.

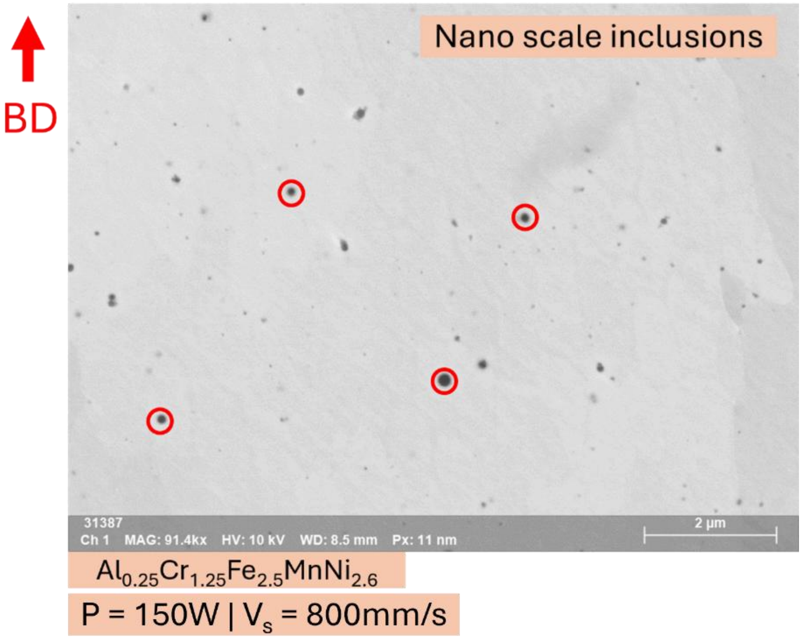

Figure 60: SEM-micrograph of $Al_{0.25}Cr_{1.25}Fe_{2.5}MnNi_{2.6}$ cubic sample

In the $Al_{0.25}Cr_{1.25}Fe_{2.5}MnNi_{2.6}$ cubic samples, these inclusions are homogeneously dispersed within the FCC matrix and are observed across the entire build. Microcracks are frequently observed in the surroundings of these nano scale inclusions.

Semi-quantitative EDX analyses performed on these features (Table 18) indicate that the nano-scale inclusions are enriched in aluminum and oxygen, confirming their oxide nature. Silicon is also detected in significant amounts.

Table 18: Chemical composition median in at. %, wt. %, and normalized wt.%, of Al, O, and Si elements of the nano scale inclusions in $Al_{0.25}Cr_{1.25}Fe_{2.5}MnNi_{2.6}$ cubic sample (P = 150W | V_s = 800mm/s)

Spectrum	Al	O	Si
at. %	16.6 ± 5.8	77.9 ± 3.8	6.1 ± 2
wt. %	1.40 ± 0.5	3.6 ± 0.9	0.6 ± 0.2
wt. %n	24.4 ± 7.9	67.4 ± 4.7	9.2 ± 3.2

Similar nano scale inclusions are also observed in the $CrFe_{2.1}MnNi_2$ samples, as shown in Figure 61. In this case, the inclusions are enriched in silicon and oxygen, indicating the formation of silicon oxide inclusions. These features are distributed throughout the build and are occasionally associated with microcracks.

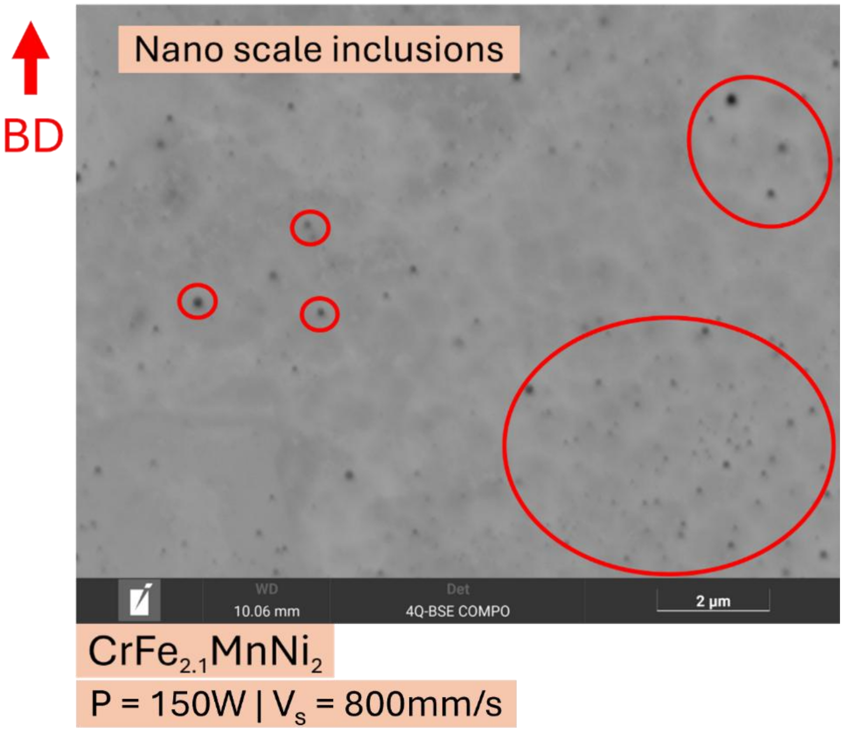

Figure 61: SEM-micrograph of $CrFe_{2.1}MnNi_2$ cubic sample

4. Discussions

This section aims to interpret the experimental observations by linking microstructural features, defect formation mechanisms, and processing-composition interactions in the investigated LPBF fabricated alloys. The subjects will focus on the formation of hot cracks, combining experimental results with solidification theory to explain the effects of solute segregation, mushy zone behavior, residual stresses, and processing conditions.

Oxidation phenomena and non-metallic inclusions will also be examined by addressing their origin, chemical nature, and interaction with the surrounding microstructure, as well as their secondary contribution to crack initiation and propagation.

The combined influence of alloy composition and LPBF parameters on densification, surface quality, porosity, phase constitution, and grain morphology is also discussed. It highlights the physical mechanisms governing melt pool stability and defect sensitivity.

Finally, the intrinsic limitations associated with the use of multiple powder mixtures will be discussed, including chemical deviations, powder related heterogeneities, and their implications for process stability and microstructural control.

4.1. Hot cracks formation

Hot cracks were systematically observed in every LPBF cubic sample and predominantly exhibited an intergranular morphology, as shown in Figure 50 and Figure 51. This morphology indicates cracking mechanisms occurring during the solidification. Solidification cracks form during the final stages of solidification when a semi-solid mushy zone is subjected to tensile stresses arising from thermal contraction and constrained shrinkage. This cracking mode is well documented in welding and laser-based additive manufacturing processes, where steep thermal gradients, rapid solidification rates, and repeated thermal cycling promote crack initiation along weakened grain boundaries [10,17,26,52].

A major factor contributing to hot crack formation in this study is elemental segregation at grain boundaries, particularly involving silicon. Silicon was not intentionally alloyed but originates from the use of multiple mixed powders. As reported in previous work[53], hot cracks were identified as Si-rich, providing direct experimental evidence that silicon segregates preferentially to crack-prone regions. In multicomponent alloys, including high-entropy alloys, solute partitioning during solidification is common and can be amplified under non-equilibrium solidification conditions such as those encountered in LPBF. Even small compositional deviations may significantly alter local solidification behavior and grain boundary chemistry [40,41,53].

During solidification, silicon exhibits a strong tendency to partition to the liquid phase. This behavior implies that silicon is rejected by the advancing solid-liquid interface and progressively enriches the remaining liquid as solidification proceeds. Under rapid solidification conditions of LPBF, this effect is further amplified because limited solid-state diffusion prevents homogenization of solute elements within the growing grains. As a result, silicon accumulates in the last regions to solidify, in the interdendritic channels and grain boundary regions, as illustrated in Figure 62. This segregation leads to the formation of a continuous Si-rich interdendritic liquid film between adjacent growing grains. Due to its relatively low melting temperature, silicon locally reduces the solidus temperature and significantly widens the solidification range. This effectively increases the lifetime of the mushy zone during the final stages of solidification. According to classical solidification cracking theory, an extended mushy zone delays grain coalescence and maintains weak, liquid-containing grain boundaries over a wider temperature range. Under these conditions, interdendritic liquid feeding becomes increasingly difficult, while tensile stresses generated by thermal contraction accumulate. This combination markedly increases crack susceptibility by promoting the rupture of Si-rich liquid films along grain boundaries [9,10,52,53].

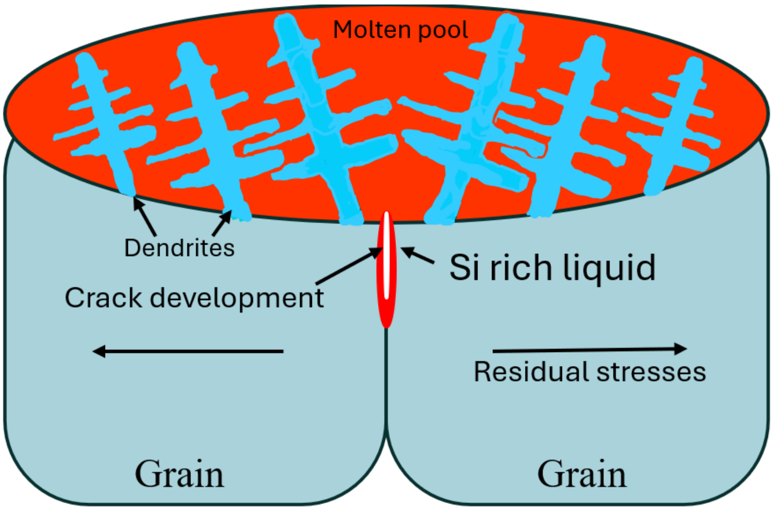

Figure 62:Illustration of solidification cracking due to segregation of Si-rich liquid along grain boundary and the development of cracks driven by residual tensile stresses between adjacent grains [53]

As solidification proceeds and the melt pool cools, volumetric shrinkage occurs in the surrounding solid. Under ideal conditions, this shrinkage can be inhibited by interdendritic liquid feeding, which compensates for contraction during solidification. However, when the remaining liquid is confined to thin, discontinuous Si-rich films, liquid feeding becomes severely restricted. As a result, tensile stresses build up across grain boundaries. When the local tensile stress exceeds the cohesive strength of the weakened intergranular region, the liquid film ruptures, initiating an intergranular crack. Upon further cooling, the Si-rich liquid solidifies into a mechanically weak and brittle intergranular region, along which cracks propagate. The combination of segregation, limited feeding, stress accumulation, and liquid film rupture is a typical solidification cracking mechanism and is extensively described in welding metallurgy literature [10,26,52].

Residual stresses generated during LPBF further intensify this mechanism. The extremely steep thermal gradients inherent to the process induce tensile residual stresses during the final cooling stages. Adjacent grains experience differential thermal contraction, and when grain boundaries are chemically weakened by segregation, they become preferential paths for crack initiation and propagation [17,26].

A higher density of hot cracks was also systematically observed near the top layer of the builds compared to the underlying regions, as shown in Figure 51. This increase in crack density is consistent across all samples investigated. The top layers correspond to the final stages of the build, where solidification occurs under different thermal conditions than in the bulk, and where tracks are no longer remelted, leaving cracks that formed during the last solidification cycles unhealed by subsequent layer deposition.

In addition to segregation driven mechanisms, partially melted or unmelted powder particles were frequently observed near cracks, as observed in Figure 51 and Figure 52. These particles introduce localized heterogeneities in both chemical composition and thermophysical properties, such as thermal conductivity and thermal expansion coefficient. During solidification, such heterogeneities generate local shrinkage mismatches and stress concentrations that promote crack initiation. Moreover, partially melted particles disrupt melt pool continuity and locally inhibit interdendritic liquid feeding, further increasing susceptibility to solidification cracking. The coexistence of chemically and structurally distinct microstructural regions around these particles also reduces local cohesion compared to a homogeneous matrix, facilitating crack propagation [13,33].

Oxide inclusions may also promote crack formation by introducing local brittle heterogeneities and acting as stress concentrators within the structure [30,31]. Both micro-scale and nano-scale oxide inclusions were observed throughout the build (Figure 60 and Figure 61). These inclusions, combined with grain boundary weakening and residual tensile stresses, promote cracks initiation and propagation. The formation mechanisms, chemistry and distribution of these oxide inclusions are discussed in detail in the dedicated section 4.2.

The formation of hot cracks in the present work can be attributed to the combined effect of silicon segregation to grain boundaries, widening of the mushy zone, insufficient interdendritic liquid feeding, thermal shrinkage, and residual stress accumulation. All these effects are further exacerbated by the use of multiple powder mixtures containing undesired elements such as silicon.

In the present work, mitigation strategies commonly employed to reduce hot cracking in LPBF were implemented, including substrate preheating to 500°C and the use of a 67-67 rotating scan strategy. Preheating is known to reduce thermal gradients, lower cooling rates, and decrease residual stress accumulation during solidification, while rotating scan strategies promote a more homogeneous heat distribution and reduce directional stress build-up.

Despite the implementation of these measures, hot cracking was systematically observed in all samples. This indicates that, under the conditions investigated, stress-mitigation strategies alone were insufficient to suppress cracking. The persistence of hot cracks suggests that the dominant cracking mechanism is governed by chemical effects, particularly silicon segregation and the associated widening of the mushy zone, rather than by residual stress magnitude alone. While preheating and scan strategy optimization likely reduce crack severity, they do not fully counteract the formation of weak, liquid-containing grain boundaries during the final stages of solidification.

4.2. Oxidation and inclusions

Oxide inclusions were systematically observed in all LPBF samples investigated at both the micro- and nano-scale, regardless of alloy composition (Figure 60 and Figure 61). In Al-containing alloys, inclusions were primarily composed of aluminum oxides, whereas in the Al-free composition, silicon oxide inclusions were predominantly observed (Figure 56 and Figure 58). These observations indicate that oxidation phenomena are intrinsic to the processing route employed in this study and are strongly influenced by the chemical nature of the alloy constituents [10,13,26].

The formation of aluminum-rich oxide inclusions in Al-containing alloys is thermodynamically favored due to the high oxygen affinity of aluminum [35,52]. Ellingham diagrams indicate that aluminum oxidizes preferentially compared to other alloying elements, including silicon [54]. As a result, even trace oxygen levels in the processing atmosphere or oxygen originating from powder surfaces can lead to the formation of stable aluminum oxides during LPBF, as shown in Figure 58 and Figure 59 [10,26]. In contrast, for alloys without aluminum, silicon becomes the most reactive element with respect to oxygen, explaining the prevalence of silicon oxide inclusions in the $CrFe_{2.1}MnNi_2$ compositions (Figure 56 and Figure 57) [55].

This interpretation is supported by the DTA results (Figure 25 and Table 14), which revealed exothermic events associated with oxide formation during cooling [52,56,57]. These thermal signatures indicate that oxidation reactions occur during solidification, suggesting that oxide inclusions are formed in situ rather than exclusively inherited from pre-existing powder surface oxide [10,58].

A recurring feature observed in both alloy compositions is the presence of chemically stratified inclusions. In Al-containing alloys, aluminum oxide inclusions are surrounded by a silicon-rich oxide layer, forming a distinct interfacial region between the inclusion core and the surrounding FCC matrix (Figure 58 and Figure 59) [58,59]. Similarly, in Al-free alloys, silicon oxide inclusions are frequently surrounded by a manganese-enriched layer (Figure 56 and Figure 57). These layered structures suggest that oxidation and subsequent elemental redistribution occur dynamically during melting and solidification, leading to complex inclusion morphologies rather than chemically homogeneous particles [10,56,58]. The presence of Mn-enriched interfacial layers further indicates that oxidation processes are coupled with local solute redistribution during solidification, contributing to chemical heterogeneity at inclusion-matrix interfaces [56,58].

Nano-scale oxidation inclusions were found to be homogeneously distributed throughout the build volume for both alloys (Figure 60 and Figure 61). EDX analyses confirmed that these nano-inclusions exhibit chemical compositions consistent with aluminum or silicon oxides, depending on the alloy (Table 18). The presence of such inclusions at multiple length scales indicates that oxidation is not limited to isolated events but rather occurs repeatedly throughout the LBFP process [10,26]. Their widespread distribution suggests that oxidation originates from a combination of residual oxygen in the processing chamber, surface oxides present on the starting powders, and repeated remelting during layer-by-layer fabrication [13,26,60].

Although oxide inclusions are not considered the primary driving force of hot crack formation, their contribution to crack initiation and propagation should not be neglected [7,10]. Oxide inclusions introduce local chemical and mechanical heterogeneities within the microstructure and act as brittle entities embedded in a ductile FCC matrix [7,32]. When located along grain boundaries or in the surroundings of partially melted powder particles, these inclusions act as local stress concentrators and reduce grain boundary cohesion, as shown in Figure 51 to Figure 53 [10,15]. This effect is particularly pronounced when combined with silicon segregation, residual tensile stresses, and restricted interdendritic liquid feeding, which collectively weaken grain boundaries during the final stages of solidification [52,56,61].

In addition, nano-scale oxide inclusions were frequently observed in association with microcracks (Figure 60 and Figure 61). While their presence alone is insufficient to trigger cracking, their interaction with stress fields generated during rapid cooling and solidification can locally promote crack initiation [10]. At the micro-scale, oxide inclusions embedded at or near grain boundaries may serve as preferential sites for crack deflection or crack initiation, particularly in regions already weakened by solute segregation or partial melting (Figure 51 and Figure 55) [7,15].

Overall, the oxidation phenomena observed in this study contribute to microstructural heterogeneity across multiple length scales [10,13]. While oxide inclusions are not the dominant mechanism responsible for hot cracking, they play a secondary yet non-negligible role by locally weakening the microstructure and facilitating crack initiation or propagation when combined with solidification-related mechanisms [7,32]. These findings highlight the importance of controlling oxygen content, powder quality, and powder mixing strategies when processing multicomponent alloys by LPBF, particularly when undesired elements such as silicon are present [13,22,60].

4.3. Impact of processing parameters and composition on final part

The combined analysis of DTA experiments, LPBF process maps, density measurements, surface profilometry, and microstructural characterization highlights the strong interplay between alloy composition and processing parameters in determining final part quality [10,13,15]. These results demonstrate that compositional effects govern phase stability and defect sensitivity, while processing parameters primarily control melt pool stability, energy input, and defect morphology.

DTA analysis highlights aluminum as a primary factor of the solidification path and phase constitution (Figure 26 to Figure 31). The Al-free $CrFe_{2.1}MnNi_2$ alloy solidifies into a fully FCC microstructure (Figure 26), reflecting the high FCC stability expected for this composition and confirming thermodynamic predictions. Introducing a limited aluminum content ($Al_{0.25}$) does not significantly destabilize the FCC phase, as the microstructure remains predominantly FCC with only minor secondary features at grain boundaries (Figure 27). This indicates that, at low concentrations, aluminum does not sufficiently alter the thermodynamic balance to induce phase transformation.

At higher aluminum concentrations ($Al_{0.4}$ and $Al_{0.9}$), however, the formation of BCC/B2 regions within the FCC matrix and the formation of inclusions such as MnS (Figure 28 and Figure 29) indicate a fundamental change in solidification behavior. This transition is consistent with aluminum's strong effect on valence electron concentration and mixing enthalpy, which progressively destabilizes the FCC solid solution and promotes BCC/B2 formation [40,62]. Higher magnification observations further reveal intermetallic phases embedded within BCC/B2 regions (Figure 30), demonstrating that increasing aluminum content not only modifies phase stability but also microstructural complexity, in agreement with Thermo-Calc predictions.

Comparable phase constitutions were observed in LPBF-processed samples (Figure 46 and Figure 47), indicating that the rapid solidification and non-equilibrium conditions inherent to LPBF do not fundamentally alter the dominant phase selection relative to near-equilibrium DTA conditions [9,10,27]. This suggests that, for the investigated alloys, phase stability is primarily dictated by chemical composition, while LPBF processing mainly influences microstructural scale and defect formation rather than phase type [40,62]. The repeated remelting and thermal cycling characteristic of LPBF also promotes local chemical homogenization within melt pools, which reduces the persistence of metastable phases that could otherwise form during a single rapid solidification event [10,17]. As a result, LPBF primarily affects microstructural length scales, such as grain size, cellular spacing, and defect density, rather than altering the dominant phase constitution predicted under near-equilibrium conditions [9,10,40].

Single track experiments performed on the $CrFe_{2.1}MnNi_2$ alloy provided initial insight into printability and melt pool stability (Figure 32). The selected processing window favored relatively low scan speeds, as scan speeds above 1,000mm/s were excluded from cubic samples fabrication. This choice avoided high surface damage regions identified in the process map (Figure 32). However, spatter was still observed within the selected parameter sets (Figure 33.c). Spatter formation in LPBF is strongly associated with recoil pressure induced by metal vaporization, Marangoni driven melt flow, and keyhole oscillations, all of which can occur even at moderate scan speeds when local energy density and absorptivity are high [10,17,63]. The ejection of molten droplets and powder particles from the melt pool can redeposit onto the surrounding powder bed, locally disturbing layer uniformity and shielding subsequent laser interaction [10,15,26].

For cubic samples, the $CrFe_{2.1}MnNi_2$ alloy was investigated more extensively (Figure 34 and Figure 35), enabling the identification of distinct defect regimes, including lack-of-fusion and keyhole porosity, as well as regions characterized by reduced defect density (Figure 35). The existence of a narrow region with reduced defect density reflects the balance of printing parameters to achieve sufficient melt pool penetration and avoid excessive vaporization.

At low energy densities, insufficient melt pool depth and poor overlap between adjacent tracks limit bonding, leading to lack-of-fusion defects. At high energy densities, excessive vaporization and unstable keyhole dynamics promote pore entrapment and spatter formation, degrading part quality [10,17,63]. The observed narrow optimal window therefore corresponds to conditions where energy input is sufficient to ensure full consolidation while maintaining melt pool stability.

Top view analysis of the cubic samples revealed a pronounced influence of argon gas flow direction for both alloy compositions (Figure 34 to Figure 37). Cubes located on the left side of the build plate consistently exhibited poorer surface quality, indicating that spatters ejected from upstream tracks were transported by the gas flow and redeposited onto downstream samples (Figure 34 to Figure 37) [15,26]. The reproducibility of this behavior across both alloy systems suggests that gas flow driven spatter redeposition plays a significant role in surface degradation and defect formation, independent of alloy chemistry [15,26].

Density measurements reveal how densification in LBPF results from the balance between melt pool penetration, track overlap, and vaporization-driven instabilities, all of which are strongly affected by both scan speed and alloy composition (Figure 38 and Figure 39). For both alloys, the highest relative densities were obtained at scan speeds between 600 and 800mm/s, which corresponds to a regime where the laser-material interaction time is sufficient to generate a melt pool deep and wide enough to ensure bonding between adjacent tracks and layers, while still avoiding excessive peak temperatures that promote vaporization and keyhole instability. This behavior is consistent with the conduction to keyhole transition framework in the literature, which shows that insufficient energy input leads to lack-of-fusion porosity, whereas excessive local energy density drives strong recoil pressure, melt pool oscillations, and pore entrapment [17,26].

Although both alloys have similar optimal scan speed range, the laser powder window required to achieve maximum density differs between compositions, reflecting the influence of chemical composition on melt pool thermophysical behavior. In the $CrFe_{2.1}MnNi_2$ alloy, high densities (up to approximately 98.5%) were achieved over a relatively broad power range of 125 to 185W (Figure 38), indicating a comparatively robust conduction mode regime in which variations in power do not immediately destabilize the melt pool. Such robustness has been reported for FCC solid-solution alloys with moderate absorptivity and thermal conductivity, where heat dissipation limits the onset of keyhole instability [10,28]. In contrast, $Al_{0.25}Cr_{1.25}Fe_{2.5}MnNi_{2.6}$ samples reached densities above 99% only within a narrower power window of 150-175W (Figure 39), suggesting that the presence of aluminum increases the sensitivity of melt pool stability to energy input. Aluminum is known to modify laser absorptivity, surface tension gradients, and vaporization behavior, therefore amplifying Marangoni convection and recoil pressure effects at elevated temperatures [9,10,17]. As a result, small deviations in power more readily shift the process from a stable conduction regime to an unstable vaporization dominated regime, explaining the narrower processing window. Despite this sensitivity, the Al-containing alloy exhibited a higher average density than the Al-free composition, indicating that once a stable melt pool regime is achieved, aluminum addition can promote improved consolidation under the investigated conditions.

Surface profilometry further demonstrates that surface integrity is governed by melt pool dynamics and spatter behavior rather than densification alone (Figure 40 to Figure 43). Removing the lowest scan speed of 200mm/s for $Al_{0.25}Cr_{1.25}Fe_{2.5}MnNi_{2.6}$ significantly improved average surface quality, because low scan speeds increase local energy input and peak temperature, intensifying vaporization and melt pool instability. In $CrFe_{2.1}MnNi_2$ samples produced at 200mm/s, average top layer heights exceeded 120µm (Figure 42.a), reflecting severe surface irregularities associated with spatter redeposition and unstable melt pool flow. Similar mechanisms have been widely reported in LPBF literature, where excessive energy input leads to balling, spatter ejection, and surface roughening [26,29].

Although Al-containing samples exhibited lower average surface heights overall (Figure 42.b), maximum height values were particularly poor at 400mm/s (Figure 43). This behavior indicates that aluminum addition shifts the optimal surface quality window, likely due to changes in surface tension gradients and melt pool flow patterns. Moreover, these samples were located on the left side of the build plate, where argon gas flow transported spatters from upstream tracks (Figure 34 to Figure 37). Gas flow driven spatter redeposition is known to locally disrupt powder bed uniformity and laser absorption, thereby amplifying surface defects independently of nominal process parameters [9,15].

The absence of a systematic correspondence between optimal surface profile (Figure 42 and Figure 43) and maximum densities (Figure 38 and Figure 39) reflects that surface roughness, density, and porosity arise from partially independent physical mechanisms. While density is primarily controlled by melt pool penetration and track overlap, surface roughness is strongly influenced by spatter redeposition, melt pool oscillations, and powder bed disturbances, which do not necessarily scale with densification [10,26].

Porosity analysis further reinforces this decoupling (Figure 44). For both alloys, samples fabricated at 200mm/s exhibited the highest porosity, consistent with excessive energy input driving vaporization and unstable melt pool behavior. In $CrFe_{2.1}MnNi_2$ samples, porosity decreased monotonically with increasing scan speed, reaching minimum values at 600-800mm/s (Figure 44.a), where stable conduction mode melting and sufficient overlap are maintained. In contrast, Al-containing samples exhibited a more complex response (Figure 44.b), with both the best and worst porosity values occurring within similar scan speed ranges. Notably, a sample fabricated at 100W and 400mm/s exhibited the lowest porosity while simultaneously showing poor density and surface quality (Figure 39 and Figure 42.b). This indicates that porosity minimization alone does not guarantee adequate consolidation or surface integrity, as pores can be suppressed even when melt pool geometry or surface stability remain suboptimal. Similar decoupling between porosity, density, and surface roughness has been reported for LPBF alloys with composition-dependent melt pool dynamics [28,33].

The average porosity of Al-containing samples was approximately half that of $CrFe_{2.1}MnNi_2$ samples (Figure 44), indicating a generally superior bulk quality for the aluminum-containing alloy under the investigated conditions. This improvement is consistent with the enhanced melt pool fluidity and modified Marangoni flow associated with aluminum additions, which can improve pore healing when melt pool stability is preserved [10,43].

EBSD analysis revealed fully FCC microstructures in all LPBF printed samples for both compositions (Figure 46 and Figure 47), consistent with DTA observations (Figure 26 and Figure 27). This confirms that, despite the strongly non-equilibrium nature of LPBF, dominant phase selection remains governed by alloy chemistry rather than processing routes. In compositionally complex alloys, the free-energy differences between competing phases are sufficiently large that rapid solidification does not suppress the formation of the thermodynamically favored phase [40,56].

Both alloys exhibited elongated columnar grains aligned with the build direction (Figure 48 and Figure 49), resulting from directional solidification under steep vertical thermal gradients. In

LBPF, heat is extracted predominantly through the previously solidified material, promoting epitaxial grain growth and suppressing new nucleation. This behavior is a direct consequence of the high thermal gradients relative to cooling rates, as described by classical solidification theory [27,56,64].

Regarding defects, hot cracks were systematically observed across all samples (Figure 50 and Figure 51), as discussed in detail in section 4.1. Lack-of-fusion pores were present across a wide range of parameters, including at high volumetric energy densities (Figure 54), indicating that incomplete melting and local powder bed heterogeneities persist even under nominally sufficient energy input. Keyhole pores appeared at high energy densities (Figure 54.a) but did not dominate the porosity population, while gas pores were detected across all processing parameters without a clear dependence on laser power or scan speed (Figure 54.b and Figure 54.c). Such coexistence of pore types reflects the stochastic nature of LPBF melt pool dynamics and powder-laser interactions [15,26].

Overall, these results demonstrate that alloy composition controls phase stability and melt pool sensitivity, while processing parameters regulate energy distribution, melt pool geometry, and spatter dynamics. The lack of direct correlations between density, surface roughness, and porosity highlights the intrinsic complexity of LBPF process optimization for multicomponent alloys. Aluminum addition improves densification and reduces average porosity but simultaneously narrows the stable processing window, emphasizing the necessity of composition specific process optimization strategies rather than universal parameter sets [10,43].

4.4. Limitations of multiple powders mixtures

The use of multiple commercially available powders to produce tailored alloy compositions introduces several intrinsic limitations that affect powder handling, chemical accuracy, and final part quality [11,22,24].

The use of multiple powders with different particles sizes distributions, morphologies, and surface chemistry inherently reduces powder homogeneity and spreadability compared to pre-alloyed powders [21,22]. To mitigate these effects, a mixing strategy was implemented to minimize the number of powders used, maximize individual powder utilization, and ensure compatibility with commercially available feedstocks [30,63].

Despite the optimization, deviations from the target compositions were unavoidable (Table 10). These deviations originate from the imperfect compositional match between available powders and the target alloy but also from the presence of undesired elements inherent to the powders themselves (Table 2) [22,63]. The hand mixing method employed in this study further contributes to compositional uncertainty, as it lacks reproducibility and homogeneity achievable with industrial mixing techniques (Table 11 and Table 12) [30,63].

Following composition optimization and hand mixing, deviations for aluminum, chromium, iron, and nickel remained small when considered on a relative basis (Table 12). In contrast, manganese content exhibited a standard deviation of around 25 at. %, while silicon content nearly doubled compared to target values (Table 12). The pronounced deviation for Mn may not only originate from powder mixing uncertainty but can also be attributed to preferential volatilization during LPBF processing. Due to the extremely high local temperatures reached in the melt pool, selective evaporation of alloying elements with comparatively high vapor pressures can occur. Manganese is frequently reported as being more prone to volatilization than many transition metals under laser processing conditions, leading to local Mn depletion and composition drift during LPBF fabrication [10,17,26,64,65]. The silicon enrichment is particularly critical, as silicon was meant to be minimized as it was previously identified as a key contributor to hot cracking through grain boundary segregation (cfr. Section 4.1) [10,17]. The amplification of silicon content highlights a fundamental limitation of powder mixing approaches when undesired elements are present in multiple feedstocks [22,63].

The powder used in this work exhibited different particles size distributions and morphologies (Figure 15 and Table 3). While the 316L, Ni-Cr, and aluminum powders were predominantly spherical, manganese powders displayed a more irregular morphology. Such irregular particles are known to negatively affect powder flowability and layer uniformity, which can decrease powder spreading and lead to local variations in powder bed density [19–21].

Differences in particle size have a dual effect. On the one hand, a broader particle size distribution can increase packing density by allowing smaller particles to fill interstitial spaces between larger ones, as illustrated in Figure 63 [21]. Higher packing density may improve local powder bed density and potentially enhance laser-powder interaction [10,26]. On the other hand, increased packing density does not necessarily imply improved spreadability. In fact, the presence of fine particles often increases interparticle cohesion and reduces flowability, particularly when combined with irregular particle shapes [20,21]. Therefore, while broad particle size distribution mixtures may locally increase packing density, they may simultaneously degrade powder spreading behavior [20].

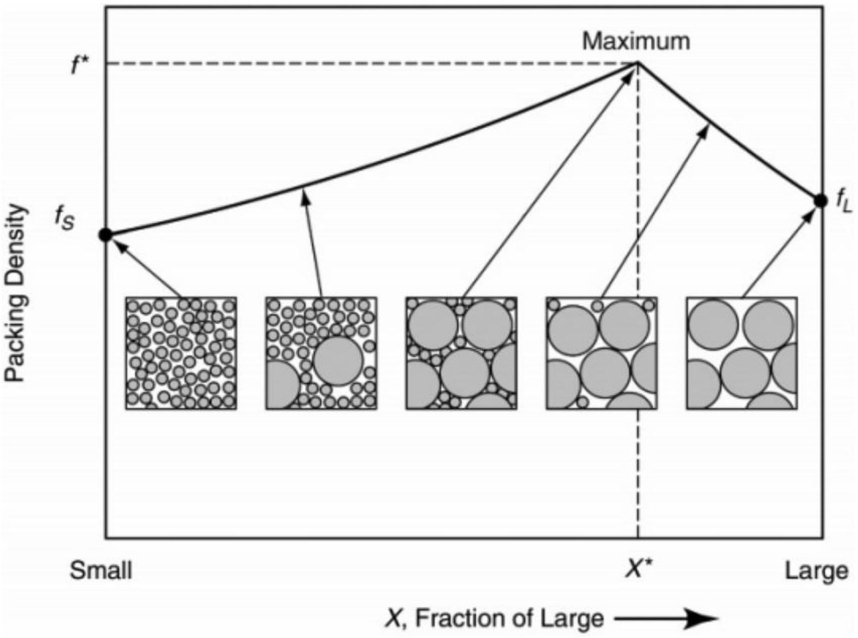

Figure 63: Relation between particle packing density and particle size distribution [75]

Heterogeneous powder mixtures may lead to local compositional variations within the powder bed, which in turn can affect local absorptivity, thermal conductivity, and melting behavior during LPBF [13,17]. Such local variations can promote uneven melting, resulting in lack-of-fusion pores or partially melted particles [10,56]. Furthermore, localized enrichment in brittle or low melting point elements may create preferential sites for crack initiation during solidification [10,56].

The frequent observation of unmelted or partially melted powder particles, even within optimized processing windows, suggests that certain powders exhibit thermophysical properties that differ significantly from the surrounding matrix [10,26]. In a multi-powder system, these differences may lead to selective melting behavior, where specific particles are more prone to incomplete melting [30]. This phenomenon may locally deplete the surrounding matrix in certain elements while simultaneously increasing chemical heterogeneity in the solidified material [10,63].

Compared to pre-alloyed powders, multiple powders mixtures inherently increase the risk of microstructural heterogeneity, chemical segregation, and defect formation [22,24,30]. While such approaches offer flexibility in alloy design and rapid compositional screening, they impose significant constraints on powder handling, chemical control, and process stability [11,63]. These limitations are further exacerbated when undesired elements such as silicon are present, as their concentration may unintentionally increase during mixing significantly influence solidification behavior and defect sensitivity [10,17].

Overall, while multiple powders mixture represents a practical and cost-effective approach for exploratory alloy development, the present results demonstrate that it introduces intrinsic limitations that must be carefully managed. Improved mixing techniques, tighter control of powder chemistry and printing atmosphere, and also the use of pre-alloyed powders may be necessary to fully exploit the potential of complex alloys in LPBF [11,22,30].

5. Conclusions

- Hot cracking was systematically observed in all LPBF samples, despite substrate preheating and scan strategy optimization. The results indicate that, for the investigated alloys, cracking susceptibility is strongly influenced by alloy chemistry, particularly the presence of silicon, and cannot be suppressed by stress mitigation strategies alone under the conditions explored.

- Oxide inclusions were present in all samples. In Al-containing alloys, aluminum-rich oxides were predominant, with silicon enrichment at the oxide-matrix interface. In Al-free compositions, silicon oxide inclusions were dominant, often associated with manganese enrichment. These observations suggest composition-dependent oxidation behavior during LPBF.

- Processability was strongly composition dependent. Different combinations of laser power and scan speed led to distinct optimal windows in terms of density and surface quality. Aluminum addition improved average densification but reduced the width of the optimal processing window.

- All LPBF samples exhibited fully FCC microstructures with columnar grains aligned with the build direction. Phase constitution and grain morphology were consistent across processing conditions, suggesting that phase stability is primarily controlled by alloy composition for the studied alloys.

- The use of multiple powder mixtures led to deviations from target compositions, increased silicon content, and reduced powder homogeneity. These factors are likely to contribute to chemical heterogeneity and defect formation. While suitable for exploratory alloy development, mixed powder approaches impose limitations compared to pre-alloyed powders.

6. Perspectives

- Reprinting the selected compositions using powders with optimized and more uniform particle size distributions and morphologies could improve powder spreadability and packing density. It could be expected to obtain enhanced density and top layer surface quality, while lowering porosity and microstructural defects.

- Replacing manual hand mixing with controlled industrial mixing techniques would likely improve powder homogeneity and reproducibility. Enhanced mixing could reduce local compositional variations, lower the occurrence of unmelted powder particles, and improve powder bed uniformity.

- Using pre-alloyed powders could also be investigated to overcome multiple powders mixtures intrinsic limitations. Pre-alloyed powders would also enhance chemical composition precision by reducing compositional deviations from target alloys, and limiting undesired parasitic elements such as silicon. This could mitigate segregation effects, and hot cracks, while promoting homogeneous microstructures.

- Further investigations could focus on identifying which specific powders are most prone to incomplete melting during LPBF. This could be performed using EDX analyses of unmelted particles and could help adapt powders and processing parameters selection.

- Additional characterization to determine the alloys properties could also be performed, particularly corrosion resistance, in order to determine their potential applications. Comparative tests between Al-free and Al-containing alloys could also help identify the optimal compositions for specific environment and determine the role of aluminum on corrosion behavior.

- Using vacuum or ultra-low oxygen printing environment could be explored to limit the formation of oxides during processing. Reducing oxygen availability may significantly decrease the formation of aluminum and silicon oxides, leading to improved microstructures, fewer inclusions, and potential reduction of crack initiation sites.

References

1. Dobrzańska-Danikiewicz AD, Bączyk A. A review of additive manufacturing technologies. Archives of Materials Science and Engineering. 2024 Aug 1;128(1).
2. Iftekar SF, Aabid A, Amir A, Baig M. Advancements and Limitations in 3D Printing Materials and Technologies: A Critical Review. Polymers (Basel). 2023 May 30;15(11).
3. Koltsaki M, Mavri M. A Comprehensive Overview of Additive Manufacturing Processes Through a Time-Based Classification Model. 3D Print Addit Manuf. 2024 Feb 1;11(1):363–82.
4. Mertens A. Additive Manufacturing and 3D printing: Course lectures. Liège; 2023.
5. Marchal Y. Manufacturing Processes: Course lectures. Liège; 2023.
6. Biedermann M. Automated Design of Additive Manufactured Flow Components [Internet]. Technical University of Munich; 2022. Available from: https://doi.org/https://doi.org/10.3929/ethz-b-000587405
7. Bellini C, Berto F, Cocco V Di, Iacoviello F, Mocanu LP, Razavi N. Additive manufacturing processes for metals and effects of defects on mechanical strength: a review. Procedia Structural Integrity. 2021;33:498–508.
8. Barroqueiro B, Andrade-Campos A, Valente RAF, Neto V. Metal Additive Manufacturing Cycle in Aerospace Industry: A Comprehensive Review. Journal of Manufacturing and Materials Processing. 2019 Jun 26;3(3):52.
9. Herzog D, Seyda V, Wycisk E, Emmelmann C. Additive manufacturing of metals. Acta Mater. 2016 Sep;117:371–92.
10. DebRoy T, Wei HL, Zuback JS, Mukherjee T, Elmer JW, Milewski JO, et al. Additive manufacturing of metallic components – Process, structure and properties. Prog Mater Sci [Internet]. 2018 Mar;92:112–224. Available from: https://linkinghub.elsevier.com/retrieve/pii/S0079642517301172
11. Vafadar A, Guzzomi F, Rassau A, Hayward K. Advances in Metal Additive Manufacturing: A Review of Common Processes, Industrial Applications, and Current Challenges. Applied Sciences [Internet]. 2021 Jan 28;11(3):1213. Available from: https://www.mdpi.com/2076-3417/11/3/1213

12. Gibson I, Rosen D, Stucker B, Khorasani M. Additive Manufacturing Technologies [Internet]. Cham: Springer International Publishing; 2021. Available from: https://link.springer.com/10.1007/978-3-030-56127-7

13. Chowdhury S, Yadaiah N, Prakash C, Ramakrishna S, Dixit S, Gupta LR, et al. Laser powder bed fusion: a state-of-the-art review of the technology, materials, properties & defects, and numerical modelling. Journal of Materials Research and Technology. 2022 Sep;20:2109–72.

14. Pantawane M V., Ho YH, Joshi SS, Dahotre NB. Computational Assessment of Thermokinetics and Associated Microstructural Evolution in Laser Powder Bed Fusion Manufacturing of Ti6Al4V Alloy. Sci Rep. 2020 May 5;10(1):7579.

15. Guillen D, Wahlquist S, Ali A. Critical Review of LPBF Metal Print Defects Detection: Roles of Selective Sensing Technology. Applied Sciences. 2024 Aug 1;14(15):6718.

16. Liang A, Pey KS, Polcar T, Hamilton AR. Effects of rescanning parameters on densification and microstructural refinement of 316L stainless steel fabricated by laser powder bed fusion. J Mater Process Technol. 2022 Apr;302:117493.

17. Zhao C, Shi B, Chen S, Du D, Sun T, Simonds BJ, et al. Laser melting modes in metal powder bed fusion additive manufacturing. Rev Mod Phys. 2022 Oct 20;94(4):045002.

18. Wang J, Zhu R, Liu Y, Zhang L. Understanding melt pool characteristics in laser powder bed fusion: An overview of single- and multi-track melt pools for process optimization. Advanced Powder Materials. 2023 Oct;2(4):100137.

19. Niu HJ, Chang ITH. Selective laser sintering of gas and water atomized high speed steel powders. Scr Mater. 1999 Jun;41(1):25–30.

20. Mussatto A, Groarke R, O’Neill A, Obeidi MA, Delaure Y, Brabazon D. Influences of powder morphology and spreading parameters on the powder bed topography uniformity in powder bed fusion metal additive manufacturing. Addit Manuf. 2021 Feb;38:101807.

21. Fedina T, Sundqvist J, Kaplan AFH. The role of powder morphology in particle movement behavior in laser powder bed fusion with an emphasis on fluid drag. Powder Technol. 2022 Jan;395:720–31.

22. Antony LVM, Reddy RG. Processes for production of high-purity metal powders. JOM. 2003 Mar;55(3):14–8.

23. Liu B, Wildman R, Tuck C, Ashcroft I, Hague R. Investigaztion the effect of particle size distribution on processing parameters optimisation in selective laser melting process. 22nd

Annual International Solid Freeform Fabrication Symposium - An Additive Manufacturing Conference, SFF 2011. 2011 Nov;

24. Singh S, Ramakrishna S, Singh R. Material issues in additive manufacturing: A review. J Manuf Process. 2017 Jan;25:185–200.

25. Silbernagel C, Gargalis L, Ashcroft I, Hague R, Galea M, Dickens P. Electrical resistivity of pure copper processed by medium-powered laser powder bed fusion additive manufacturing for use in electromagnetic applications. Vol. 29, Additive Manufacturing. 2019. p. 100831.

26. King WE, Anderson AT, Ferencz RM, Hodge NE, Kamath C, Khairallah SA, et al. Laser powder bed fusion additive manufacturing of metals; physics, computational, and materials challenges. Appl Phys Rev. 2015 Dec;2(4):041304.

27. Thijs L, Verhaeghe F, Craeghs T, Humbeeck J Van, Kruth JP. A study of the microstructural evolution during selective laser melting of Ti–6Al–4V. Acta Mater. 2010 May;58(9):3303–12.

28. Khorasani AM, Gibson I, Ghasemi A, Ghaderi A. A comprehensive study on variability of relative density in selective laser melting of Ti-6Al-4V. Virtual Phys Prototyp. 2019 Oct 2;14(4):349–59.

29. Dar J, Ponsot AG, Jolma CJ, Lin D. A review on scan strategies in laser-based metal additive manufacturing. Journal of Materials Research and Technology. 2025 May;36:5425–67.

30. Ron T, Shirizly A, Aghion E. Additive Manufacturing Technologies of High Entropy Alloys (HEA): Review and Prospects. Materials. 2023 Mar 19;16(6):2454.

31. Vogiatzief D, Evirgen A, Gein S, Molina VR, Weisheit A, Pedersen M. Laser Powder Bed Fusion and Heat Treatment of an AlCrFe2Ni2 High Entropy Alloy. Front Mater. 2020 Jul 28;7.

32. Kok Y, Tan XP, Wang P, Nai MLS, Loh NH, Liu E, et al. Anisotropy and heterogeneity of microstructure and mechanical properties in metal additive manufacturing: A critical review. Mater Des. 2018;139.

33. Liu C song, Xue X, Wang Y, Zhang H, Li J, Lu Y yuan, et al. Investigation on the characteristics of porosity, melt pool in 316L stainless steel manufactured by laser powder bed fusion. Journal of Materials Research and Technology. 2024 Sep;32:1832–44.

34. Yao S, Wang J, Li M, Chen Z, Lu B, Shen S, et al. LPBF-Formed 2024Al Alloys: Process, Microstructure, Properties, and Thermal Cracking Behavior. Metals (Basel). 2023 Jan 29;13(2):268.

35. Michael F. Ashby, David R.H. Jones. Engineering Materials 1. Elsevier; 2012.

36. Smith WF. Principles of Materials Science and Engineering. In 1986. Available from: https://api.semanticscholar.org/CorpusID:135513349

37. Cantor B. Multicomponent and High Entropy Alloys. Entropy. 2014 Aug 26;16(9):4749–68.

38. Cantor B, Chang ITH, Knight P, Vincent AJB. Microstructural development in equiatomic multicomponent alloys. Materials Science and Engineering: A. 2004 Jul;375–377:213–8.

39. Yeh J -W., Chen S -K., Lin S -J., Gan J -Y., Chin T -S., Shun T -T., et al. Nanostructured High-Entropy Alloys with Multiple Principal Elements: Novel Alloy Design Concepts and Outcomes. Adv Eng Mater. 2004 May 24;6(5):299–303.

40. Miracle DB, Senkov ON. A critical review of high entropy alloys and related concepts. Acta Mater. 2017 Jan;122:448–511.

41. Zhang Y, Zuo TT, Tang Z, Gao MC, Dahmen KA, Liaw PK, et al. Microstructures and properties of high-entropy alloys. Prog Mater Sci. 2014 Apr;61:1–93.

42. Senkov ON, Wilks GB, Scott JM, Miracle DB. Mechanical properties of Nb25Mo25Ta25W25 and V20Nb20Mo20Ta20W20 refractory high entropy alloys. Intermetallics (Barking). 2011 May;19(5):698–706.

43. Ostovari Moghaddam A, Shaburova NA, Samodurova MN, Abdollahzadeh A, Trofimov EA. Additive manufacturing of high entropy alloys: A practical review. J Mater Sci Technol. 2021 Jun;77:131–62.

44. Nartita R, Ionita D, Demetrescu I. A Modern Approach to HEAs: From Structure to Properties and Potential Applications. Crystals (Basel). 2024 May 9;14(5):451.

45. Netzsch-Gerätebau GmbH - STA 449 C Jupiter Thermo-microbalance database [Internet]. [cited 2025 Oct 8]. Available from: https://speciation.net/Database/Instruments/NetzschGeraetebau-GmbH/STA-449-C-Jupiter-Thermomicrobalance-;i2006

46. Aconity3D website [Internet]. [cited 2025 Oct 8]. Available from: https://aconity3d.com/products/aconity-mini/

47. Micromeritics Website [Internet]. [cited 2025 Sep 19]. Available from: https://micromeritics.com/support/accupyc-ii-1345/

48. EMS - Benelux website [Internet]. [cited 2025 Nov 6]. Available from: https://www.ems-benelux.com/produits/infinite-focus-g5

49. Exapro Website [Internet]. [cited 2025 Sep 22]. Available from: https://www.exapro.fr/sp/charmilles-robofil310-53372/

50. STRUERS Website [Internet]. [cited 2025 Sep 22]. Available from: https://www.struers.com/

51. Boston Industries Website [Internet]. [cited 2025 Sep 22]. Available from: https://www.bostonind.com/

52. Kou S. Welding Metallurgy. Wiley; 2002.

53. Blondiau C. Design of High Entropy Alloys through Laser Powder Bed Fusion with the help of Differential Thermal Analysis [Internet]. [Liège, Belgium]: Université de Liège; 2024. Available from: https://matheo.uliege.be/handle/2268.2/20446

54. Epifano E, others. Ellingham diagram: A new look at an old tool. Corros Sci. 2023;

55. Niederwimmer K, others. Annealing Conditions' Influence on the Oxidation of Silicon in Al-Si Alloys. physica status solidi (a). 2019;

56. Kurz W, Fisher DJ. Fundamentals of Solidification. Switzerland: Trans Tech Publication Ltd. 1992 Dec;

57. Ohtsuki T, others. Oxide Behavior During Laser Surface Melting. Metals (Basel). 2025;15(6):627.

58. Deng P. The Origins of Nanoscale Oxide Inclusion and its Evolution in 316L Austenitic Stainless Steel Manufactured by Laser Powder Bed Fusion [Internet]. Auburn University; 2020. Available from: https://auetd.auburn.edu/bitstream/handle/10415/7397/Pu%20Deng%20Dissertation%20.pdf

59. Pistorius PC. Managing Oxide Inclusions in Laser Powder Bed Fusion Builds [Internet]. 2022. Available from: https://engineering.cmu.edu/next/_files/documents/seminars/2022/apr-26-2022-seminar-managing-oxide-inclusions.pdf

60. de Andrade Schwerz C, others. Reduction of oxygen content in laser powder bed fusion process atmosphere: effects on stochastic defect formation and mechanical properties. 2024; Available from: https://research.chalmers.se/publication/541562/file/541562_Fulltext.pdf

61. Stopyra W, others. Laser powder bed fusion of AA7075 alloy: Influence of process parameters on microstructure and hot cracking. Addit Manuf. 2020;

62. Murty BS, Yeh JW, Ranganathan S, Bhattacharjee PP. A brief history of alloys and the birth of high-entropy alloys. In: High-Entropy Alloys. Elsevier; 2019. p. 1–12.

63. Kumar A, Singh A, Suhane A. Mechanically alloyed high entropy alloys: existing challenges and opportunities. Journal of Materials Research and Technology. 2022 Mar;17:2431–56.

64. Krakhmalev P, Yadroitsev I, Yadroitsava I, de Smidt O. Microstructure, Solidification Texture, and Thermal Stability of 316L Stainless Steel Manufactured by Laser Powder Bed Fusion. Metals (Basel). 2018;8(8):643.

65. Raza A. Powder degradation during powder bed fusion processing [Internet]. 2021. Available from: https://research.chalmers.se/publication/526142/file/526142_Fulltext.pdf

66. Sathish K, Kumar SS, Magal RT, Selvaraj V, Narasimharaj V, Karthikeyan R, et al. A Comparative Study on Subtractive Manufacturing and Additive Manufacturing. Parthiban A, editor. Advances in Materials Science and Engineering [Internet]. 2022 Apr 15;2022:1–8. Available from: https://www.hindawi.com/journals/amse/2022/6892641/

67. De Leon E, Riensche A, Bevans BD, Billings C, Siddique Z, Liu Y. A Review of Modeling, Simulation, and Process Qualification of Additively Manufactured Metal Components via the Laser Powder Bed Fusion Method. Journal of Manufacturing and Materials Processing. 2025 Jan 13;9(1):22.

68. Wang J, Zhu R, Liu Y, Zhang L. Understanding melt pool characteristics in laser powder bed fusion: An overview of single- and multi-track melt pools for process optimization. Advanced Powder Materials. 2023 Oct;2(4):100137.

69. Pereira JC, Aranzabe J, Taboada MC, Ruiz N, Rodriguez PP. Analysis of Microstructure and Mechanical Properties in As-Built/As-Cast and Heat-Treated Conditions for IN718 Alloy Obtained by Selective Laser Melting and Investment Casting Processes. Crystals (Basel). 2021 Oct 2;11(10):1196.

70. Pal S, Gubeljak N, Hudák R, Lojen G, Rajťúková V, Brajlih T, et al. Evolution of the metallurgical properties of Ti-6Al-4V, produced with different laser processing parameters, at constant energy density in selective laser melting. Results Phys. 2020 Jun;17:103186.

71. Wang J, Liu S, Fang Y, He Z. A short review on selective laser melting of H13 steel. The International Journal of Advanced Manufacturing Technology. 2020 Jun 9;108(7–8):2453–66.

72. Nene SS. Some Distinct Features of Transformative High Entropy Alloys for Metal Additive Manufacturing. Front Mater. 2022 Jun 2;9.

73. Sonar T, Ivanov M, Trofimov E, Tingaev A, Suleymanova I. A comprehensive review on fusion welding of high entropy alloys – Processing, microstructural evolution and mechanical properties of joints. International Journal of Lightweight Materials and Manufacture. 2024 Jan;7(1):122–83.

74. Tescan Website [Internet]. [cited 2025 Sep 22]. Available from: https://info.tescan.com/

75. Shakor P, Chu SH, Puzatova A, Dini E. Review of binder jetting 3D printing in the construction industry. Progress in Additive Manufacturing. 2022 Aug 21;7(4):643–69.

Appendices

Appendix A – Product sheet of SS 316L powder

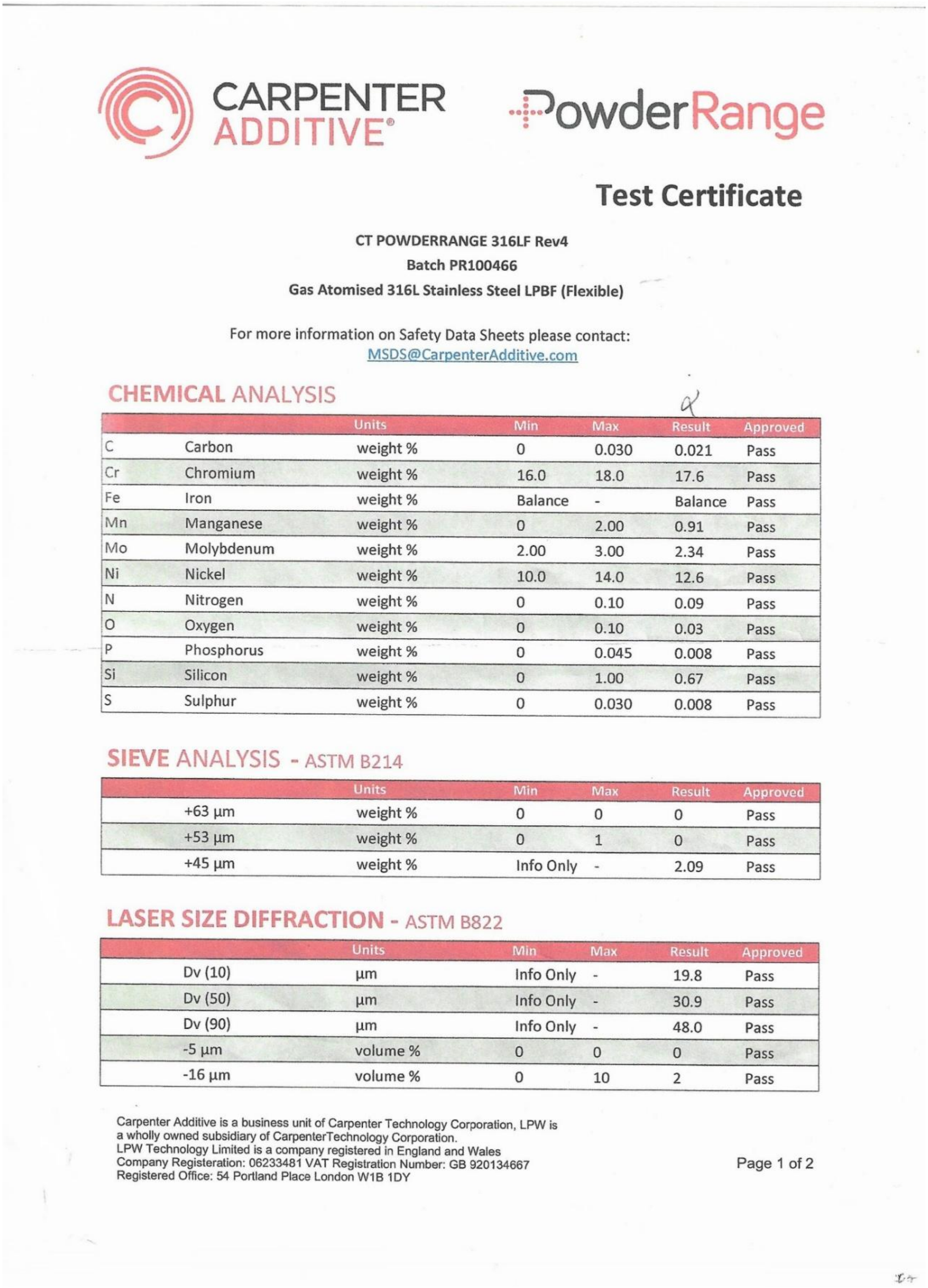

CARPENTER ADDITIVE®

PowderRange

Test Certificate

CT POWDERRANGE 316LF Rev4
Batch PR100466
Gas Atomised 316L Stainless Steel LPBF (Flexible)

For more information on Safety Data Sheets please contact:
MSDS@CarpenterAdditive.com

CHEMICAL ANALYSIS

		Units	Min	Max	Result	Approved
C	Carbon	weight %	0	0.030	0.021	Pass
Cr	Chromium	weight %	16.0	18.0	17.6	Pass
Fe	Iron	weight %	Balance	-	Balance	Pass
Mn	Manganese	weight %	0	2.00	0.91	Pass
Mo	Molybdenum	weight %	2.00	3.00	2.34	Pass
Ni	Nickel	weight %	10.0	14.0	12.6	Pass
N	Nitrogen	weight %	0	0.10	0.09	Pass
O	Oxygen	weight %	0	0.10	0.03	Pass
P	Phosphorus	weight %	0	0.045	0.008	Pass
Si	Silicon	weight %	0	1.00	0.67	Pass
S	Sulphur	weight %	0	0.030	0.008	Pass

SIEVE ANALYSIS - ASTM B214

	Units	Min	Max	Result	Approved
+63 µm	weight %	0	0	0	Pass
+53 µm	weight %	0	1	0	Pass
+45 µm	weight %	Info Only	-	2.09	Pass

LASER SIZE DIFFRACTION - ASTM B822

	Units	Min	Max	Result	Approved
Dv (10)	µm	Info Only	-	19.8	Pass
Dv (50)	µm	Info Only	-	30.9	Pass
Dv (90)	µm	Info Only	-	48.0	Pass
-5 µm	volume %	0	0	0	Pass
-16 µm	volume %	0	10	2	Pass

Carpenter Additive is a business unit of Carpenter Technology Corporation, LPW is
a wholly owned subsidiary of CarpenterTechnology Corporation.
LPW Technology Limited is a company registered in England and Wales
Company Registeration: 06233481 VAT Registration Number: GB 920134667
Registered Office: 54 Portland Place London W1B 1DY

Page 1 of 2

Appendix B – Product sheet of Ni-Cr, Mn, and Al powders

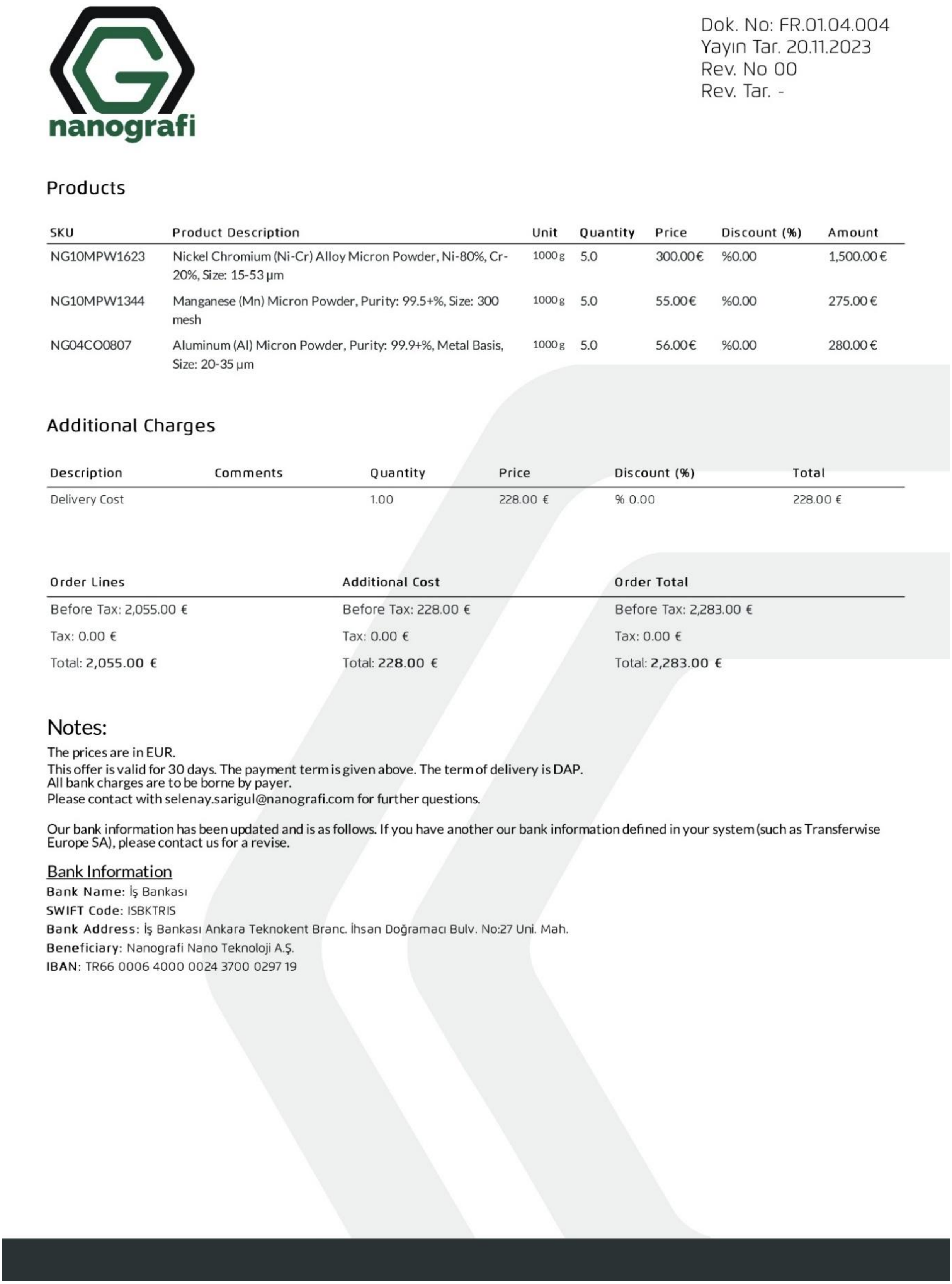

nanografi

Dok. No: FR.01.04.004
Yayın Tar. 20.11.2023
Rev. No 00
Rev. Tar. -

Products

SKU	Product Description	Unit	Quantity	Price	Discount (%)	Amount
NG10MPW1623	Nickel Chromium (Ni-Cr) Alloy Micron Powder, Ni-80%, Cr-20%, Size: 15-53 µm	1000 g	5.0	300.00 €	%0.00	1,500.00 €
NG10MPW1344	Manganese (Mn) Micron Powder, Purity: 99.5+%, Size: 300 mesh	1000 g	5.0	55.00 €	%0.00	275.00 €
NG04CO0807	Aluminum (Al) Micron Powder, Purity: 99.9+%, Metal Basis, Size: 20-35 µm	1000 g	5.0	56.00 €	%0.00	280.00 €

Additional Charges

Description	Comments	Quantity	Price	Discount (%)	Total
Delivery Cost		1.00	228.00 €	% 0.00	228.00 €

Order Lines	Additional Cost	Order Total
Before Tax: 2,055.00 €	Before Tax: 228.00 €	Before Tax: 2,283.00 €
Tax: 0.00 €	Tax: 0.00 €	Tax: 0.00 €
Total: **2,055.00 €**	Total: **228.00 €**	Total: **2,283.00 €**

Notes:

The prices are in EUR.
This offer is valid for 30 days. The payment term is given above. The term of delivery is DAP.
All bank charges are to be borne by payer.
Please contact with selenay.sarigul@nanografi.com for further questions.

Our bank information has been updated and is as follows. If you have another our bank information defined in your system (such as Transferwise Europe SA), please contact us for a revise.

Bank Information

Bank Name: İş Bankası
SWIFT Code: ISBKTRIS
Bank Address: İş Bankası Ankara Teknokent Branc. İhsan Doğramacı Bulv. No:27 Uni. Mah.
Beneficiary: Nanografi Nano Teknoloji A.Ş.
IBAN: TR66 0006 4000 0024 3700 0297 19

Appendix C – Table of single-track parameter sets

Laser Power P (W)	Laser Scan Speed V_s (mm/s)	Linear Energy Density E_l (J/mm)
100	200	0.500
100	400	0.250
100	600	0.167
100	800	0.125
100	1000	0.100
125	400	0.313
125	600	0.208
125	800	0.156
125	1000	0.125
125	1200	0.104
125	1400	0.089
125	1600	0.078
125	2000	0.063
150	200	0.750
150	400	0.375
150	600	0.250
150	800	0.188
150	1000	0.150
150	1200	0.125
150	1400	0.107
150	1600	0.094
150	1800	0.083
150	2000	0.075
175	200	0.875
175	400	0.438
175	600	0.292
175	800	0.219
175	1000	0.175
175	1200	0.146
175	1400	0.125
175	1600	0.109
175	1800	0.097
175	2000	0.088
185	200	0.925
185	400	0.463
185	600	0.308
185	800	0.231
185	1000	0.185
185	1200	0.154

185	1400	0.132
185	1600	0.116
185	1800	0.103
185	2000	0.093
200	200	1.000
200	400	0.500
200	600	0.333
200	800	0.250
200	1000	0.200
200	1200	0.167
200	1400	0.143
200	1600	0.125
200	1800	0.111
200	2000	0.100

Appendix D – Use of Artificial Intelligence Tools

Artificial Intelligence tools were used during the preparation of this work. In particular, ChatGPT (OpenAI) was used to assist with Python code optimization and to support language verification and text reformulation of the manuscript.

No AI tools were used for the generation of scientific content, data fabrication, or interpretation of results.